Mathematical Problems in Engineering

Mathematical and Numerical Methods for Microelectromechanical and Nanoelectromechanical Systems Devices

Lead Guest Editor: Agustin Herrera-May
Guest Editors: Muhammad W. Ashraf, Francisco López-Huerta, and Shahzadi Tayyaba

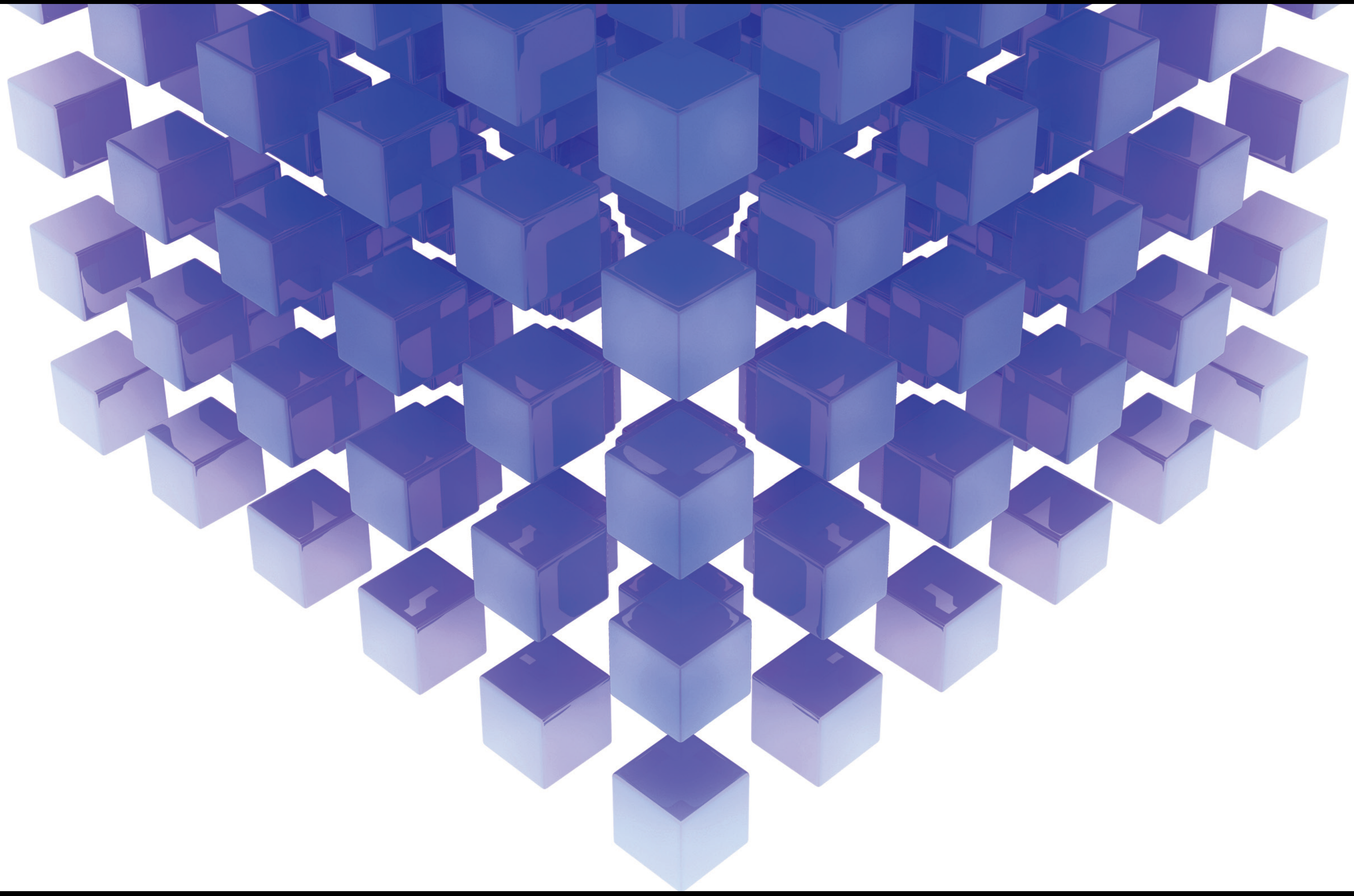

Mathematical and Numerical Methods for Microelectromechanical and Nanoelectromechanical Systems Devices

Mathematical Problems in Engineering

Mathematical and Numerical Methods for Microelectromechanical and Nanoelectromechanical Systems Devices

Lead Guest Editor: Agustin Herrera-May
Guest Editors: Muhammad W. Ashraf, Francisco López-Huerta, and Shahzadi Tayyaba

Paolo Boscariol, Italy
Daniela Boso, Italy
Guillermo Botella-Juan, Spain
Abdesselem Boulkroune, Algeria
Boulaïd Boulkroune, Belgium
Fabio Bovenga, Italy
Francesco Braghin, Italy
Ricardo Branco, Portugal
Julien Bruchon, France
Matteo Bruggi, Italy
Michele Brun, Italy
Maria Elena Bruni, Italy
Maria Angela Butturi, Italy
Bartłomiej Błachowski, Poland
Dhanamjayulu C, India
Raquel Caballero-Águila, Spain
Filippo Cacace, Italy
Salvatore Caddemi, Italy
Zuowei Cai, China
Roberto Caldelli, Italy
Francesco Cannizzaro, Italy
Maosen Cao, China
Ana Carpio, Spain
Rodrigo Carvajal, Chile
Caterina Casavola, Italy
Sara Casciati, Italy
Federica Caselli, Italy
Carmen Castillo, Spain
Inmaculada T. Castro, Spain
Miguel Castro, Portugal
Giuseppe Catalanotti, United Kingdom
Alberto Cavallo, Italy
Gabriele Cazzulani, Italy
Fatih Vehbi Celebi, Turkey
Miguel Cerrolaza, Venezuela
Gregory Chagnon, France
Ching-Ter Chang, Taiwan
Kuei-Lun Chang, Taiwan
Qing Chang, USA
Xiaoheng Chang, China
Prasenjit Chatterjee, Lithuania
Kacem Chehdi, France
Peter N. Cheimets, USA
Chih-Chiang Chen, Taiwan
He Chen, China
Kebing Chen, China
Mengxin Chen, China
Shyi-Ming Chen, Taiwan
Xizhong Chen, Ireland
Xue-Bo Chen, China
Zhiwen Chen, China
Qiang Cheng, USA
Zeyang Cheng, China
Luca Chiapponi, Italy
Francisco Chicano, Spain
Tirivanhu Chinyoka, South Africa
Adrian Chmielewski, Poland
Seongim Choi, USA
Gautam Choubey, India
Hung-Yuan Chung, Taiwan
Yusheng Ci, China
Simone Cinquemani, Italy
Roberto G. Citarella, Italy
Joaquim Ciurana, Spain
John D. Clayton, USA
Piero Colajanni, Italy
Giuseppina Colicchio, Italy
Vassilios Constantoudis, Greece
Enrico Conte, Italy
Alessandro Contento, USA
Mario Cools, Belgium
Gino Cortellessa, Italy
Carlo Cosentino, Italy
Paolo Crippa, Italy
Erik Cuevas, Mexico
Guozeng Cui, China
Mehmet Cunkas, Turkey
Giuseppe D'Aniello, Italy
Peter Dabnichki, Australia
Weizhong Dai, USA
Zhifeng Dai, China
Purushothaman Damodaran, USA
Sergey Dashkovskiy, Germany
Adiel T. De Almeida-Filho, Brazil
Fabio De Angelis, Italy
Samuele De Bartolo, Italy
Stefano De Miranda, Italy
Filippo De Monte, Italy

José António Fonseca De Oliveira Correia, Portugal
Jose Renato De Sousa, Brazil
Michael Defoort, France
Alessandro Della Corte, Italy
Laurent Dewasme, Belgium
Sanku Dey, India
Gianpaolo Di Bona, Italy
Roberta Di Pace, Italy
Francesca Di Puccio, Italy
Ramón I. Diego, Spain
Yannis Dimakopoulos, Greece
Hasan Dinçer, Turkey
José M. Domínguez, Spain
Georgios Dounias, Greece
Bo Du, China
Emil Dumic, Croatia
Madalina Dumitriu, United Kingdom
Premraj Durairaj, India
Saeed Eftekhar Azam, USA
Said El Kafhali, Morocco
Antonio Elipe, Spain
R. Emre Erkmen, Canada
John Escobar, Colombia
Leandro F. F. Miguel, Brazil
FRANCESCO FOTI, Italy
Andrea L. Facci, Italy
Shahla Faisal, Pakistan
Giovanni Falsone, Italy
Hua Fan, China
Jianguang Fang, Australia
Nicholas Fantuzzi, Italy
Muhammad Shahid Farid, Pakistan
Hamed Faroqi, Iran
Yann Favennec, France
Fiorenzo A. Fazzolari, United Kingdom
Giuseppe Fedele, Italy
Roberto Fedele, Italy
Baowei Feng, China
Mohammad Ferdows, Bangladesh
Arturo J. Fernández, Spain
Jesus M. Fernandez Oro, Spain
Francesco Ferrise, Italy
Eric Feulvarch, France
Thierry Floquet, France
Eric Florentin, France
Gerardo Flores, Mexico
Antonio Forcina, Italy
Alessandro Formisano, Italy
Francesco Franco, Italy
Elisa Francomano, Italy
Juan Frausto-Solis, Mexico
Shujun Fu, China
Juan C. G. Prada, Spain
HECTOR GOMEZ, Chile
Matteo Gaeta, Italy
Mauro Gaggero, Italy
Zoran Gajic, USA
Jaime Gallardo-Alvarado, Mexico
Mosè Gallo, Italy
Akemi Gálvez, Spain
Maria L. Gandarias, Spain
Hao Gao, Hong Kong
Xingbao Gao, China
Yan Gao, China
Zhiwei Gao, United Kingdom
Giovanni Garcea, Italy
José García, Chile
Harish Garg, India
Alessandro Gasparetto, Italy
Stylianos Georgantzinos, Greece
Fotios Georgiades, India
Parviz Ghadimi, Iran
Ştefan Cristian Gherghina, Romania
Georgios I. Giannopoulos, Greece
Agathoklis Giaralis, United Kingdom
Anna M. Gil-Lafuente, Spain
Ivan Giorgio, Italy
Gaetano Giunta, Luxembourg
Jefferson L.M.A. Gomes, United Kingdom
Emilio Gómez-Déniz, Spain
Antonio M. Gonçalves de Lima, Brazil
Qunxi Gong, China
Chris Goodrich, USA
Rama S. R. Gorla, USA
Veena Goswami, India
Xunjie Gou, Spain
Jakub Grabski, Poland

Irfan Kaymaz, Turkey
Vahid Kayvanfar, Qatar
Krzysztof Kecik, Poland
Mohamed Khader, Egypt
Chaudry M. Khalique, South Africa
Mukhtaj Khan, Pakistan
Shahid Khan, Pakistan
Nam-Il Kim, Republic of Korea
Philipp V. Kiryukhantsev-Korneev, Russia
P.V.V Kishore, India
Jan Koci, Czech Republic
Ioannis Kostavelis, Greece
Sotiris B. Kotsiantis, Greece
Frederic Kratz, France
Vamsi Krishna, India
Edyta Kucharska, Poland
Krzysztof S. Kulpa, Poland
Kamal Kumar, India
Prof. Ashwani Kumar, India
Michal Kunicki, Poland
Cedrick A. K. Kwuimy, USA
Kyandoghere Kyamakya, Austria
Ivan Kyrchei, Ukraine
Márcio J. Lacerda, Brazil
Eduardo Lalla, The Netherlands
Giovanni Lancioni, Italy
Jaroslaw Latalski, Poland
Hervé Laurent, France
Agostino Lauria, Italy
Aimé Lay-Ekuakille, Italy
Nicolas J. Leconte, France
Kun-Chou Lee, Taiwan
Dimitri Lefebvre, France
Eric Lefevre, France
Marek Lefik, Poland
Yaguo Lei, China
Kauko Leiviskä, Finland
Ervin Lenzi, Brazil
ChenFeng Li, China
Jian Li, USA
Jun Li, China
Yueyang Li, China
Zhao Li, China
Zhen Li, China
En-Qiang Lin, USA
Jian Lin, China
Qibin Lin, China
Yao-Jin Lin, China
Zhiyun Lin, China
Bin Liu, China
Bo Liu, China
Heng Liu, China
Jianxu Liu, Thailand
Lei Liu, China
Sixin Liu, China
Wanquan Liu, China
Yu Liu, China
Yuanchang Liu, United Kingdom
Bonifacio Llamazares, Spain
Alessandro Lo Schiavo, Italy
Jean Jacques Loiseau, France
Francesco Lolli, Italy
Paolo Lonetti, Italy
António M. Lopes, Portugal
Sebastian López, Spain
Luis M. López-Ochoa, Spain
Vassilios C. Loukopoulos, Greece
Gabriele Maria Lozito, Italy
Zhiguo Luo, China
Gabriel Luque, Spain
Valentin Lychagin, Norway
YUE MEI, China
Junwei Ma, China
Xuanlong Ma, China
Antonio Madeo, Italy
Alessandro Magnani, Belgium
Toqeer Mahmood, Pakistan
Fazal M. Mahomed, South Africa
Arunava Majumder, India
Sarfraz Nawaz Malik, Pakistan
Paolo Manfredi, Italy
Adnan Maqsood, Pakistan
Muazzam Maqsood, Pakistan
Giuseppe Carlo Marano, Italy
Damijan Markovic, France
Filipe J. Marques, Portugal
Luca Martinelli, Italy
Denizar Cruz Martins, Brazil

George A. Papakostas, Greece
Xosé M. Pardo, Spain
You-Jin Park, Taiwan
Manuel Pastor, Spain
Pubudu N. Pathirana, Australia
Surajit Kumar Paul, India
Luis Payá, Spain
Igor Pažanin, Croatia
Libor Pekař, Czech Republic
Francesco Pellicano, Italy
Marcello Pellicciari, Italy
Jian Peng, China
Mingshu Peng, China
Xiang Peng, China
Xindong Peng, China
Yuexing Peng, China
Marzio Pennisi, Italy
Maria Patrizia Pera, Italy
Matjaz Perc, Slovenia
A. M. Bastos Pereira, Portugal
Wesley Peres, Brazil
F. Javier Pérez-Pinal, Mexico
Michele Perrella, Italy
Francesco Pesavento, Italy
Francesco Petrini, Italy
Hoang Vu Phan, Republic of Korea
Lukasz Pieczonka, Poland
Dario Piga, Switzerland
Marco Pizzarelli, Italy
Javier Plaza, Spain
Goutam Pohit, India
Dragan Poljak, Croatia
Jorge Pomares, Spain
Hiram Ponce, Mexico
Sébastien Poncet, Canada
Volodymyr Ponomaryov, Mexico
Jean-Christophe Ponsart, France
Mauro Pontani, Italy
Sivakumar Poruran, India
Francesc Pozo, Spain
Aditya Rio Prabowo, Indonesia
Anchasa Pramuanjaroenkij, Thailand
Leonardo Primavera, Italy
B Rajanarayan Prusty, India
Krzysztof Puszynski, Poland
Chuan Qin, China
Dongdong Qin, China
Jianlong Qiu, China
Giuseppe Quaranta, Italy
DR. RITU RAJ, India
Vitomir Racic, Italy
Carlo Rainieri, Italy
Kumbakonam Ramamani Rajagopal, USA
Ali Ramazani, USA
Angel Manuel Ramos, Spain
Higinio Ramos, Spain
Muhammad Afzal Rana, Pakistan
Muhammad Rashid, Saudi Arabia
Manoj Rastogi, India
Alessandro Rasulo, Italy
S.S. Ravindran, USA
Abdolrahman Razani, Iran
Alessandro Reali, Italy
Jose A. Reinoso, Spain
Oscar Reinoso, Spain
Haijun Ren, China
Carlo Renno, Italy
Fabrizio Renno, Italy
Shahram Rezapour, Iran
Ricardo Riaza, Spain
Francesco Riganti-Fulginei, Italy
Gerasimos Rigatos, Greece
Francesco Ripamonti, Italy
Jorge Rivera, Mexico
Eugenio Roanes-Lozano, Spain
Ana Maria A. C. Rocha, Portugal
Luigi Rodino, Italy
Francisco Rodríguez, Spain
Rosana Rodríguez López, Spain
Francisco Rossomando, Argentina
Jose de Jesus Rubio, Mexico
Weiguo Rui, China
Rubén Ruiz, Spain
Ivan D. Rukhlenko, Australia
Dr. Eswaramoorthi S., India
Weichao SHI, United Kingdom
Chaman Lal Sabharwal, USA
Andrés Sáez, Spain

Yong (Aaron) Tan, United Kingdom
Marco Antonio Taneco-Hernández, Mexico
Lu Tang, China
Tianyou Tao, China
Hafez Tari, USA
Alessandro Tasora, Italy
Sergio Teggi, Italy
Adriana del Carmen Téllez-Anguiano, Mexico
Ana C. Teodoro, Portugal
Efstathios E. Theotokoglou, Greece
Jing-Feng Tian, China
Alexander Timokha, Norway
Stefania Tomasiello, Italy
Gisella Tomasini, Italy
Isabella Torcicollo, Italy
Francesco Tornabene, Italy
Mariano Torrisi, Italy
Thang nguyen Trung, Vietnam
George Tsiatas, Greece
Le Anh Tuan, Vietnam
Nerio Tullini, Italy
Emilio Turco, Italy
Ilhan Tuzcu, USA
Efstratios Tzirtzilakis, Greece
FRANCISCO UREÑA, Spain
Filippo Ubertini, Italy
Mohammad Uddin, Australia
Mohammad Safi Ullah, Bangladesh
Serdar Ulubeyli, Turkey
Mati Ur Rahman, Pakistan
Panayiotis Vafeas, Greece
Giuseppe Vairo, Italy
Jesus Valdez-Resendiz, Mexico
Eusebio Valero, Spain
Stefano Valvano, Italy
Carlos-Renato Vázquez, Mexico
Martin Velasco Villa, Mexico
Franck J. Vernerey, USA
Georgios Veronis, USA
Vincenzo Vespri, Italy
Renato Vidoni, Italy
Venkatesh Vijayaraghavan, Australia
Anna Vila, Spain
Francisco R. Villatoro, Spain
Francesca Vipiana, Italy
Stanislav Vítek, Czech Republic
Jan Vorel, Czech Republic
Michael Vynnycky, Sweden
Mohammad W. Alomari, Jordan
Roman Wan-Wendner, Austria
Bingchang Wang, China
C. H. Wang, Taiwan
Dagang Wang, China
Guoqiang Wang, China
Huaiyu Wang, China
Hui Wang, China
J.G. Wang, China
Ji Wang, China
Kang-Jia Wang, China
Lei Wang, China
Qiang Wang, China
Qingling Wang, China
Weiwei Wang, China
Xinyu Wang, China
Yong Wang, China
Yung-Chung Wang, Taiwan
Zhenbo Wang, USA
Zhibo Wang, China
Waldemar T. Wójcik, Poland
Chi Wu, Australia
Qiuhong Wu, China
Yuqiang Wu, China
Zhibin Wu, China
Zhizheng Wu, China
Michalis Xenos, Greece
Hao Xiao, China
Xiao Ping Xie, China
Qingzheng Xu, China
Binghan Xue, China
Yi Xue, China
Joseph J. Yame, France
Chuanliang Yan, China
Xinggang Yan, United Kingdom
Hongtai Yang, China
Jixiang Yang, China
Mijia Yang, USA
Ray-Yeng Yang, Taiwan

Contents

Hindawi
Mathematical Problems in Engineering
Volume 2022, Article ID 7326504, 11 pages
https://doi.org/10.1155/2022/7326504

Research Article

Effects of the Magnetohydrodynamic Flow within the Boundary Layer of a Jeffery Fluid in a Porous Medium over a Shrinking/Stretching Sheet

Shaila S. Benal,[1] Jagadish V. Tawade,[2,3] Mahadev M. Biradar,[4] and Haiter Lenin Allasi[5]

[1]*Department of Mathematics, B.L.D.E. A's V. P. Dr. P. G. Halakatti College of Engineering and Technology, Vijayapur-586103, Karnataka, India*
[2]*Department of Mathematics, Vishwakarma University, Pune-411048, Maharashtra, India*
[3]*Department of Mathematics, Bheemanna Khandre Institute of Technology, Bhalki-585328, Karnataka, India*
[4]*Department of Mathematics, Basaveshwar Engineering College (Autonomous), Bagalkot-587103, Karnataka, India*
[5]*Department of Mechanical Engineering, WOLLO University, Kombolcha Institute of Technology, P O. Box 208, Kombolcha, Ethiopia*

Correspondence should be addressed to Haiter Lenin Allasi; drahlenin@kiot.edu.et

Received 5 May 2022; Accepted 14 June 2022; Published 1 July 2022

Academic Editor: Muhammad Waseem Ashraf

The consequences of magnetohydrodynamic flow inside the boundary layer of a Jeffery fluid in a porous material across a shrinking/stretching sheet are discussed in this paper. The Runge–Kutta fourth-order technique is used to turn partial differential equations into nonlinear ordinary differential equations and solve them using similarity transformation. On the velocity and temperature profiles, the effects of key factors such as "thermal stratification" e_1, λ_1 "Jeffery parameter," Pr "Prandtl number", M "Magnetic field," "Porous parameter" λ_2, and "heat generation/absorption" have been visually described. In terms of heat transmission, the Jeffrey nanofluid beats other fluids such as Oldroyd-B and Maxwell nanofluids, according to the findings. According to our findings, the thickness of the boundary layer is explored in both stretching and shrinking. When the "thermal stratification" e_1 parameter is increased, fluid velocity and temperature rise, while the "heat generation/absorption" γ parameter has the opposite effect.

1. Introduction

Non-Newtonian fluids such as printing inks, polymer solutions, ketchup, glues, detergent slurries, and pastes are basically nonlinear and regularly show elastic as well as viscous properties. Such constitutive equations are more advanced than standard (Navier Stokes) Newtonian fluid. Preeminent non-Newtonian type Walters-B short memory models, Jeffery models, and Oldroyd-B models have different degrees of clarification of the classical momentum preserve these equations. Jeffrey most is the most straightforward non-Newtonian liquid which displays shear diminishing properties, excessive shear viscosity, and yield pressure. Many engineering researchers are fascinated because of its variety of applications and simplicity in engineering and science. Crane (1) studied flow overstretching plate and gave a precise resembling solution and solved analytically for peripheral layer flow of incompressible viscous fluid.

"Wang [1] conferred the concept of the flow around the shrinking sheet in his study of unsteady film. The existence and uniqueness of the solution of steady viscous flow over a shrinking sheet were proved by Milkovich and Wang [2]. Miklavcic and W [3] first studied the MHD flow over a stretching surface in an electrically conducting fluid. The authors of [4, 5] studied stretching sheets. Makinde [6] explored heat and mass transfer with mixed convection in presence of a stagnation point. Shateyi and Makinde [7] discussed on convectively heated disk with hydromagnetic stagnation point flow towards a radically stretching. Ellahi et al. [8] discussed the peristaltic flow pf Jeffery in a rectangular duct. [9] Yakubu Seini and Oluwole Makinde traced on boundary layer flow near stagnation points on a vertical surface in the presence of the transverse magnetic field. The third-grade nanofluid flow generated by sheet stretching was influenced by Khan et al. [10]. With viscous dissipation and Joule heating, the MHD stagnation point flow of Jeffery fluid radically was studied by Hayat et al. [11]. El-Aziz [12] studied the dual solutions in hydromagnetic stagnation point flow and heat transfer towards a stretching/shrinking sheet with a nonuniform heat source/sink and variable surface heat flux. Turkyilmazoglu [13] analysed the flow of a micropolar fluid due to a porous stretching sheet and heat transfer." Babu and Narayana [14] studied on mixed convection of a Jeffrey fluid over a stretching sheet with power-law heat flux. Shahzad et al. [15] reported on unsteady axisymmetric flow and heat transfer over a time-dependent radically stretching sheet. Eswara Rao and Sreenadh [16] discussed on boundary layer flow of Jeffery fluid over a shrinking/stretching sheet. Mishra et al. [17] proposed a non-Newtonian convective flow in two dimensions in the presence of a heat source and sink. Eswara and Krishna Murthy [18] proposed the flow of Jeffrey fluid through a stretching/shrinking sheet over porous material was studied using MHD stagnation point flow. The authors of [19, 20] studied on stagnation point. The heat transport properties of an incompressible non-Newtonian Jeffery liquid over a stretching/shrinking surface with polluted radiation and a heat source were investigated by Babu et al. [21]. A number of authors have freshly investigated non-Newtonian fluid flow models incorporating a variety of heat transfer effects.

The effect of MHD flow on various fluid models was later addressed by multiple writers [22–26] with the convective boundary flows through the periphery layer. Peripheral layer flow with convective boundary conditions is used in manufacturing and ecological technologies, as well as energy storage, gas turbines, geothermal reservoirs, and nuclear reactors. Transmission has gained a lot of traction. The relevant studies comprise Afzal et al. [27], Afzal et al. [28], and Tayyaba et al. [29].

Motivated by previous literature, we study the effects of thermal stratification, Jeffery parameter, Prandtl number, magnetic field, porous parameter, and heat generation/absorption for Jeffery fluid by taking into account the later wall being impermeable. The major observation is the rise in the porosity parameter of the fluid is caused by an increase in the viscosity of the fluid, whereas a drop in the porosity at the wall results in a progressive reduction in the fluid's flow velocity, as observed. The results are obtained with the help of bvp4c and are presented in form of tables and figures.

2. Formulation Problem

A two-dimensional (x, y) MHD stream of incompressible Jeffrey liquid flows across a $y = 0$ shrinking/stretching sheet. In standard notation, the MHD Jeffery fluid flow and temperature equations are expressed as (ref [28] and [29])

$$\frac{\partial u}{\partial x} + \frac{\partial u}{\partial y}, \tag{1}$$

$$u\frac{\partial u}{\partial x} + v\frac{\partial u}{\partial y} = \left(\frac{\nu}{1+\lambda_1}\right)\frac{\partial^2 u}{\partial y^2} - \frac{\sigma B_0^2}{\rho}u - \frac{\nu}{k}u, \tag{2}$$

$$u\frac{\partial T}{\partial x} + v\frac{\partial T}{\partial y} = \frac{k}{\rho C_p}\frac{\partial^2 T}{\partial y^2} + \frac{Q}{\rho C_p}(T - T_\infty). \tag{3}$$

Velocity components u & v, "$\nu = \mu/\rho$" denotes kinematic fluid viscosity, "ρ" denotes fluid density, μ is the coefficient of fluid viscosity, λ_1 represents Jeffery parameter, Cp and k represent specific heat and thermal conductivity at constant pressure, and Q denotes heat generation/absorption. The boundary conditions for the present study are

$$\left.\begin{array}{l} u = U_w, v = -v_w, T = T_w = T_0 + b_1 x at y = 0 \\ u \longrightarrow 0 \Rightarrow T \longrightarrow T_\infty = T_0 + b_2 x, y \longrightarrow \infty, as y \longrightarrow \infty \end{array}\right\}, \tag{4}$$

where $U_w = cx$ represents for stretching sheet case, and $U_w = -cx$ represents for the situation of shrinking sheet case with $e > 0$ being shrinking/stretching constant. v_w wall mass transfer velocity with $v_w > 0$ for mass suction and $v_w < 0$ for mass injection.

Similarity transformations are

$$\left.\begin{array}{l} \psi = \sqrt{c\nu}\, x f(\eta) \text{ and } \eta = y\sqrt{\dfrac{c}{\nu}} \\ \theta(\eta) = \dfrac{T - T_\infty}{T_w - T_0} \Rightarrow T = (T_w - T_o)\theta(\eta) + T_\infty \end{array}\right\}, \tag{5}$$

where ψ is stream function, and η is similarity variable. Stream functions are defined as

$$u = \frac{\partial \psi}{\partial y} \text{and} v = -\frac{\partial \psi}{\partial x}. \tag{6}$$

Also,

$$T = b_1 x\theta(\eta) \& T_\infty = T_0 + b_2. \tag{7}$$

Using equation (5), the equations (2) and (3) take the forms

$$\left(\frac{1}{1+\lambda_1}\right)f''' + ff'' - f'^2 - (M + \lambda_2)f' = 0, \tag{8}$$

$$\theta'' + Pr\theta' f - Pr\theta f' - Pre_1 f' + Pr\gamma\theta = 0. \tag{9}$$

The corresponding boundary condition for the stretching sheet is as follows:

$$\begin{array}{c} f(\eta) = S, f'(\eta) = 1, \theta(0) = 1 - e_1 at \eta = 0; \\ f'(\eta) \longrightarrow 0, \theta(\infty) \longrightarrow 0, as \eta \longrightarrow \infty. \end{array} \tag{10}$$

For shrinking sheet,

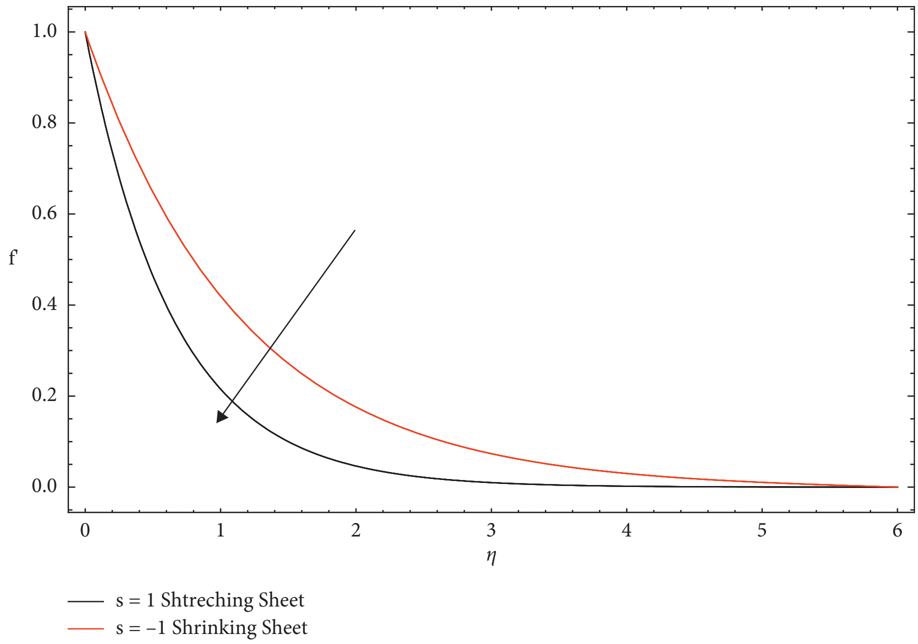

FIGURE 1: The impact of Prandtl number Pr on the velocity profile.

$$f(\eta) = S, f'(\eta) = -1, \theta(0) = 1 - e_1 at\eta = 0;$$
$$f'(\infty) \longrightarrow 0, \theta(\infty) \longrightarrow 0, as\eta \longrightarrow \infty, \quad (11)$$

$S = v_w/(cv)^{1/2}$. With $S > 0$ (i.e., $v_w > 0$) $S < 0$ (i.e., $v_w < 0$) for wall mass suction and wall mass injection, S represents wall mass parameter.

where $M = \sigma B_0^2/\rho c$ magnetic parameter, $\lambda_2 = v/ck$ porous parameter, $pr = \mu C_p/K$. Thermal stratification parameter $e_1 = b_2/b_1$ and $\gamma = Q/\rho C_p a$ heat generation/absorption parameter.

3. Methodology

To solve the BVPs, the governing equation is solved using the firing system with the Runge–Kutta fourth-order technique. Equations (8) and (11) are used to translate the altered ODEs into the following system.

$$\frac{df_0}{d\eta} = f_{1,} \frac{df_1}{d\eta} = f_{2,} (1+\lambda) \frac{df_2}{d\eta} = \left(f_1^2 + M + \lambda_2\right) f_1 - f_0 f_2 \Big), \quad (12)$$

$$\frac{d\theta_0}{d\eta} = \theta_1, \frac{d\theta_1}{d\eta} = \Pr\left[f_1\theta_0 + e_1 f_1 + \gamma\theta_0 - \theta_1 f_o\right]. \quad (13)$$

Following that, the boundary conditions, equations ten and eleven, take the form of stretching and shrinking. $f_o = S$, $f_1(0) = -1, f_1(\infty) = 0, \theta_0(0) = 1 - e_1, \theta_0(\infty) = 0$ $f_o = f(\eta)$, and$\theta_0 = \theta(\eta)$ By correctly estimating the omitted slopes, the aforementioned BVP is first turned into an IVP. The MATLAB bvp4c package is used to solve the generated IVPs.

4. Results & Discussion

Figure 1 shows the impact of Prandtl no "Pr" on f' (velocity profile) & "θ" temperature profile for both cases stretching and shrinking. An increase in Prandtl no composes the fluid more dense, which causes a decline in the velocity profile. In temperature profile for both the cases, for different values of Pr no decreases, because the dimensionless number is inversely related to thermal conductivity, it follows that increases in Prandtl no hold weak energy diffusion. Upgrading Pr causes a significant drop in fluid temperature, resulting in a smaller thermal boundary layer. While shrinking a sheet, an immense Prandtl number fluid induces thermal unsteadiness at the superficial (i.e., a negative value of Nu), but this is not the case when stretching a sheet. This is shown in Figure 2. Thermal stratification e_1 is plotted in Figures 3 and 4 for stretching and shrinking on the velocity profile and temperature profile. Thermal stratification e_1 because the convective potential among the sheet surface and the ambient temperature is reduced, the fluid's velocity is reduced. "θ" temperature decreases enhances in the stratification parameter. An effect of heat generation/absorption γ in Figures 5 and 6 demonstrates how the temperature changes as the heat emission/immersion parameter is changed. It has been discovered that as γ grows, so does the temperature. The existence of a transverse magnetic field induces the Lorentz force, which results in a velocity field retarding force. The retarding force increases as the value of M increases, and as a result, the velocity decreases as the temperature and concentration profiles increase. The thickness of the thermal boundary layer thickens as the fluid temperature rises. The presence of an external heat source has a considerable effect on the fluid's temperature gradient, resulting in an increase in both the temperature distribution

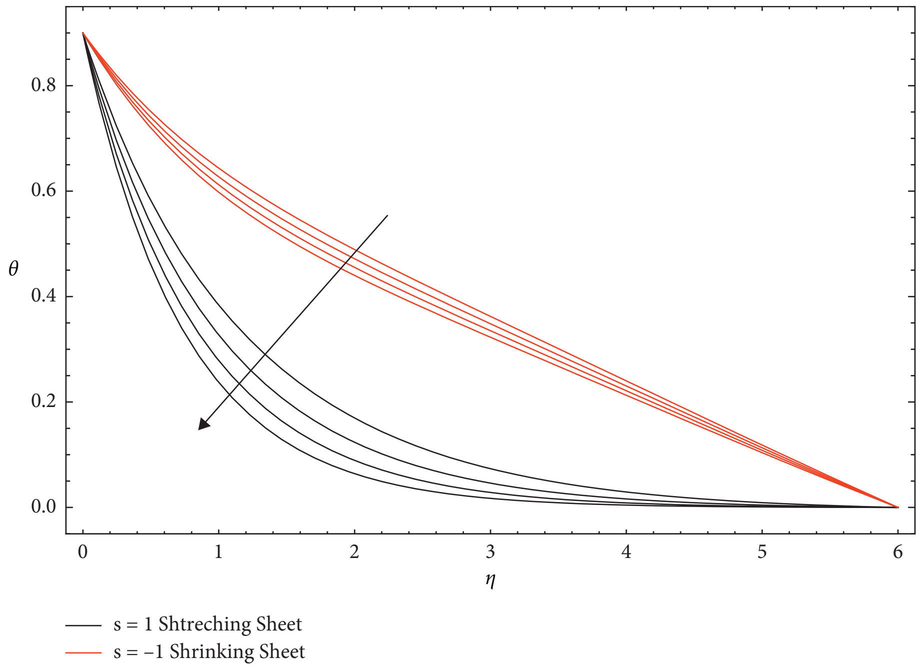

Figure 2: "Pr" on the temperature profile.

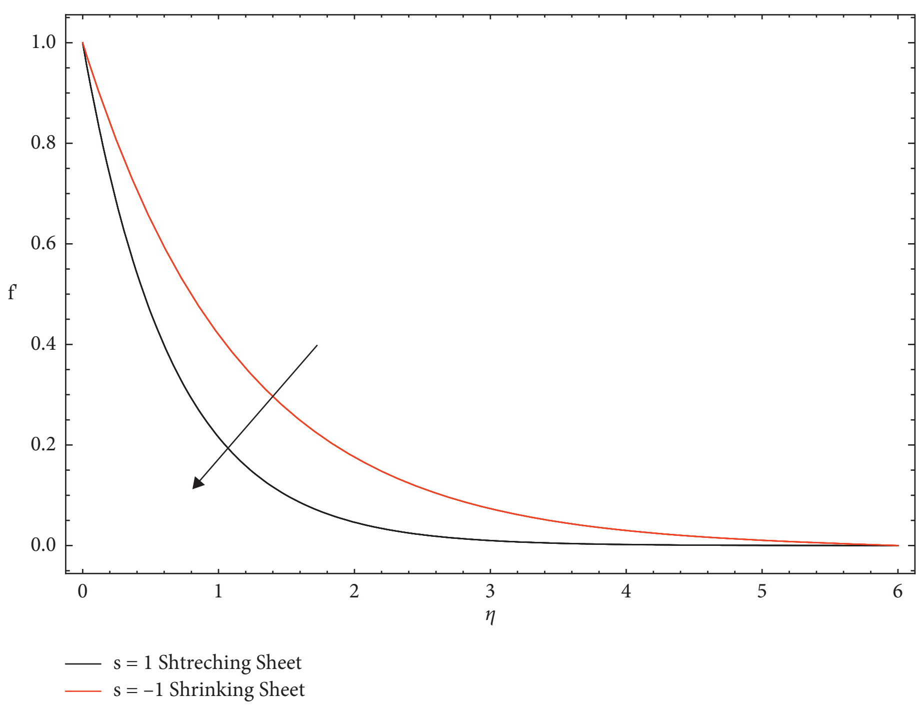

Figure 3: Thermal stratification e_1 for velocity profile.

and the fluid's thermal state. The thermal boundary layer thickness grows to a greater extent as a considerable amount of heat energy is created among fluid particles. When the parameter M shrinks, different values of M cause the velocity to rise, as shown in Figure 7. The influence of the magnetic field parameter M on flow temperature profiles is shown in Figure 8 for both cases. Figure 9 demonstrates, for different values of the Jeffrey parameter λ_1, the fluctuation in velocity f in the stretching situation, the velocity reduces as the Jeffrey parameter λ_1 grows, and the viscosity of the boundary layer decreases, whereas, in the shrinking case, the velocity decreases as the Jeffrey parameter λ_1 increases, and the thickness of the peripheral layer decreases. Figure 10 demonstrates the impact of λ_1 on the temperature profile for stretching and shrinking cases, and because of the greater temperature and profuse thermal boundary layer, the temperature profile reduces as the Jeffery parameter λ_1 enhances, resulting in a rise in moderation time and a drop-

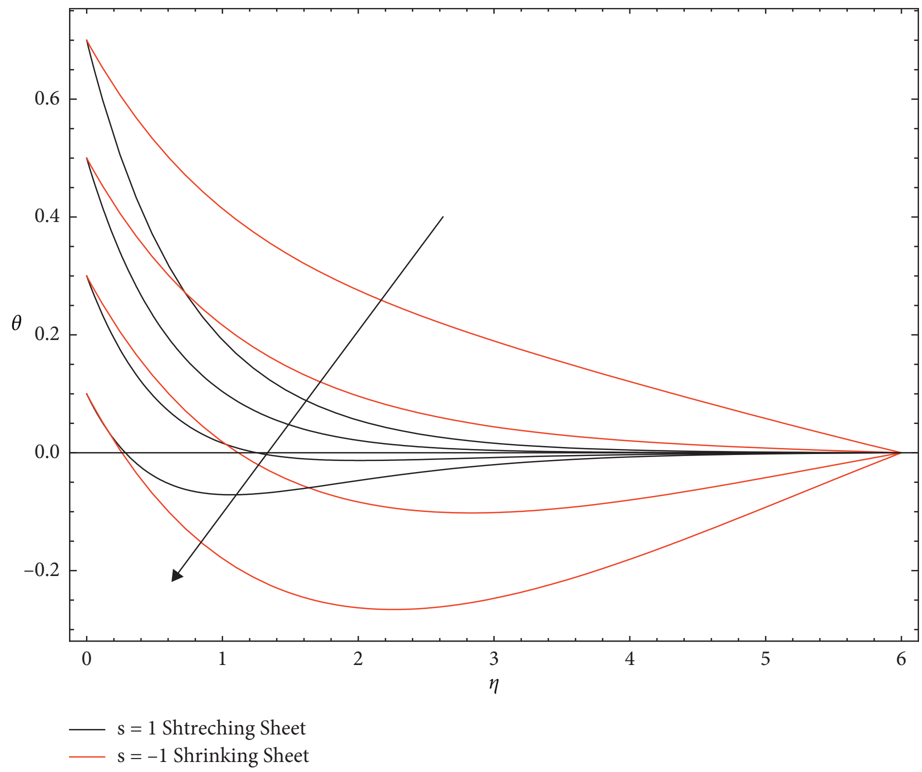

Figure 4: The influence of "e_1" thermal stratification on the temperature profile.

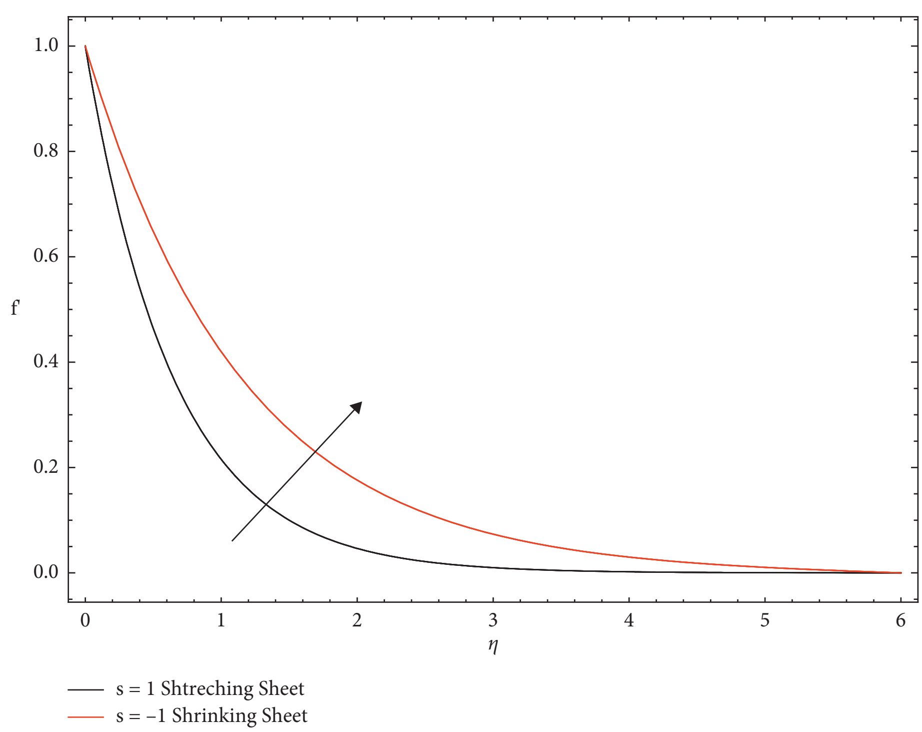

Figure 5: Effects of heat generation/absorption γ on the velocity profile.

in obstruction time. The reason behind the decrease in velocity profile is that, as we increase the values of the Jeffrey fluid parameter, the boundary layer momentum thickness will rise. Hence, the velocity distribution declines as the values rise up. Figures 11 and 12 are plotted the graphs for the porous parameter λ_2 for velocity f' and temperature profile "θ" for both the cases stretching and shrinking. λ_2 porous parameter increases as velocity decreases for both the

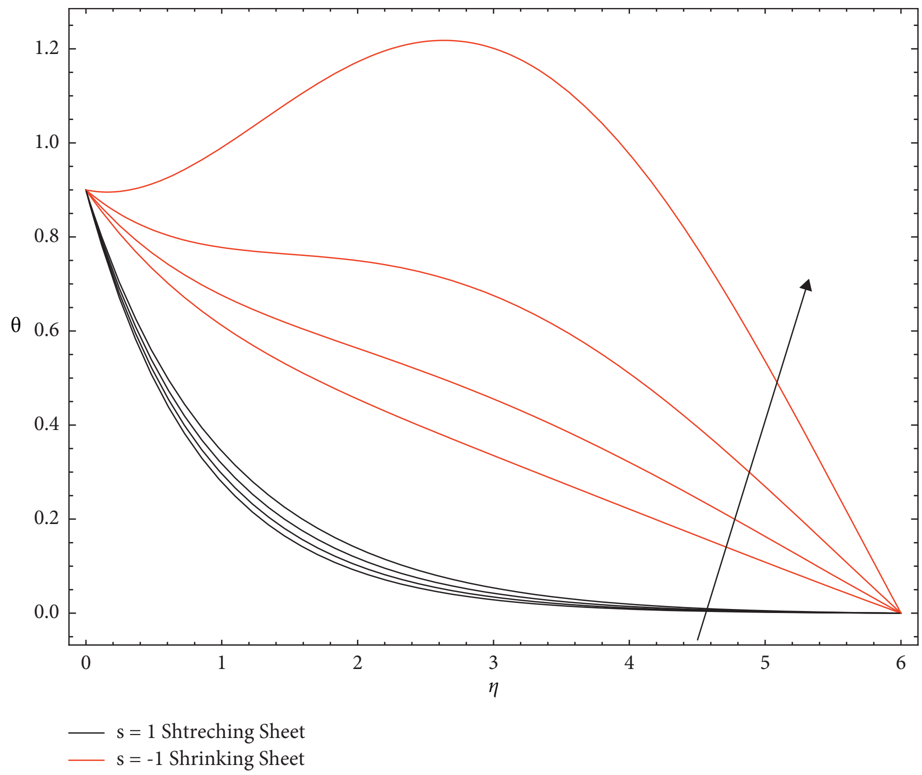

FIGURE 6: Temperature profile effects of heat generation/absorption γ.

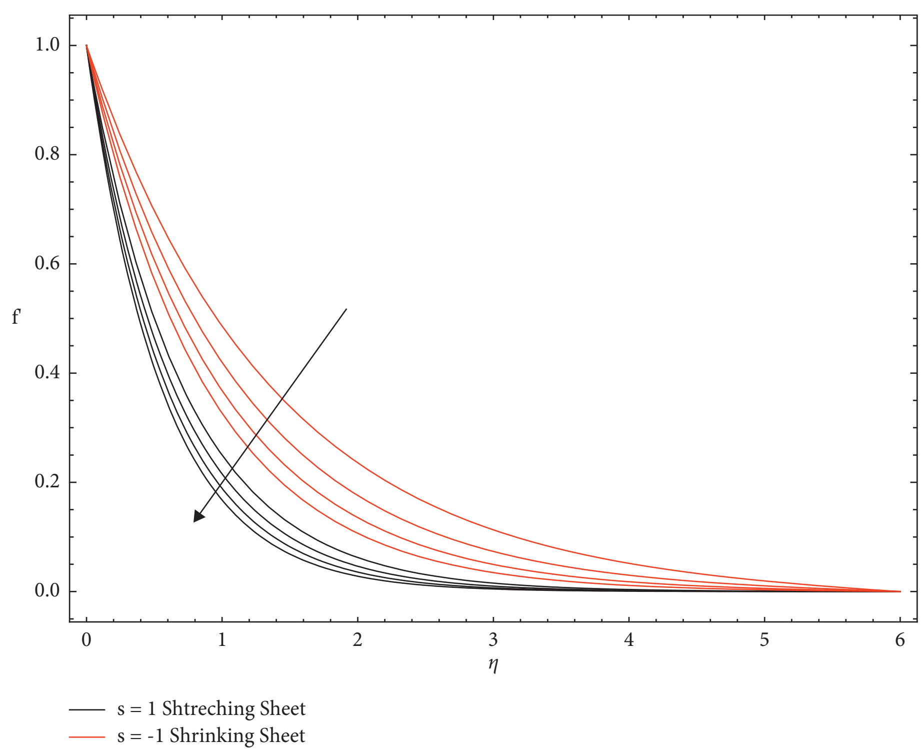

FIGURE 7: The velocity profile on which the magnetic parameter M has an effect.

cases. In temperature profile for different values of λ_2, porous parameter increases as temperature profile decreases in stretching case, but in shrinking case λ_2, porous parameter increases as temperature decreases. The rise in the porosity parameter of the fluid is caused by an increase in the viscosity of the fluid, a drop in the permeability at the edge, or a

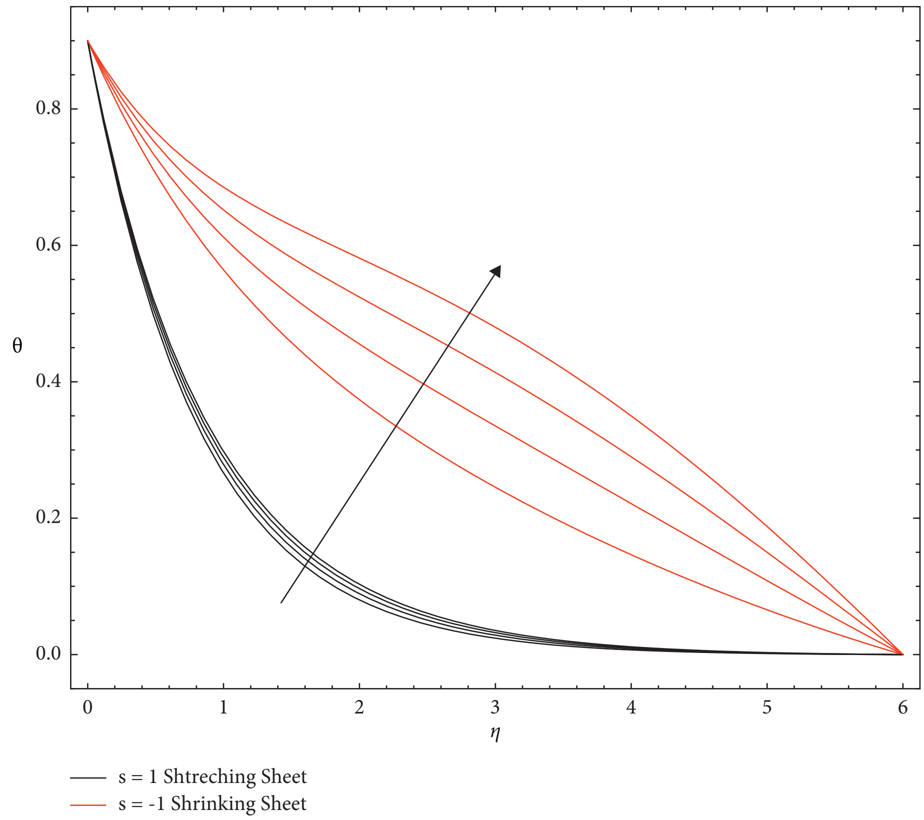

Figure 8: Magnetic parameter M on the temperature profile.

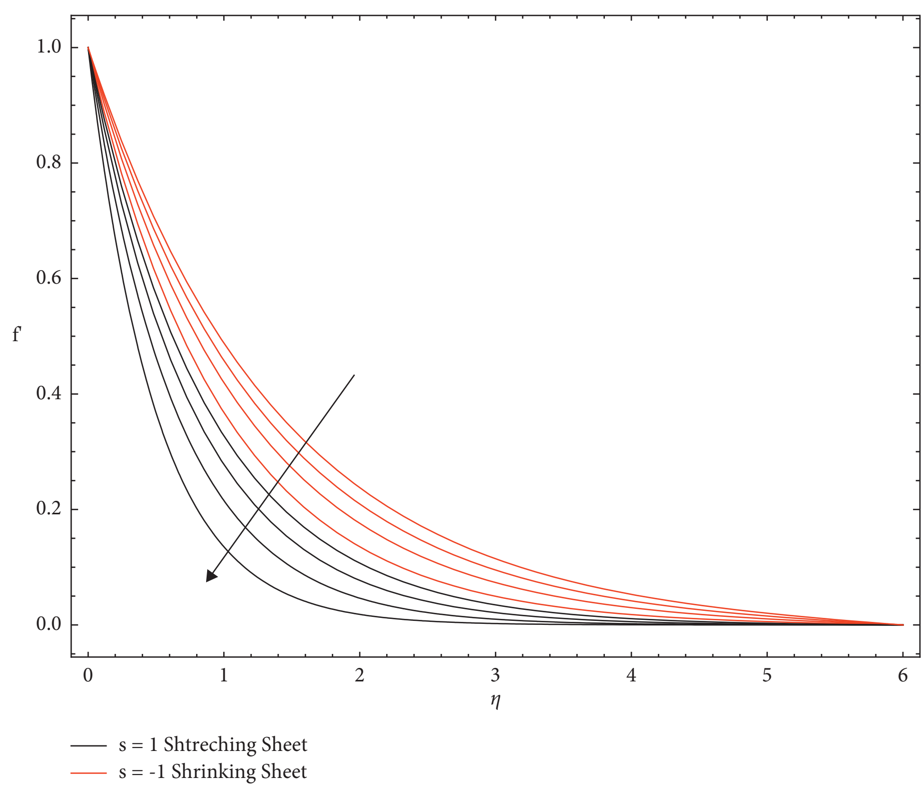

Figure 9: The influence of the Jeffery parameter λ_1 on the velocity profile.

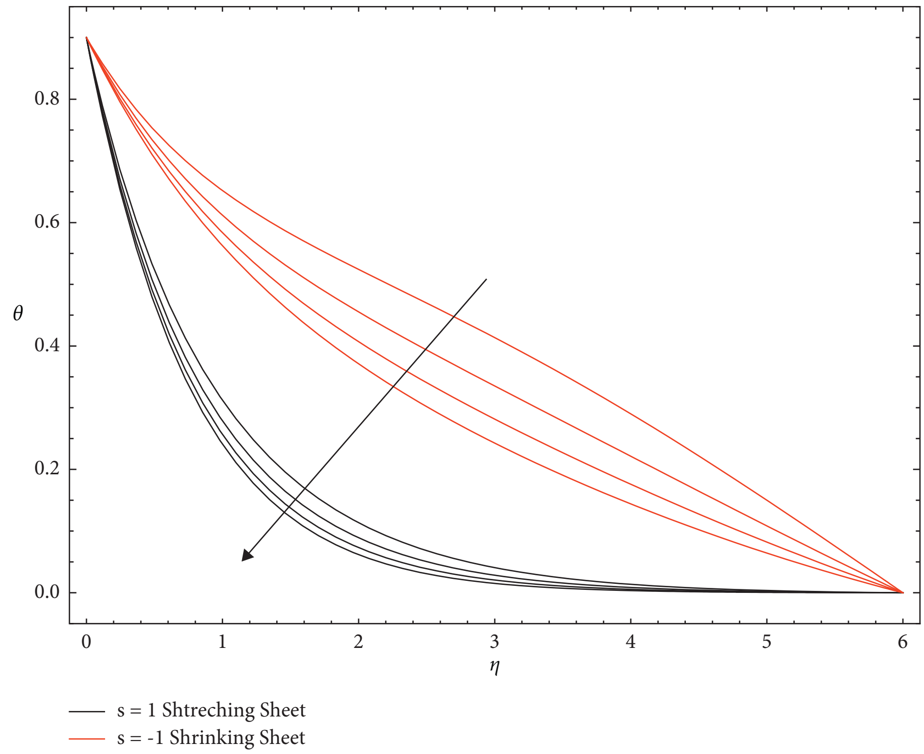

Figure 10: Plots Jeffery parameter λ_1 on the temperature profile.

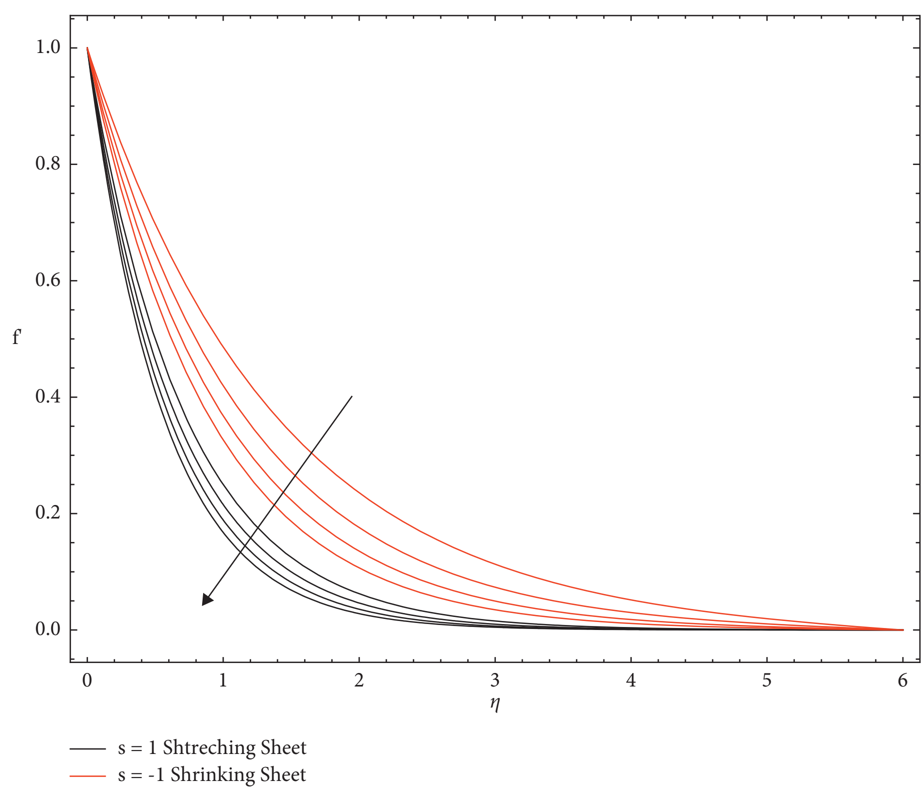

Figure 11: Porous parameter λ_2 on the velocity profile.

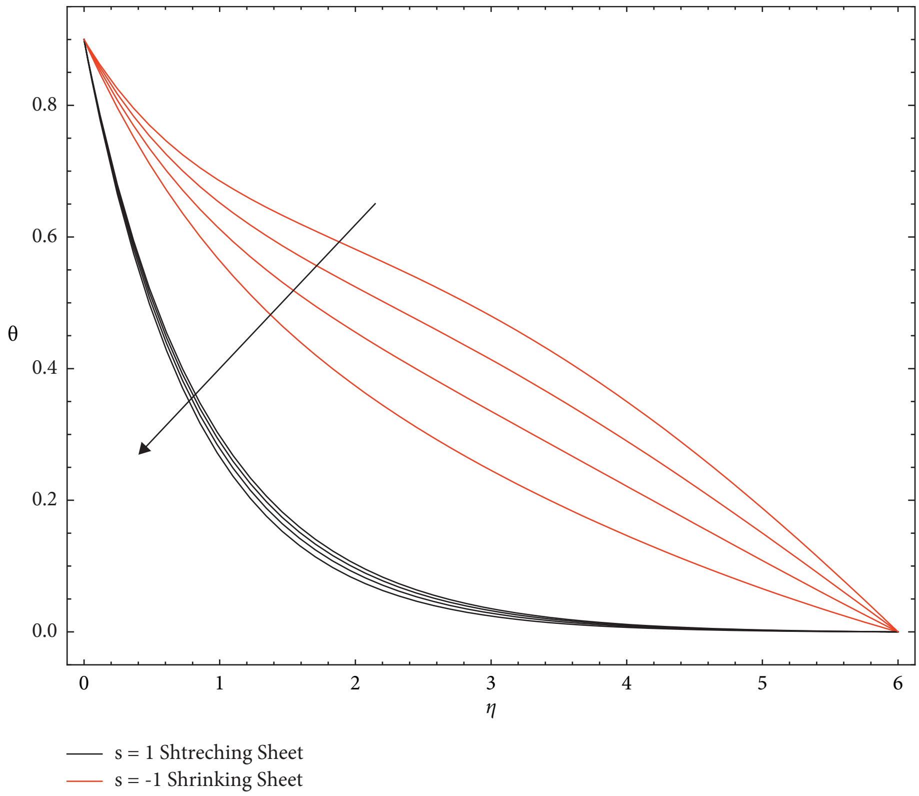

FIGURE 12: Plots porosity parameter λ_2 on the temperature profile.

TABLE 1: The rate of heat transfer $-\theta'$ for different values of b/a.

b/a	Pr	M	S	Bhattacharyya [5]	Dash [17]	Eswara Rao [21]	Present values
−1.24	0.1	0	0	0.128297	0.128166	0.118198	0.118077
−1.24	0.5	0	0	0.098372	0.095886	0.095848	0.095330
−1.24	0.5	1	−1	0.653725	0.598104	0.674000	0.672103
−1	0.71	0	0	—	0.228280	0.228279	0.227102
−1	0.71	1	0	—	0.324963	0.324963	0.323102
−1	0.71	1	0.2	—	0.178289	0.178289	0.164122
−0.5	0.71	1	0.2	—	0.299788	0.299788	0.299786
0	0.71	1	0.2	—	0.402840	0.402840	0.402840
1	0.71	1	0.2	—	0.574088	0.574088	0.574087
−1	7	1	0.2	—	−0.685150	−0.685150	−0.685150

decrease in the stretching rate of the accelerating surface, which results in a progressive reduction in the fluid's flow velocity, as observed.

The Nusselt number is provided in tabular form for various values of specified physical parameters. The following conclusion can be drawn from the current investigation as shown in Table 1.

5. Conclusion

The main focus of this research is on the momentum and heat transfer of boundary layer fluid flow of a Jeffrey fluid in a porous material over a shrinking/stretching sheet. The concept of dimensionless velocity and temperature is also investigated. From the current analysis, we may derive the following conclusions for various values of the stated physical parameters, the Nusselt number, and skin friction [30, 31].

(i) The effects of the Prandtl number on velocity, temperature, and concentration have been observed; the rise in the fluid's Prandtl number is related to increased viscosity.

(ii) The flow for different values of Jeffrey fluid parameter λ_1, on the velocity profile $f'(\eta)$, it is observed that, an increase in the Jeffrey fluid parameter, increases the velocity in the boundary region.

(iii) The thermal stratification parameter e_1's strength can aid in fluid velocity and temperature control. For increasing stratification parameters, the temperature θ (η) of the flowing fluid drops. As e_1

decreases, the temperature differential between the surrounding fluid and the fluid on the surface decreases, lowering the temperature as illustrated.

(iv) For both cases, the λ_2 porous parameter increases as velocity decreases. In the stretching scenario, the λ_2 porous parameter grows as the temperature profile lowers, but in the shrinking situation, the λ_2 porous parameter increases as the temperature decreases.

(v) Finally, raising the absolute value of the heat absorption parameter raises the local Nusselt number whereas increasing the magnetic parameter and the heat generation parameter decreases it.

(vi) The Oldroyd-B fluid model is used to investigate the behavior of blood flow across an abdominal aortic segment in real life (hemodynamics).

Data Availability

The data used to support the findings of this study are available from the corresponding author upon request.

Conflicts of Interest

The authors declare no conflicts of interest.

References

[1] K. B. Pavlov, "Magnetohydrodynamic flow of an incompressible viscous fluid caused by deformation of a surface," *Magnetohydrodynamics*, vol. 10, no. 4, pp. 507–510, 1974.

[2] C. Y. Wang, "Liquid film on an unsteady stretching sheet," *Quarterly of Applied Mathematics*, vol. 48, no. 13, 1990.

[3] M. Miklavcic and C. Y. Wang, "Viscous flow due a shrinking sheet," *Quarterly of Applied Mathematics*, vol. 64, 2006.

[4] A. Ishak, "Similarity solutions for flow and heat transfer over a permeable surface with convective boundary condition," *Applied Mathematics and Computation*, vol. 217, no. 2, pp. 837–842, 2010.

[5] O. D. Makinde, "Similarity solution for natural convection from a moving vertical plate with internal heat generation and a convective boundary condition," *Thermal Science*, vol. 15, no. 1, pp. 137–143, 2011.

[6] O. D. Makinde, "Heat and mass transfer by MHD mixed convection stagnation point flow toward a vertical plate embedded in a highly porous medium with radiation and internal heat generation," *Meccanica*, vol. 47, no. 5, pp. 1173–1184, 2012.

[7] S. Shateyi and O. D. Makinde, "Hydro magnetic stagnation-point flow towards a radically stretching convectively heated disk," *Mathematical Problems in Engineering*, vol. 2013, Article ID 616947, 2013.

[8] R. Ellahi, M. M. Bhatti, A. Riaz, and M. Sheikholeslami, "Effects of magneto hydrodynamics on peristaltic flow of Jeffrey fluid in a rectangular duct through a porous medium," *Journal of Porous Media*, vol. 17, no. 2, 2014.

[9] I. Yakubu Seini and D. Oluwole Makinde, "Boundary layer flow near stagnation-points on a vertical surface with slip in the presence of transverse magnetic field," *International Journal of Numerical Methods for Heat and Fluid Flow*, vol. 24, no. 3, pp. 643–653, 2014.

[10] W. A. Khan, J. R. Culham, and O. D. Makinde, "Combined heat and mass transfer of third-grade nanofluids over a convectively-heated stretching permeable surface," *Canadian Journal of Chemical Engineering*, vol. 93, no. 10, pp. 1880–1888, 2015.

[11] T. Hayat, M. Waqas, S. A. Shehzad, and A. Alsaedi, "MHD stagnation point flow of Jeffrey fluid by a radially stretching surface with viscous dissipation and Joule heating," *Journal of Hydrology and Hydromechanics*, vol. 63, no. 4, pp. 311–317, 2015.

[12] M. A. El-Aziz, "Dual solutions in hydro magnetic stagnation point flow and heat transfer towards a stretching/shrinking sheet with non-uniform heat source/sink and variable surface heat flux," *Journal of the Egyptian Mathematical Society*, vol. 24, pp. 479–486, 2016.

[13] M. Turkyilmazoglu, "Flow of a micro polar fluid due to a porous stretching sheet and heat transfer," *International Journal of Non-linear Mechanics*, vol. 83, pp. 59–64, 2016.

[14] D. H. Babu and P. V. S. Narayana, "Joule heating effects on MHD mixed convection of a Jeffrey fluid over a stretching sheet with power law heat flux: a numerical study," *Journal of Magnetism and Magnetic Materials*, vol. 412, pp. 185–193, 2016.

[15] A. Shahzad, R. Ali, M. Hussain, and M. Kamran, "Unsteady axisymmetric flow and heat transfer over time-dependent radially stretching sheet," *Alexandria Engineering Journal*, vol. 56, no. 1, pp. 35–41, 2017.

[16] M. Eswara Rao and S. Sreenadh, "MHD boundary layer flow of Jeffrey fluid over a stretching/shrinking SH EET through porous medium," *Global Journal of Pure and Applied Mathematics*, vol. 13, no. 8, pp. 3985–4001, 2017.

[17] S. R. Mishra, I. Khan, Q. M. Al-Mdallal, and T. Asifa, "Free convective micropolar fluid flow and heat transfer over a shrinking sheet with heat source," *Case Studies in Thermal Engineering*, vol. 11, pp. 113–119, 2018.

[18] R. M. Eswara and M. Krishna Murthy, "MHD Stagnation point flow of a Jaffrey fluid over a stretching/shrinking sheet through porous medium," *COJEC*, vol. 1, no. 3, Article ID 000512, 2018.

[19] M. Y. Malik and O. D. Makinde, "Parabolic curve fitting study subject to Joule heating in MHD thermally stratified mixed convection stagnation point flow of Eyring-Powell fluid induced by an inclined cylindrical surface," *Journal of King Saud University Science*, vol. 30, no. 4, pp. 440–449, 2018.

[20] P. V. Narayana and D. H. Babu, "Numerical study of a Jeffrey fluid over a porous stretching sheet with heat source/sink," *International Journal of Fluid Mechanics Research*, vol. 46, no. 2, 2019.

[21] D. H. Babu, K. A. Ajmath, B. Venkateswarlu, and P. V. Narayana, "Thermal radiation and heat source effects on MHD non-Newtonian nanofluid flow over a stretching sheet," *Journal of Nanofluids*, vol. 8, no. 5, pp. 1085–1092, 2019.

[22] D. H. Babu1, N. Tarakaramu2, P. V. Satya Narayana, G. Sarojamma, and O. D. Makinde, "MHD flow and heat transfer of a Jeffrey fluid over a porous stretching/shrinking sheet with a convective boundary," *Condition" International Journal of Heat and Technology*, vol. 39, no. 3, pp. 885–894, 2020.

[23] M. Aleem, M. I. Asjad, A. Ahmadian, M. Salimi, and M. Ferrara, "Heat transfer analysis of channel flow of MHD Jeffrey fluid subject to generalized boundary conditions," *The European Physical Journal plus*, vol. 135, no. 1, pp. 1–15, 2020.

[24] K. Kumaraswamy Naidu, D. Harish Babu, S. Harinath Reddy, and P. V. Satya Narayana, "Radiation and partial slip effects on MHD Jeffrey nanofluid containing gyro tactic microorganisms over a stretching surface," *Journal of Thermal Science*

and Engineering Applications, vol. 13, no. 3, Article ID 031011, 2020.

[25] T. Mohamed and M. Bouaziz, “Deep investigation on natural convection flow of a couple stress fluid with nanoparticles in an MHD vertical porous channel with convective boundary conditions,” *Int. J. Heat and Technology*, vol. 38, no. 2, pp. 487–498, 2020.

[26] M. Bilal and S. Ashbar, “Flow and heat transfer analysis of Eyring-Powell fluid over stratified sheet with mixed convection,” *Journal of the Egyptian Mathematical Society*, vol. 28, no. 1, 40 pages, 2020.

[27] M. Afzal, S. Tayyaba, M. Ashraf, M. Hossain, M. Uddin, and N. Afzulpurkar, “Simulation, fabrication and analysis of silver based ascending sinusoidal microchannel (ASMC) for implant of varicose veins,” *Micromachines*, vol. 8, no. 9, p. 278, 2017.

[28] M. Afzal, M. Ashraf, S. Tayyaba, M. Hossain, and N. Afzulpurkar, “Sinusoidal microchannel with descending curves for varicose veins implantation,” *Micromachines*, vol. 9, no. 2, p. 59, 2018.

[29] S. Tayyaba, M. W. Ashraf, Z. Ahmad, N. Wang, M. J. Afzal, and N. Afzulpurkar, “Fabrication and analysis of polydimethylsiloxane (PDMS) microchannels for biomedical application,” *Processes*, vol. 9, p. 57, 2021.

[30] L. J. Crane, “Flow past a stretching plate,” *Zeitschrift für Angewandte Mathematik und Physik*, vol. 21, pp. 645–647, 1970.

[31] O. D. Makinde and A. Aziz, “Boundary layer flow of a nanofluid past a stretching sheet with a convective boundary condition,” *International Journal of Thermal Sciences*, vol. 50, no. 7, pp. 1326–1332, 2011.

Hindawi
Mathematical Problems in Engineering
Volume 2022, Article ID 5371716, 9 pages
https://doi.org/10.1155/2022/5371716

Research Article

Comparative Study to Analyze MEMS Based Microrobot Using Fuzzy TOPSIS Approach

Ammar Oad ,[1,4] Shahzadi Tayyaba ,[2] Muhammad Waseem Ashraf ,[3] Dong Feng,[1] Gaofeng Luo,[1] and Maham Akhlaq[3]

[1]*Faculty of Information Engineering, Shaoyang University, Shaoyang 422000, China*
[2]*Department of Computer Engineering, University of Lahore, Lahore, Pakistan*
[3]*Department of Physics (Electronics), Government College University, Lahore, Pakistan*
[4]*Information Technology Center, Sindh Agriculture University, Tando Jam 70060, Pakistan*

Correspondence should be addressed to Ammar Oad; ammar.oad@hnsyu.edu.cn and Muhammad Waseem Ashraf; dr.waseem@gcu.edu.pk

Received 6 March 2022; Revised 4 May 2022; Accepted 31 May 2022; Published 29 June 2022

Academic Editor: Ardashir Mohammadzadeh

With the emergence in the field of developing small-scale systems, microrobots are gaining enormous attention due to their small size, wide number of application, and negligible effects on the surrounding. MEMS and microrobots both have electrical and mechanical parts which are situated on a single device and chip. This makes MEMS based microrobots and an excellent device due to its ease of fabrication and small size. MEMS-based microrobots have a wide number of applications in the field of bio-medical special drug delivery and invasive surgery. These tiny robots can be sent into the human body to send any medicine inside the human body. Various types of MEMS based microrobot can be used in drug delivery applications including magnetic nanoparticles based microrobots, magnetized spirulina microrobot, and electro-magnetic microrobots. However, the suitability of all these robots for drug delivery applications depends on the locomotion, navigation controlling, shape transformation, actuation requirement, and amount of drug wasted before moving to the destination. In this work, fuzzy rules based system is performed to confirm the dependence of the parameters including the locomotion, navigation controlling, shape transformation, actuation requirement, and amount of drug wasted on the working of microrobots in drug delivery applications. Similarly, fuzzy TOPSIS based study is performed to compare and analyze the most suitable microrobot for drug delivery application. Piezo-electric and electro-magnetic microrobots are considered the most suitable option with relative closeness to the ideal solution of 0.71 and 0.66, respectively, owing to their better shape transformation and movement.

1. Introduction

Automation in the industry is getting enormous attention owing to its excellent use in increasing the productivity and efficiency of industrial units [1, 2]. To achieve automation, robotic systems are widely used in industry. These robotic systems range from large size as well as nano-sized robots with different functionalities [3]. Among these types of robots, microrobots consist of mechanical and electric parts which is similar to the micro-electromechanical system (MEMS) [4]. Microrobots on a single chip with both electric and mechanical parts are categorized as MEMS microrobots [5, 6]. MEMS based system is designed on the basis of their actuation, sensing, structural, and electronic circuit. On microscale, microrobots also consist of these components in which they sense the environment based on the microstructure properties, and the electronic circuit then responds to the sensing data by actuating it.

Actuating can be moving from one place to another or to carry out a work based on the sensing data. The basic components along with their few basic types for MEMS based systems are shown in Figure 1. MEMS technology is expected to have an impact on microrobots in three ways. These ways include providing sensing and actuation, introducing a better and intelligent system, and providing autonomous distributive systems. With its small size and excellent applications, microrobots are considered an important constituent in the bio-medical industry. It has several applications in disease diagnosis, health monitoring, tissue engineering, invasive surgery, drug delivery, and cell manipulation [7–10].

Reported small-scale bio-medical robot sizes use range from tens of micrometers to several centimeters. Typically, the dimensions of a single biomedical MEMS microrobot are less than 1 mm and larger than 1 μm that can work on microscale forces. Thus, for microrobots, bulk forces such as inertial forces and buoyancy are negligible in comparison with its size. These parameters include surface tension, adhesion, viscous forces, friction, and drag. Microsized medical robots are used in surgical procedures which can be static or moveable [11, 12]. There are two main ways of designing, building, and controlling moveable biomedical microrobots including the following:

(i) On-board approach: similar to a typical robot which is self-contained and self-propelled, the miniature robot with components on-board has the capability to operate on its own.

(ii) Off-board approach: off-board microrobots have their components attached externally. All the actuation, sensing, and controlling parts are externally connected to the sensor.

In the various fields of biomedical engineering, drug delivery is considered as an important method to send various different types of drugs and medicines to various different parts of the human body. Microrobots of various different actuation principles have been used in the biomedical engineering field. Figure 2 shows microrobots of different types used in bio-medical applications. Various on-board as well as off-board microrobots have been reported in the literature which can be used in drug delivery using microrobots. Microrobots have the potential which makes them usually for application including real-time tissue controlling and complex drug delivery to the human body [13, 14]. However, it faces issues including its proper locomotion within the human body, navigation controlling, shape transformation, drug wastage, ease of fabrication, difficulty in controlling, and actuation principle as well as design.

Various MEMS based magnetic and piezo-electric robots are used which helps in providing an ease in drug delivery throughout the human body. However, their work is highly affected by the use of different types of actuation principles as well as materials to fabricate the microrobots [20, 21]. Various different types of microrobots that can be used for drug delivery include hydrogel microrobot, piezo-electric microrobot, magnetic nanoparticles based microrobots, magnetized spirulina microrobot, and electro-magnetic microrobots [22–26]. These various robots show issues in terms of drug wastage, slow motion and navigation, requirement of high actuation, and shape transformation. Koleoso et al identify various different types of microrobots which can provide magnetic actuation for drug delivery as well as for different other biomedical applications. In terms of MEMS based microrobots, these different microrobots can be defined in terms of a single lab of chip device (under the on-board approach) and can be categorized as an excellent way to improve the use of microrobots in drug delivery applications.

In this work, various different microrobots used for drug delivery including hydrogel microrobot, piezo-electric microrobot, hydrogel microrobot, and electro-magnetic microrobots are categorized in terms of MEMS based microrobots. The effect of the above-stated robots on the basis of 3D locomotion, stationary controlling, navigation controlling, shape transformation, drug wastage, ease of fabrication, and magnetic field requirement is analyzed using TOPSIS. The proposed system has application in the field of bio-medical including drug delivery, invasive surgery, dental, and other applications.

2. Methodology

In this work, the selected microrobots are analyzed for their dependent parameters using a fuzzy rule based system. After analyzing the effect of the parameters on the microrobot, the best microrobot for bio-medical application is analyzed using the TOPSIS study. The block diagram of the work is shown in Figure 3.

2.1. Fuzzy Analysis. The fuzzy analysis is carried out in the MAMDANI model for the three different microrobots and its effect on the output including 3D locomotion, navigation controlling, ease to fabricate, shape transformation, and drug wastage. The input hydrogel microrobot, piezo-electric microrobot, and electro-magnetic microrobots and output parameters are shown in Figure 4. Three membership functions are defined for all the inputs and outputs as shown in Figures 5 and 6. The ranges for the inputs and outputs are selected from 0 to 1. The membership function includes low, medium, and high. The low membership function has a range of 0–0.25, the medium membership function has a range of 0.20–0.80, and the high membership function has a range of 0.7–1.

Totally, 27 rules are then defined in terms of literature and theories. On the basis of the theories, 3D graphs are plotted which show the relationship between inputs and outputs. The graphs show that the robots significantly affect the motion, movement, and working of the robot. The rule viewer based on the fuzzy analysis is shown in Figure 7.

Based on the simulated values, the output crisp values are calculated based on the input crisp value from the rule viewer and the MAMDANI formula. The Minimum membership function for the MAMDANI formula is calculated using the input crisp values from the rule viewer.

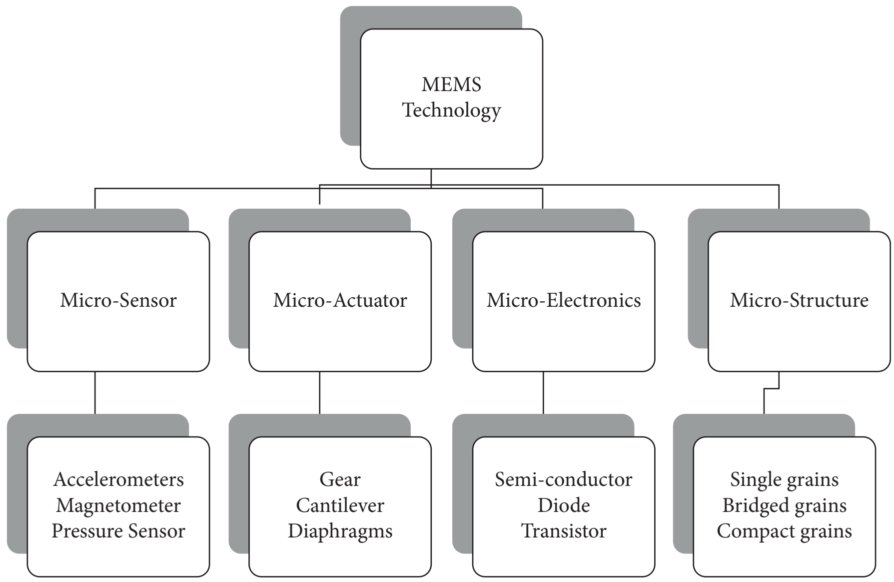

FIGURE 1: Basic components of MEMS based systems.

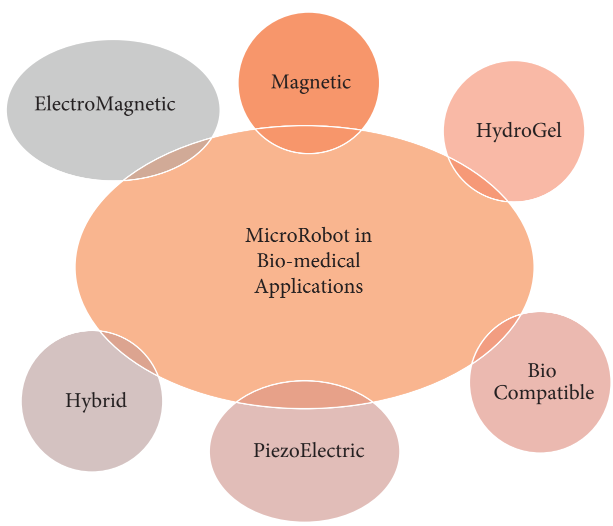

FIGURE 2: Microrobots used in bio-medical applications [15–19].

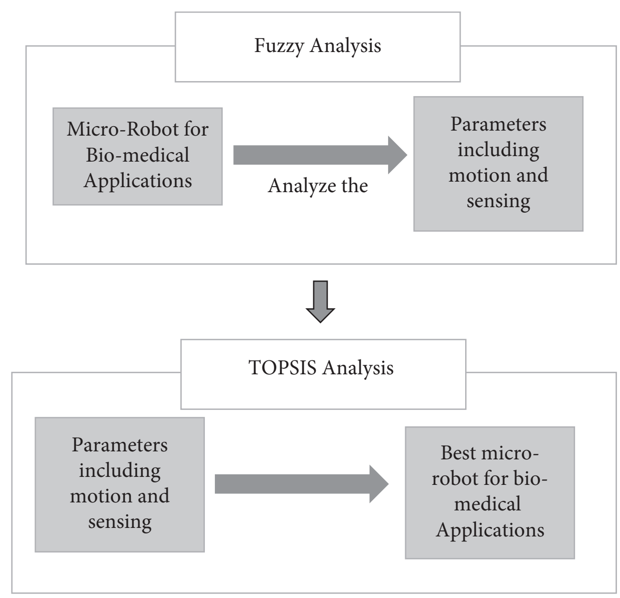

FIGURE 3: Block diagram for the proposed methodology.

Table 1 shows the simulated values from the crisp values and calculated values using the MAMDANI model. The error between the values is less than 1% which shows the accuracy of the system. Similarly, the dependence of all the three inputs microrobots also depends on the output 3D locomotion, navigation controlling, ease of fabrication, shape transformation, and drug wastage.

2.2. TOPSIS Study. TOPSIS is considered a way to do multicriteria decision-making for the determination of an ideal solution. To carry out the TOPSIS study, the following steps are taken.

(1) Various different criteria and attributes are selected. In this work, attributes include piezo-electric, electro-magnetic, and hydrogel microrobots, and the criteria on which the attributes are checked include 3D locomotion, ease of fabrication, navigation controlling, shape transformation, and drug wastage.

(2) After finalizing the attributes and criteria, the relative behavior of each factor is analyzed.

(3) The attributes are now checked based on the feedback from the literature review and experts to check the effect of attributes on the criteria. The marked attributes on the basis of criteria are in terms of 0–10.

(4) With the rating, the average attributes are finalized along with the decision matrix.

(5) The entities in the decision matrix are calculated as Xij.

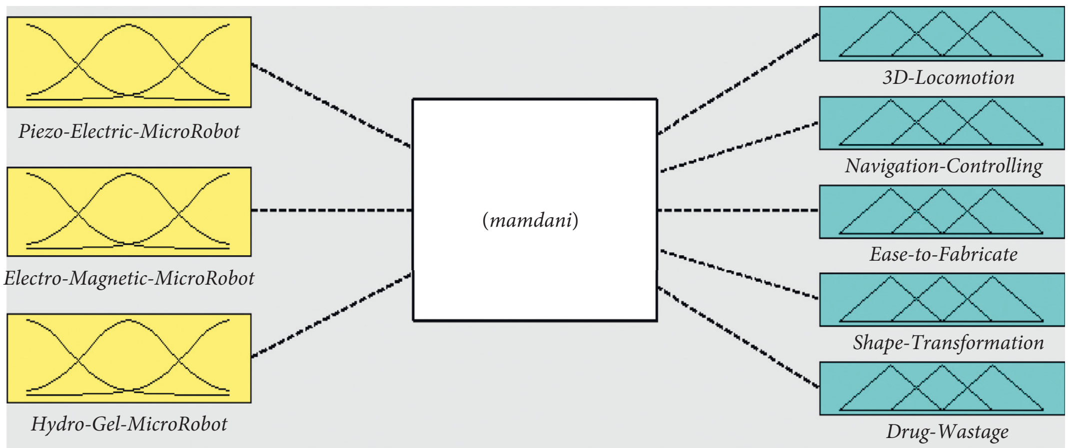

FIGURE 4: FIS figure of the fuzzy rule based system.

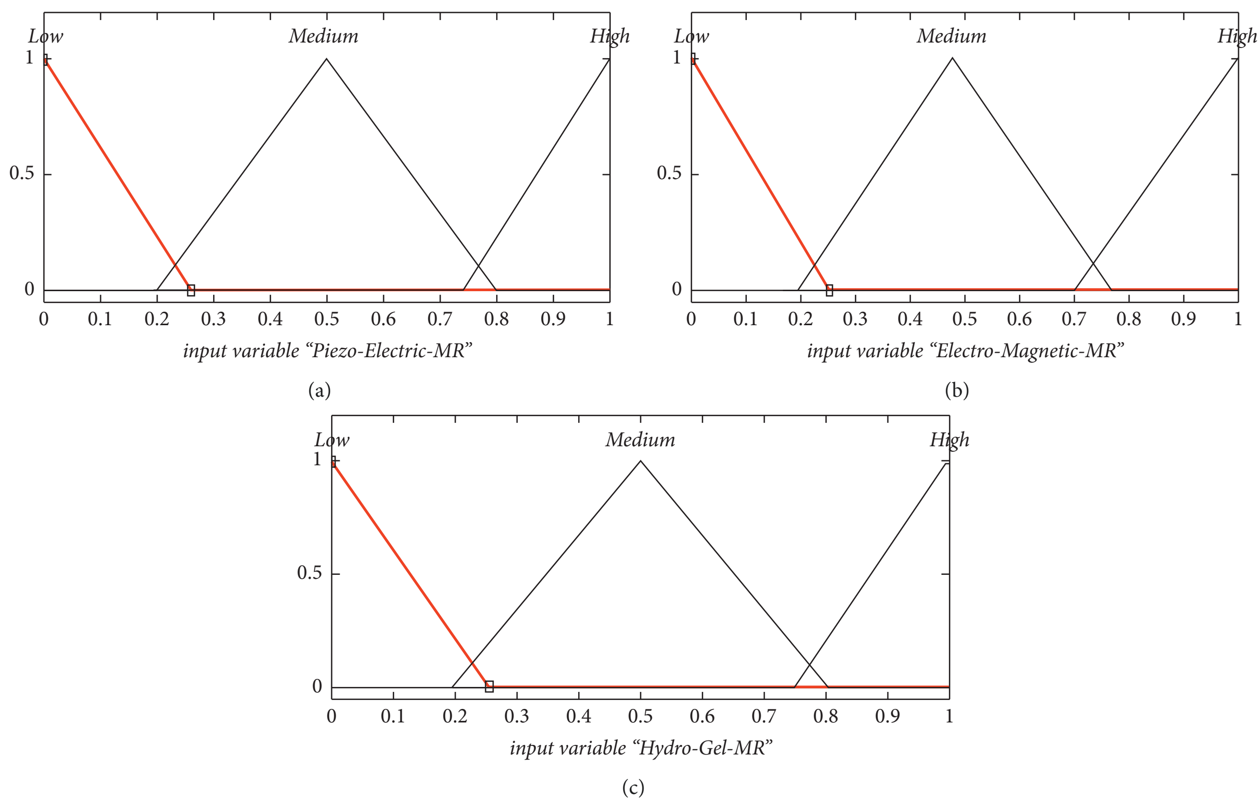

FIGURE 5: Membership function for input. (a) Piezo-electric microrobot. (b) Electro-magnetic microrobot. (c) Hydro-gel microrobot.

(6) After the entities are calculated, they are multiplied with each weight attributed.

(7) The ideal and nonideal solutions are calculated. The ideal solution is calculated by using the formula stated in the following equation:

$$\mathbf{S_i^+} = \sum_{\mathbf{j=1}}^{\mathbf{m}} \left[\left(\mathbf{V_{ij}} - \mathbf{V_J^+} \right)^2 \right]^{0.5}, \tag{1}$$

where the positive ideal solution is represented by Vj^+, and the positive ideal solution is represented by Vj^-.

(9) The separation to the ideal solution is then determined using the formula in the following equation:

$$\mathbf{S_i^-} = \sum_{\mathbf{j=1}}^{\mathbf{m}} \left[\left(\mathbf{V_{ij}} - \mathbf{V_J^-} \right)^2 \right]^{0.5}. \tag{2}$$

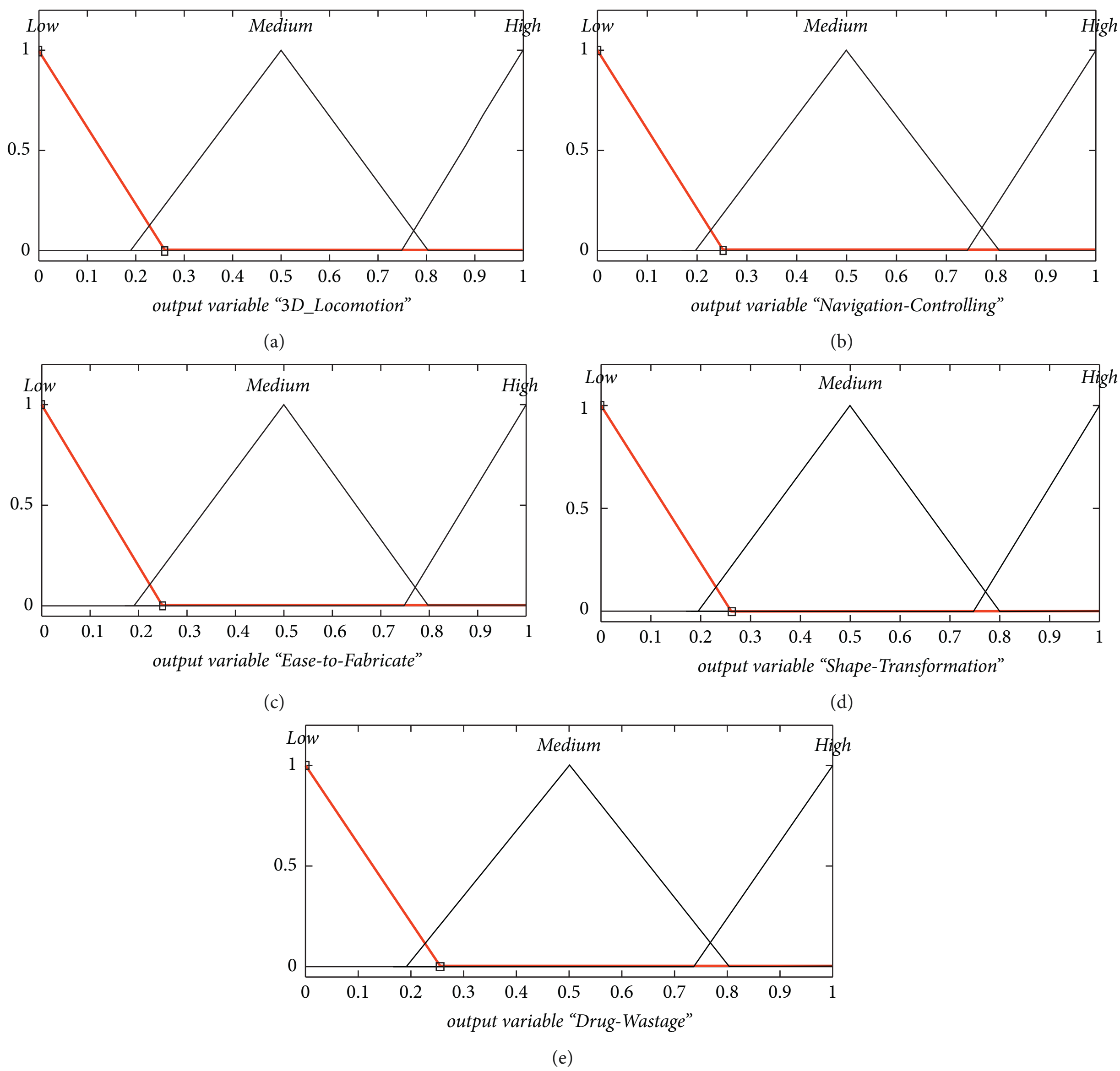

FIGURE 6: Membership functions for output. (a) 3D locomotion. (b) Navigation controlling. (c) Ease to fabricate. (d) Shape transformation. (e) Drug wastage.

(10) Relative closeness to the ideal solution is analyzed using the following formula:

$$\mathbf{P_i} = \frac{\mathbf{S_i^-}}{\mathbf{S_i^+} + \mathbf{S_i^-}}. \tag{3}$$

3. Fuzzy TOPSIS for Microrobots

In this work, microrobots including MEMS based piezo-electric microrobots, electro-magnetic microrobot, and hydro-gel microrobot are analyzed on the basis of 3D locomotion, navigation controlling, ease of fabrication, shape transformation, and drug wastage. Initially, the attributes and criteria are defined. For all three attributes, the criteria are defined based on a scientific research article. The selected information from the articles is analyzed to predict the possible attribute and criteria. The alternative which is the microrobots is numbered as R1, R2, and R3: R1 for piezo-electric microrobots, R2 for electro-magnetic microrobot, and R3 for hydro-gel microrobot. Attributes include 3D locomotion (A1), navigation controlling (A2), ease to fabricate (A3), shape transformation (A4), and seat drug wastage (A5). In terms of a fuzzy logic system, the attributes are converted into linguistic terms using the basic fuzzy triangular based system as shown in Figure 8. Linguistic terms including VS, S, M, L, and VL are taken.

Fuzzy numbers associated with the linguistic terms are shown in Table 2.

On the basis of the fuzzy ranges, the literature review is carried out to analyze the effect of parameters alongside the attributed weights designed. Table 3 shows the attribute weights designed based on literature review and fuzzy TOPSIS system.

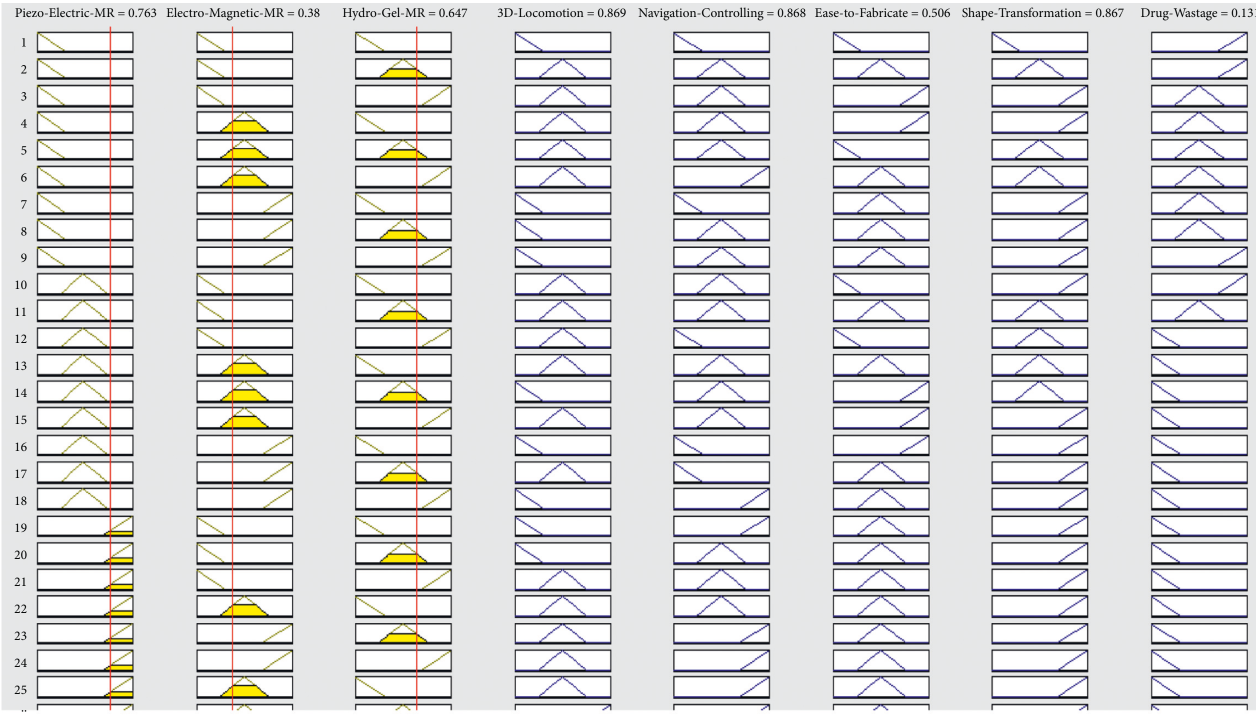

Figure 7: Rule viewer for the fuzzy analysis.

Table 1: Error between simulated and MAMDANI model calculated values.

	Simulated	Calculated	Error
3D locomotion	0.870	0.865	0.57
Navigation controlling	0.868	0.864	0.46
Ease of fabrication	0.506	0.51	0.78
Shape transformation	0.868	0.87	0.22
Drug wastage	0.131	0.135	0.5

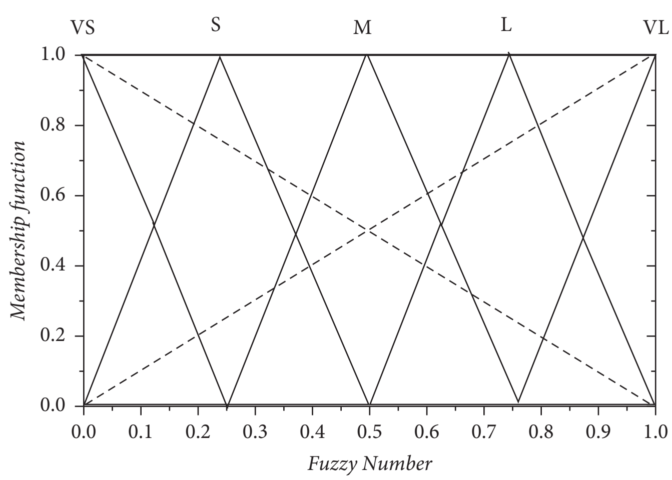

Figure 8: Linguistic terms for fuzzy logic number conversion.

Positive and negative ideal solutions are calculated which predict the best MEMS based microrobot for drug delivery. The negative ideal alternative shows the least suitable MEMS based microrobot for drug delivery application.

4. Results and Discussion

The decision matrix and the weighted standardized decision matrix (V_{ij}) are calculated for this work which is shown in Table 4.

Table 2: Linguistic terms and their ranges.

Linguistic Term	Range	Average
VS	0,0,0.3	0.1
S	0,0.3,0.5	0.26
M	0.3,0.5,0.7	0.5
L	0.5,0.7,1	0.7
VL	0.7,0.7,1	0.8

Table 3: Attributed weights for microrobots.

Criteria	Attributed weights (Wj)		
	Piezo-electric microrobots	Electro-magnetic microrobot	Hydro-gel microrobot
3D locomotion	9	8	7
Navigation controlling	7	7	8
Ease to fabrication	9	9	6
Shape transformation	7	6	6
No drug wastage	7	7	6

Table 4: Weighted standardized decision matrix (Vij) for all microrobots.

Criteria	Weighted standardized decision matrix (Vij)		
	Piezo-electric microrobots	Electro-magnetic microrobot	Hydro-gel microrobot
3D locomotion	0.13	0.114	0.1
Navigation controlling	0.055	0.055	0.063
Folding and unfolding based on temperature	0.147	0.22	0.147
Shape transformation	0.256	0.23	0.22
No drug wastage	0.272	0.25	0.23

The ideal solution and negative ideal solution are now calculated by using the formula stated below, and the ideal solution means the most suitable microrobot with the best parameters. The ideal solution is calculated using the following as shown in equation (1).

A negative ideal solution means the microrobots which is most unsuitable for use in drug delivery application and is not suitable for all the decision criteria. The negative ideal solution is calculated using the formula as shown in equation (2).

Relative closeness to the ideal solution is calculated using the formula as given in equation (3).

Table 5 shows the ideal solution and its closeness to the result. The ideal solution in this work is considered the best MEMS microrobot for drug delivery applications.

Piezo-electric and electro-magnetic microrobots show better results in terms of different factors including locomotion, navigation, shape transformation, and drug wastage. However, a piezo-electrically driven microrobot can be more beneficial in terms of other robots. This is due to the fact that the net flow in such microrobots is high which results in more accurate delivery of drug towards the sample. Similarly, thinner these types of microrobots can easily move towards thinner veins like arteries and capillaries due to their better navigation and travelling speed. This makes piezo-electric microrobots an excellent choice for use in bio-medical applications. Similarly, it provides better micropositioning and manipulation along with higher resolution, low cost, ease to fabricate, and small size suitable to be inserted in the human body for various different bio-medical applications.

Table 6 shows the benchmark table with respect to the literature review. It described the comparison between the fuzzy TOPSIS method used in various different fields using microrobots. These fields include its application in industrial arc welding, military industry, and overall multiple applications. Methods used include fuzzy TOPSIS, fuzzy AHP, and TOPSIS entropy method which are categorized as different multicriteria decision-making techniques for TOPSIS analysis.

As seen in all other applications of MEMS based microrobots, the basic parameters including its cost, availability, speed, accuracy, repeatability, ease of fabrication, capacity, and consumption have been analyzed for microrobots used in various different industries as shown in Table 6. This work however helps to provide multicriteria decision-making in predicting the best MEMs based microrobot for bio-medical application (drug delivery) for the basic parameters. Piezo-electric and electro-magnetic microrobots are considered the most suitable option for use as microrobot for drug delivery applications owing to their better shape transformation and movement.

TOPSIS provides the solution as a single ideal solution based on the decision-maker's proposed criteria and alternatives. Other multicriteria decision-making techniques including VIKOR, AHP, and BWM can be used in order to analyze and simulate the selection of microrobot. However, TOPSIS and VIKOR are considered the most suitable type of MCDM due to their work in the selection of alternatives in the existence of contradictions, number of alternative

Table 5: Closeness to the ideal solution for the microrobot.

Parameters	Piezo-electric microrobot	Electro-magnetic microrobot	Hydro-gel microrobot
S_i^+	0.035	0.05	0.078
S_i^-	0.088	0.10	0.034
$S_i^+ + S_i^-$	0.123	0.15	0.112
$S_i^- / S_i^+ + S_i^-$	0.71	0.66	0.329

Table 6: Benchmark table.

	Application	Parameters	Method	Remarks
Chu [27]	Multiple applications	Cost, load capacity, man–machine interface, availability of diagnostic software	Fuzzy TOPSIS method	Analysis of objective and subjective attribute
Chodha [28]	Industrial arc welding	Mechanical weight, repeatability, payload capacity, maximum reach, average power consumption	TOPSIS-entropy technique	Entropy weights method used for assigning attributes
Simion [29]	Military industry	High speed, accuracy, large arm reach, reduced dimensions of the robot's body, and arm, high flexibility, and reduced cost	MCDM (AHP method)	Industrial robots with different technical specifications
This work	Bio-medical applications	3D locomotion, stationary controlling, navigation controlling, shape transformation, drug wastage, ease of fabrication	Fuzzy TOPSIS method	Predicting the best robot for drug delivery application

processes and criteria, agility through the process of decision-making, computational complexity, adequacy in supporting a group decision, and addition or removal of a criterion [30].

The main contribution of this work includes providing a multicriteria decision-making method to predict the most suitable and sustainable type of microrobot from biomedical applications mainly drug delivery. This will help to improve the quality of drug delivery with better efficiency by using the proposed microrobot.

5. Conclusion

Microrobots are becoming an essential part of use in biomedical and other applications. Microrobots are becoming more popular and useful for invasive surgery, drug delivery, and pumping fluid. However, the suitability of the robot to be used is an important issue while using microrobot for biomedical application. This work shows the application of various different micropumps for use in drug delivery application by analyzing the output parameters of microrobots. Piezo-electric microrobots, electro-magnetic microrobots, and hydrogel microrobots are analyzed in this work, and fuzzy rule based system significantly shows the effect of these microrobots on the 3D locomotion, navigation controlling, shape transformation, ease of fabrication, and drug wastage. The rule-based fuzzy system provided authentic structure for fuzzy set and uncertainty handling susceptibility generated by the formally used fuzzy system. Fuzzy TOPSIS study is carried out which shows that the piezo-electric microrobots have the best closeness to the ideal solution of 0.71 as compared to other microrobots for use in drug delivery. For the electro-magnetic micropump and hydrogel micropump, the closeness to the ideal solution is 0.66 and 0.329, respectively. The scientific reason includes better and enhanced movement of the drug in the narrow medium as well as excellent micropositioning. The implementation of these sensors on the basis of their parameters in other applications including electronics, optics, material science, and mechanical systems can be carried out in the future. In the future, the interval-type fuzzy type 3 can be implemented in order upper and lower bounds of the membership function ranges are not constant, but they are fuzzy sets. This will help reduce the uncertainty and noise in the resulting fuzzy rule based system because the dependence on linguistic values decreases. These simulation results may be useful for fabrication of microrobots for biomedical applications.

Data Availability

All data are included within the manuscript, and more detail can be made available upon request from the corresponding authors.

Conflicts of Interest

The authors declare no conflicts of interest.

Acknowledgments

The authors would like to acknowledge the Faculty of Information Engineering, Shaoyang University, Shaoyang, China; Department of Physics (Electronics), GC University Lahore, Pakistan; Department of Computer Engineering, University of Lahore, Pakistan; and Information Technology Center, Sindh Agriculture University Tando Jam, Pakistan for their help, and guidance to carry out the research work.

References

[1] A. K. Inkulu, M. V. A. R. Bahubalendruni, and A. Dara, "Challenges and opportunities in human robot collaboration context of Industry 4.0 - a state of the art review," *Industrial Robot: The International Journal of Robotics Research and Application*, vol. 49, no. 2, pp. 226–239, 2021.

[2] V. G. Pratheep, T. Tamilarasi, K. Dhileephan et al., "Design and fabrication of multitasking transit robot," *IOP Conference Series: Materials Science and Engineering*, vol. 1057, no. 1, Article ID 012034, 2021.

[3] A. K. Basu, A. Basu, S. Ghosh, and S. Bhattacharya, *Introduction to MEMS in Biology and Healthcare*, AIP Publishing LLC, Melville, NY, USA, 2021.

[4] R. Garcia-Ramirez and S. Hosseini, "History of bio-microelectromechanical systems (BioMEMS)," in *BioMEMS*, pp. 1–20, Springer, Berlin, Germany, 2021.

[5] D. Wang, H. Xie, L. Thomas, and S. J. Koppal, "A miniature LiDAR with a detached MEMS scanner for micro-robotics," *IEEE Sensors Journal*, vol. 21, no. 19, pp. 21941–21946, 2021.

[6] B. Sun, G. Wood, and S. J. S. Miyashita, "Milestones for autonomous in vivo microrobots in medical applications," *Surgery*, vol. 169, no. 4, pp. 755–758, 2021.

[7] B. Ahmad, M. Gauthier, G. J. Laurent, and A. J. I. T. o. R. Bolopion, "Mobile microrobots for in vitro biomedical applications," *Surveyor*, vol. 38, 2021.

[8] W. Chen, X. Fan, M. Sun, and H. J. M. Xie, "The cube-shaped hematite microrobot for biomedical application," *Mechatronics*, vol. 74, Article ID 102498, 2021.

[9] D. Folio, *Magnetic Microrobotics for Biomedical Applications*, Université d'Orléans, Orléans, France, 2021.

[10] D. Zhang, "Perception and manipulation of microrobots via optical tweezer," Thesis or Dissertation, Imperial College London, London, UK, 2021.

[11] A. Aghakhani, O. Yasa, P. Wrede, and M. Sitti, "Acoustically powered surface-slipping mobile microrobots," *Proceedings of the National Academy of Sciences*, vol. 117, no. 7, pp. 3469–3477, 2020.

[12] Z. Lao, N. Xia, S. Wang, T. Xu, X. Wu, and L. J. M. Zhang, "Tethered and untethered 3D microactuators fabricated by two-photon polymerization: a review," *Micromachines*, vol. 12, no. 4, p. 465, 2021.

[13] S. Pané, P. Wendel-Garcia, Y. Belce, X.-Z. Chen, and J. Puigmartí-Luis, "Powering and fabrication of small-scale robotics systems," *Current Robotics Reports*, vol. 2, no. 4, pp. 427–440, 2021.

[14] J. Choi, J. Hwang, J.-y. Kim, and H. Choi, "Recent progress in magnetically actuated microrobots for targeted delivery of therapeutic agents," *Advanced Healthcare Materials*, vol. 10, no. 6, Article ID 2001596, 2021.

[15] E. Doutel, F. J. Galindo-Rosales, and L. Campo-Deaño, "Hemodynamics challenges for the navigation of medical microbots for the treatment of CVDs," *Materials*, vol. 14, no. 23, p. 7402, 2021.

[16] A. V. Singh, M. Ansari, M. Mahajan et al., "Sperm cell driven microrobots—emerging opportunities and challenges for biologically inspired robotic design," *Micromachines*, vol. 11, no. 4, p. 448, 2020.

[17] S. Jeon, A. K. Hoshiar, K. Kim et al., "A magnetically controlled soft microrobot steering a guidewire in a three-dimensional phantom vascular network," *Soft Robotics*, vol. 6, no. 1, pp. 54–68, 2019.

[18] L. Yang, L. J. A. R. O. C. Zhang, and A. Systems, "Motion control in magnetic microrobotics: from individual and multiple robots to swarms," *Annual Review of Control, Robotics, and Autonomous Systems*, vol. 4, no. 1, pp. 509–534, 2021.

[19] L. E. Beaver, S. Das, and A. Malikopoulos, "A first-order approach to model simultaneous control of multiple microrobots," 2021, https://arxiv.org/abs/2111.03232.

[20] L. S. Novelino, Q. Ze, S. Wu, G. H. Paulino, and R. Zhao, "Untethered control of functional origami microrobots with distributed actuation," *Proceedings of the National Academy of Sciences*, vol. 117, no. 39, pp. 24096–24101, 2020.

[21] A. Flayyih Hussein, B. Ibraheem Jameel, and K. Karam Abd, "Comparative analysis of Fuzzy MCDM methods for material selection in biomedical application," *Association of Arab Universities Journal of Engineering Sciences*, vol. 25, no. 2, pp. 137–148, 2018.

[22] O. Ehrenberg and G. Kósa, "Analysis of a novel piezoelectric micro-pump for drug delivery in a medical integrated micro system," in *Proceedings of the 2012 4th IEEE RAS & EMBS International Conference on Biomedical Robotics and Biomechatronics (BioRob)*, pp. 467–472, Rome, Italy, June 2012.

[23] S. Tasoglu, C. H. Yu, H. I. Gungordu, S. Guven, T. Vural, and U. Demirci, "Guided and magnetic self-assembly of tunable magnetoceptive gels," *Nature Communications*, vol. 5, p. 4702, 2014.

[24] J. Giltinan, E. Diller, C. Mayda, and M. Sitti, "Three-dimensional robotic manipulation and transport of micro-scale objects by a magnetically driven capillary micro-gripper," in *Proceedings of the 2014 IEEE International Conference on Robotics and Automation (ICRA)*, pp. 2077–2082, IEEE, Hong Kong, China, May 2014.

[25] T. Xu, J. Yu, X. Yan, H. Choi, and L. Zhang, "Magnetic actuation based motion control for microrobots: an overview," *Micromachines*, vol. 6, no. 9, pp. 1346–1364, 2015.

[26] W. Hu, K. S. Ishii, Q. Fan, and A. T. Ohta, "Hydrogel microrobots actuated by optically generated vapour bubbles," *Lab on a Chip*, vol. 12, no. 19, p. 3821, 2012.

[27] T. C. Chu and Y. C. Lin, "A fuzzy TOPSIS method for robot selection," *International Journal of Advanced Manufacturing Technology*, vol. 21, no. 4, pp. 284–290, 2003/02/01 2003.

[28] V. Chodha, R. Dubey, R. Kumar, S. Singh, and S. Kaur, "Selection of industrial arc welding robot with TOPSIS and Entropy MCDM techniques," *Materials Today Proceedings*, vol. 50, pp. 709–715, 2022.

[29] M. Simion, L. Socaciu, O. Giurgiu, and S. M. Petrişor, "The selection of industrial robots for military industry using AHP method: a case study," *Acta Technica Napocensis Series: Applied Mathematics, Mechanics, and Engineering*, vol. 61, no. 2, 2018.

[30] A. M. Ghaleb, H. Kaid, A. Alsamhan, S. H. Mian, and L. Hidri, "Assessment and comparison of various MCDM approaches in the selection of manufacturing process," *Advances in Materials Science and Engineering*, vol. 2020, no. 1, 16 pages, Article ID 4039253, 2020.

Hindawi
Mathematical Problems in Engineering
Volume 2022, Article ID 1633183, 19 pages
https://doi.org/10.1155/2022/1633183

Research Article

Numerical Simulation, Analysis, and Fabrication of MEMS-Based Solid Ag and Cu Microneedles for Biomedical Applications

Nimra Tariq,[1] Muhammad Waseem Ashraf,[1] Shahzadi Tayyaba,[2] Agustín L. Herrera-May,[3] and Enrique Delgado-Alvarado[3]

[1]*Department of Physics, Government College University Lahore, Lahore 54000, Pakistan*
[2]*Department of Computer Engineering, The University of Lahore, Lahore 54000, Pakistan*
[3]*Micro and Nanotechnology Research Center, Universidad Veracruzana, Boca del Rio 94294, Mexico*

Correspondence should be addressed to Muhammad Waseem Ashraf; dr.waseem@gcu.edu.pk and Shahzadi Tayyaba; shahzadi.tayyaba@dce.uol.edu.pk

Received 4 April 2022; Accepted 25 April 2022; Published 25 May 2022

Academic Editor: Mohammad Yaghoub Abdollahzadeh Jamalabadi

Microelectromechanical system (MEMS)-based devices have gained attention recently due to their beneficial biomedical applications. MEMS-based devices like microneedles have set new trends in drug delivery, vaccination, skin, and eye treatment. Different materials like metals, sugars, polymers, and silicon have been used for fabrication. Various techniques have been used for their fabrication, including laser ablation, lithography, injection molding, and additive manufacturing. The tip diameter of different micron ranges has been achieved. The strength and stiffness of the microneedle's tip have always been important in fabricating microneedles so that it does not break on insertion. This research paper presents a comparison between silver (Ag) and copper (Cu) solid microneedles by performing numerical analysis using the fuzzy approach, structural simulation, and fabrication. Firstly, structural simulation has been performed in ANSYS software to test the strength of silver (Ag) and copper (Cu) microneedles separately. The purpose is to compare the stress effect and fracture limit of both microneedles. The results collected from the simulation provide valuable target and prediction facts to fabricate improved designs of the solid Ag and Cu microneedles. Then, fuzzy-based numerical analysis has been performed in MATLAB software for both microneedles separately. In this numerical analysis, the effect on the range of microneedle tip diameter and cone length has been observed by varying input voltage and time. Finally, fabrication has been performed using a novel economical technique such as electrochemical etching. Electrochemical etching is a very low-cost and clean room-free technique as compared to other techniques used for the fabrication of microneedles. The fabrication technique adopted in this work is the same for both silver and copper microneedles. The scanning electron microscopy (SEM) characterization has been performed for both fabricated microneedle tips. The tip of the fabricated solid Ag and Cu microneedle has been then coated with drugs using the dip-coating method. The coated solid Ag and Cu microneedle's tip has been then characterized again using SEM. The numerical results calculated from the fuzzy analysis have been then compared with fabrication results. The fuzzy analysis gives the simulated size of the microneedle's tip for 5.05 μm silver and 5.12 μm copper which have very close approximation with the experimental values from the SEM micrographs which also give the values of the cone length from 400 to 500 μm and the tip size from 5 to 6 μm for the time of 10–15 minutes, whose values were optimized by the fuzzy analysis. The results of this research provide valuable benchmark and prediction data to fabricate improved designs of the silver solid microneedles for drug delivery and other biomedical applications.

1. Introduction

Microelectromechanical system (MEMS)- based technology has been increasing swiftly in biomedical devices. MEMSs are micron range devices that are the root of many integrated and smart devices. Due to microelectromechanical systems-based technology, the fabrication of miniature-size devices has been increased. The increasing performance of medicinal devices has become achievable to meet the critical medicinal requirements. These requirements include controlled drug delivery with insignificant side effects, enhanced bioavailability, and healing effects. In biomedicine, MEMS-based devices integrated with microneedles, microvalves, micropumps, and microchannels have many important biomedical applications. Scientists are working on their development and improvement for many years and set new trends. MEMS-based microneedles range from a few micrometers to millimeters. These microneedles are different from hypodermic microneedles because they are in the micrometer to millimeter range and make drug delivery easier and painless [1]. The objective of MEMS-based microneedles includes painless and safe insertion of needles into the skin and skin retrieval after the removal of the microneedle. They are also used in drug constancy throughout manufacturing, delivery, and storage. For patients, they help result in less pain, irritation, and infection in the skin, in addition to drug effectiveness and safety [2]. By developing a base with strong technology and multiple demos of effective drug delivery, microneedles are composed to progress more into clinical practice. This allows better medical therapies, vaccinations, and other numerous applications [3]. Microneedles have been categorized into four different types: solid microneedles, hollow microneedles, coated microneedles, and dissolving microneedles. Each microneedle type has its unique trend and innovation [4, 5]. Solid microneedles are commonly used for skin pretreatment to upsurge skin porousness. Coated microneedles which are drug-coated dissolve easily into the skin. Dissolving microneedles include polymers-made microneedles that comprise a drug and completely dissolve into the skin. Hollow microneedles are used to infuse the drug into the skin deeply [6–8]. Solid microneedles are nowadays of more interest because of their use in skin treatment as well as drug delivery. They are sharp enough and pierce into the skin or scrape the skin to make holes. Drugs can pass through these holes for either limited effect of the drug in the skin or universal delivery after acceptance by skin tubes [9–11]. A drug-loaded patch is used to apply to the skin surface above the pores for straight transdermal drug delivery. A semisolid contemporary formulation can also be used, such as a cream, ointment, gel, or lotion, because it is mostly used in skin treatments [12, 13]. The solid microneedles fabricated using different techniques have been concentrated on providing an appropriate mechanical strength. This is achieved by considering the sufficient materials for microneedles and geometry and by increasing tip sharpness to reduce the force required for inserting microneedles into the skin [14–16]. Some of the most common techniques used for the fabrication of microneedles are laser ablation, additive manufacturing, injection molding, and lithography as shown in Table 1.

Different materials used nowadays for the fabrication of microneedles are silicon, nondegradable polymers such as photolithographic epoxy a methyl vinyl ether copolymer, polycarbonate, maleic anhydride, and polymethyl-methacrylate (PMMA), polyglycolic acid (PGA), and polylactic acid (PLA). Water-soluble compounds comprised of maltose, metals containing stainless steel, titanium, nickel, and tantalum are also used [25, 26]. Microneedles have been experienced on human skin, and the other drug delivery MEMS devices have shown potential in vivo and in vitro [27]. Garcia et al. [28] reported self-sterilizing dissolving microneedles patches loaded with nanosilver and fabricated from carboxymethylcellulose which is proficient in surpassing the growth of microbial pathogen at the insertion place. Chang et al. [29] reviewed the modern developments of solid microneedles by concentrating on the materials and techniques used for the fabrication of solid microneedles. Driven by the exceptional structures and efficient materials, these microneedle patches can deliver unique solutions for skin diseases, diabetes, overweightness, and ocular diseases, as well as quick diagnosis. Liu et al. [30] presented the innovative biomedical applications of microneedles made of polymers for therapeutic delivery or transdermal drug delivery and diagnosis. The present limitations, as well as future perceptions of solid microneedles made from polymer materials, were also provided. Moussi et al. [31] presented the new biocompatible 3D-printing technique for developing solid microneedles required for undetectable tissue dispersion and transdermal and intradermal drug delivery. Lee et al. [32] discussed the design and formation of current microneedles that were designed with intention of surpassing the biological barricades of nontransdermal drug delivery in oral, optical, vascular, and mucosal tissues. Bonfante et al. [33] described that there are different polymers materials used for the fabrication of microneedles. So, to understand which polymer material is more appropriate depending upon its mechanical properties, they presented a comparison of polymers. It was to improve the mechanical properties of fabricated microneedles for different biomedical applications. Chi et al. [34] developed a biomass-based chitosan-microneedle-array patch combined with smart receptive drug delivery for endorsing wound curing. Cai et al. [35] summarized the innovative technologies working for the integration of microneedles arrays or patches with definite living organisms together with miscellaneous viruses, mammal cells, bacteria, and so on. Dugam et al. [36] reviewed different fabrication materials and techniques to emphasize distinct advantages of microneedles in biomedical industries. The development and design of MEMS-based microneedles are powerfully dependent on the fabrication method. Many of the present microfabrication technologies have resulted from procedures settled to fabricate ICs. One of the most common and significant fabrication technologies is photolithography [37]. Others include soft lithography, chemical vapor deposition, and stereolithography. All of these techniques are quite expensive and require a complete setup of sufficient environment for performing experimentation [1]. Similarly, different materials are used in the fabrication of microneedles, and the most common are silicon and polymers. Silicon is mostly used as a substrate in the fabrication of microneedles patches. This is because silicon has some outstanding mechanical as well as electrical properties and it also provides a great possibility to integrate the circuits on the transducer's substrate. For stand-alone microneedles silicon, metal, and polymer materials are greatly used in the fabrication of these stand-alone microneedles. Each of these

Table 1: Microneedles fabrication techniques.

Fabrication techniques	Overview	Cost analysis/disadvantages	References
Lithography	The master pattern of the geometric shapes transfers to the substrate surface	High cost not suitable for mass production	[16, 17]
Additive manufacturing/surface micromachining	Layer-by-layer microneedles printing	Cost-effective but not too	[16, 18, 19]
Injection molding	Inject plastic materials into a mold	High initial cost (machine equipment is costly). Composite processes	[1, 20, 21]
Laser ablation	Use laser beam for making the substrate on which microneedles are fabricated	High cost not appropriate for large manufacturers	[22–24]

materials has its strength and efficiency [38]. Silver material has been used as a coating material for microneedles. They are fabricated from other materials and loaded as nanosilver in dissolving microneedles. Silver material is a renowned antimicrobic agent in contrast to an extensive range of microbes, over 650 microbes from diverse classes, that is, Gram-positive and Gram-negative bacteria and viruses. Owing to the ratio among positive and negative side effects, silver has advantages over numerous other antimicrobic agents and particularly antibiotics [21, 39]. Silver has an interesting history of using antibiotics in human well-being. It has been industrialized for usage in water sanitization, wound cleaning, bone prosthetic device, rehabilitative orthopaedical surgical procedure, cardiac care, and surgical applications. Progressing biotechnology has allowed integration into fabrics of ionizable silver for clinical uses to cut the risk of infections as well as for individual hygiene [40]. The antimicrobic action of silver/silver compounds is relational to the bioactive silver ion and its accessibility to interrelate with microbial or fungous cell membranes [25, 41]. Silver metal or inert silver compounds ionize in water, other specimen fluids, or tissue exudations. The silver ions are organically active and voluntarily interrelate with proteins, amino-acid remains, free anions, and receptors on mammals and eukaryotic cell membranes. The bactericidal action of silver is well known. It helps in reducing or avoiding contamination. It can be seen in numerous applications such as treatment for injuries and wounds that are chronic and as a coating layer for both momentary and permanent medicinal devices. Silver has been extensively used as a nanoparticle in many types of research. Silver nanoparticles have many potential applications that are highly influenced by a few factors such as shape and size [42, 43]. Many types of research have been done on silver nanoparticles and nanowires due to their tremendous applications [44]. Silver material has not been used for microneedles fabrication; however, coating with silver has been done on microneedles. It is fabricated from other materials and loaded as nanosilver in dissolving microneedles. Silver material is a renowned antimicrobic agent in contrast to an extensive range of microbes, over 650 microbes from diverse classes, such as Gram-positive and Gram-negative bacteria and viruses. Owing to the ratio among positive and negative side effects, silver has advantages over numerous other antimicrobic agents, particularly antibiotics. Silver has an interesting history of using antibiotics in human well-being. It has been industrialized for usage in water sanitization, wound cleaning, bone prosthetic device, rehabilitative orthopaedical surgical procedure, cardiac care, and surgical applications [45, 46]. Progressing biotechnology has allowed integration into fabrics of ionizable silver for clinical uses to cut the risk of infections as well as for individual hygiene. The antimicrobic action of silver/silver compounds is relational to the bioactive silver ion and its accessibility to interrelate with microbial or fungous cell membranes. Silver metal or inert silver compounds ionize in water, other specimen fluids, or tissue exudations [47, 48]. The silver ions are organically active and voluntarily interrelate with proteins, amino-acid remains, free anions, and receptors on mammals and eucaryotic cell membranes. The bactericidal action of silver is well known. It helps in reducing or avoiding contamination. It can be seen in numerous applications such that treatment for injuries and wounds that are chronic and as a coating layer for both momentary and permanent medicinal devices. Silver has been extensively used as a nanoparticle in many types of research [49, 50]. Silver nanoparticles have many potential applications that are highly influenced by a few factors such as shape and size. Many types of research have been done on silver nanoparticles and nanowires due to their tremendous applications [51]. Silver material has not been used for microneedles fabrication; however, coating with silver has been done on microneedles. On the other hand, copper-based hollow microneedles have been fabricated so far using electrodeposition-based additive manufacturing techniques. Copper has been used for plating different metal microneedles. Copper nanoparticles have been fabricated for many years using the natural process of chemical synthesis [52–54]. Copper acts as an antibiotic, antifungal, and antimicrobial agent when added to coatings. Copper has many biological applications which make researchers use copper in developing copper-based biomaterials. These biomaterials exhibit exceptional properties in protecting the cardiac system, helping bone fracture healing, and employing antibacterial effects [55–60]. In this research, we have fabricated solid silver and copper microneedles by using an economical technique of electrochemical etching. But, before fabrication, simulation of MEMS-based microneedles has been performed. Simulation is the best way to optimize the model and process parameters before fabrication. Many simulation tools are used nowadays including COMSOL, ANSYS, and Matlab. It has been identified that, by using fuzzy tools and intelligent systems, better results were achieved. These fuzzy systems have valued logic between integers of 0 and 1. Many researchers have used fuzzy logic for monitoring and optimizing their fabricated products and done marvelous work in their research areas [61–66]. Here in our research multiple simulations using fuzzy numerical analysis have been conducted to optimize the effect of input parameters of time, voltage, and elastic modulus on the output of tip diameter and cone length. For structural simulation and fluidic analysis, ANSYS software has been used. Zhang et al. [67] performed finite element analysis of out-of-plane microneedles using ANSYS for transdermal drug delivery. Ashraf et al. [68] conducted simulation by using ANSYS before fabrication to optimize the suitability of design for transdermal drug delivery. Kuo et al. [69] conducted a numerical simulation to confirm the design of PLA microneedle using the optimal process parameters. In our research, ANSYS has been used to check solid silver and copper microneedles' tip strength and how much force or stress they will bear when inserted into the skin. After that fabrication has been performed using the electrochemical etching technique. The fabricated microneedle tip has been then sent for characterization using a scanning electron microscope (SEM). The fabricated microneedles tip has been then coated with drugs. The coated tips have also been characterized using SEM (scanning electron microscope). The surface of solid microneedle's tip before and after the coating has also been observed in SEM characterization to quantify the amount of drug coating onto the microneedle tip depending on its surface tension, capillary forces, and viscous forces.

2. Structural Simulation

MEMS-based microneedles are usually patterned as an array on the patch which is just like the nicotine patch or hydrogel patch used in baby diapers. But here, for a better understanding of the structure and working of the MEMS-based microneedle, we just assume a single microneedle made of silver and copper materials. ANSYS workbench has been used for simulation on which step-by-step simulation is carried out. The simulation for both silver and copper microneedles has been performed separately. First, the 3D model of microneedle has been designed. Afterward, the force has been applied on the designed microneedle to estimate how much force or stress it can bear when applied to the human body. In this structural examination, a microneedle with 500 μm length, 200 μm width, and approximately 5–7 μm tip diameter has been designed in the design modeler of ANSYS workbench. The 3D and meshed model of the designed microneedle is shown in Figure 1. Afterward, the designed 3D structure has been meshed using a mesh tool available in the ANSYS workbench because ANSYS is a finite element analysis (FEA) software and by meshing the structure we can do an element-by-element analysis of 3D structure. After designing the 3D model and analyzing the mesh model for silver and copper microneedle. The different parameters of mechanical properties such as Young's modulus, elastic modulus, Poisson's ratio, ultimate tensile strength, compressive tensile strength, and density for silver and copper material have been assigned to estimate the endurance and strength of our final fabricated model. The boundary conditions of stress and fixed support are applied to analyze the effect of stress from tip to base when inserted on the human skin. The stress effect on designed 3D solid model for microneedle is shown in Figure 2. When the stress of 800 MPa is applied, it goes from top to bottom. It is because first the tip is being applied to the skin for drug delivery.

Then, simulation results of total deformation, directional deformation, von Mises stress, equivalent elastic strain, and structural error for solid copper and silver microneedle are shown in Figures 3–7.

The tip comparison has also been done to check how much deflection occurs when stress is applied. The change in deflection and deformation of both microneedles depends on their elastic modulus and how much elasticity or stiffness they have to overcome the stress. Thus, comparison of tip's deflection is shown in Figure 8.

The results presented above have been taken by performing simulation in ANSYS workbench which is FEA software. Simulation is useful as it reduces the resources instead of direct fabrication.

3. Fuzzy Analysis

Fuzzy numerical analysis has been used to define the parameter of the systems in a definite way. The uncertainties and inaccuracies of physical systems can be easily quantified by using fuzzy numerical logic analysis. Appropriate notation, fractional truth concept, Boolean truth, and Boolean logic have been used in fuzzy numerical analysis to describe the accuracies of physical systems [70, 71]. Fuzzy numerical logic has its impact on every area of life and its application such as material sciences, MEMS-based devices [72], fluid dynamics, agricultural problems, information expertise, and automobiles and even in the advancement of control systems. In this research paper, numerical analysis performed by using fuzzy logic controller is presented. Fuzzy conditions are considered to be as accurate as the ideal conditions. They are more dependable as they can give infinite values in between zero and one.

It has been found in the literature that fuzzy logic has been used in many different appliances like blood pressure, washing machine, and other smart devices [73, 74]. Therefore, for understanding the effect of time, voltage, and elastic modulus on the tip diameter and needle length, we have also used fuzzy logic for analysis and consideration. The input parameters are time, voltage, and elastic modulus, whereas the output parameters are tip diameter and cone length. The microneedle FLC interface for both microneedles is given in Figure 9. Here, in both FLC models, three inputs have been considered and outputs have been achieved by varying the input conditions.

A fuzzy numerical-based logic controller has some important properties which include being easy to handle, flexibility of functional values, ease to understand, and easy modeling development, and, despite all this, it gives a

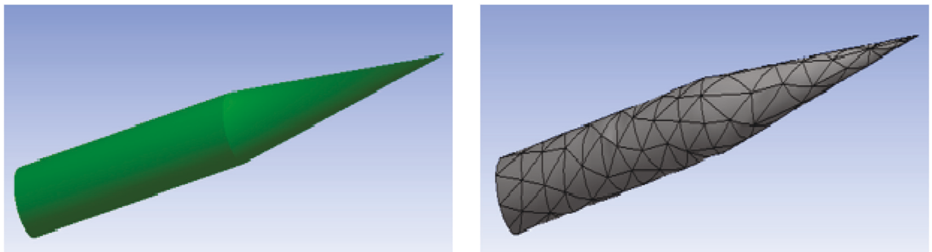

(a) (b)

Figure 1: Project design overview. (a) 3D model of solid microneedle. (b) Mesh view of the solid microneedle.

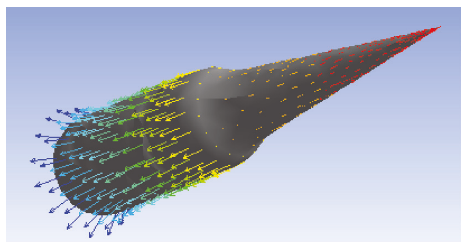

Figure 2: Stress effect overview on the 3D model of solid microneedle.

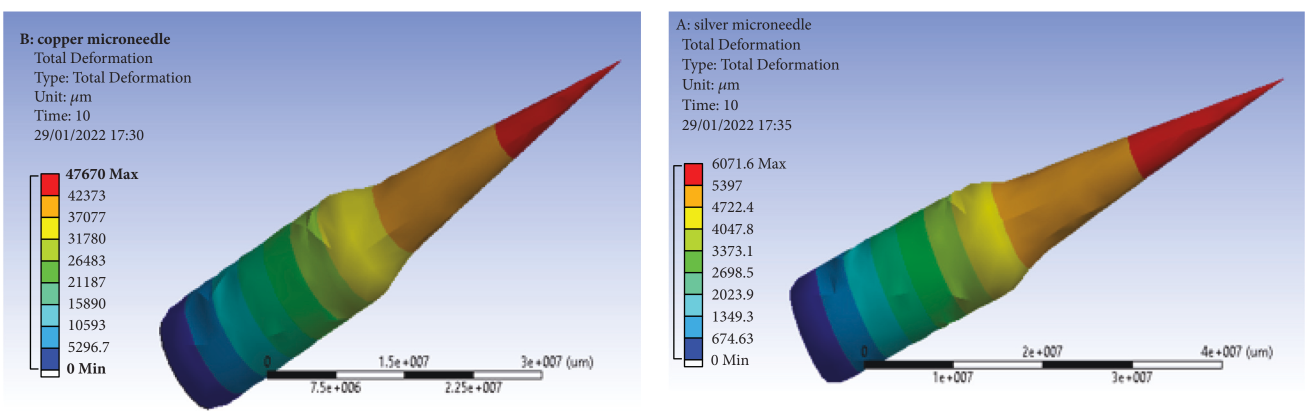

(a) (b)

Figure 3: Comparison between simulated results of total deformation for (a) copper microneedle and (b) silver microneedle.

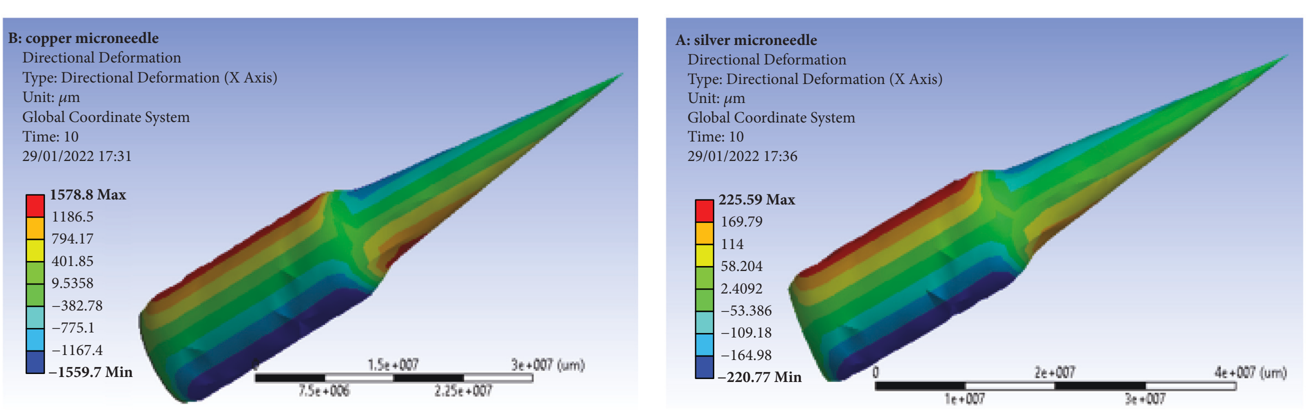

(a) (b)

Figure 4: Comparison between simulated results of directional deformation for (a) copper microneedle and (b) silver microneedle.

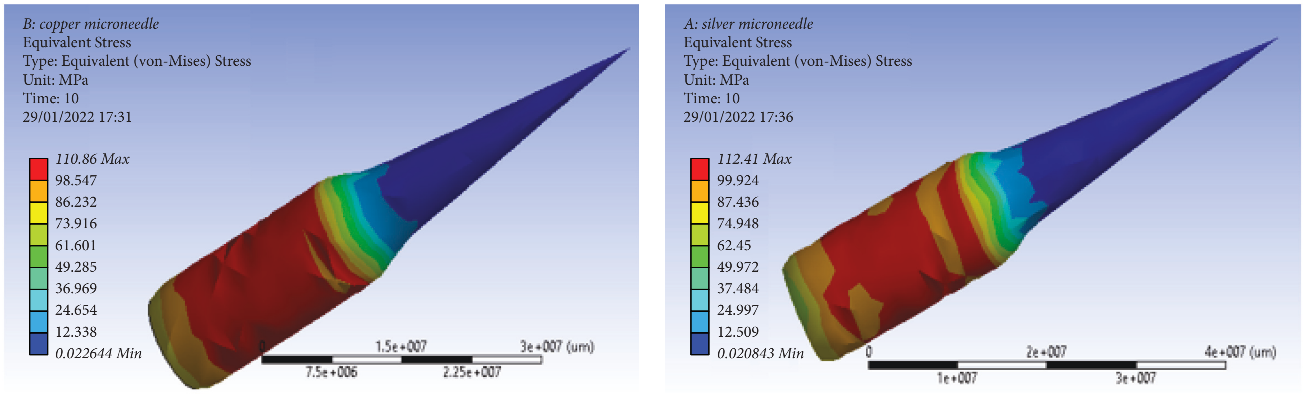

(a) (b)

Figure 5: Comparison between simulated results of Von Mises stress for (a) copper microneedle and (b) silver microneedle.

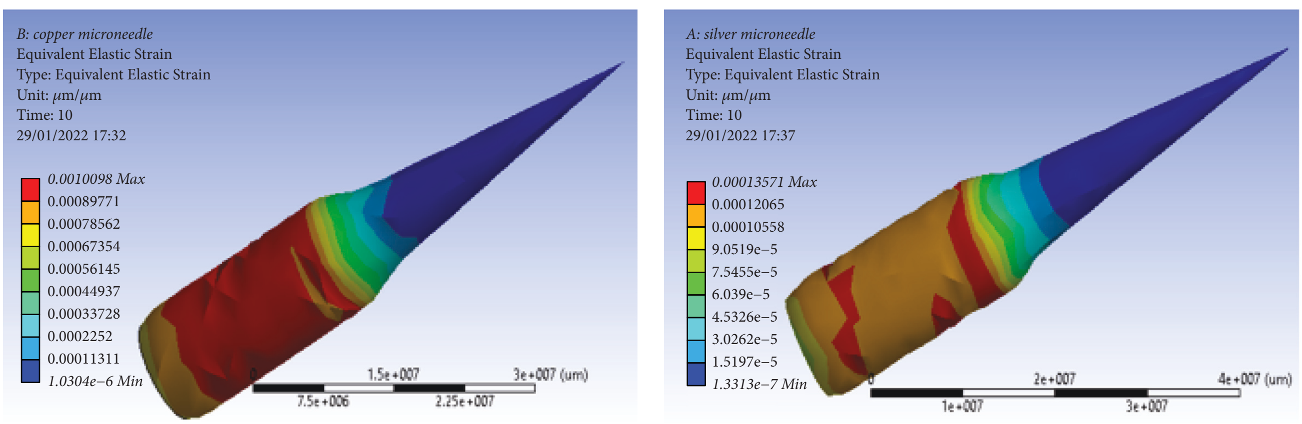

(a) (b)

Figure 6: Comparison between simulated results of equivalent elastic strain for (a) copper microneedle and (b) silver microneedle.

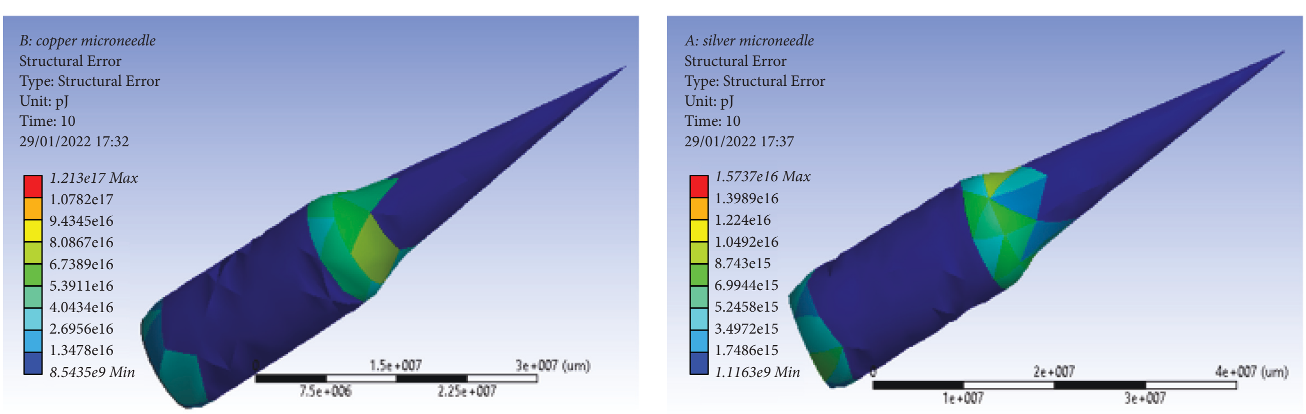

(a) (b)

Figure 7: Comparison between simulated results of structural error for (a) copper microneedle and (b) silver microneedle.

solution to the problem in big data systems due to Boolean manipulation [75]. In this research, simulations have been performed using fuzzy numerical analysis to optimize the process parameters. On the basis of these numerically optimized parameters, fabrication has been done to cut off extra expenses and get better designed fabricated model. The input and output parameters are designated by keeping all other parameters of the system constant. After deciding the

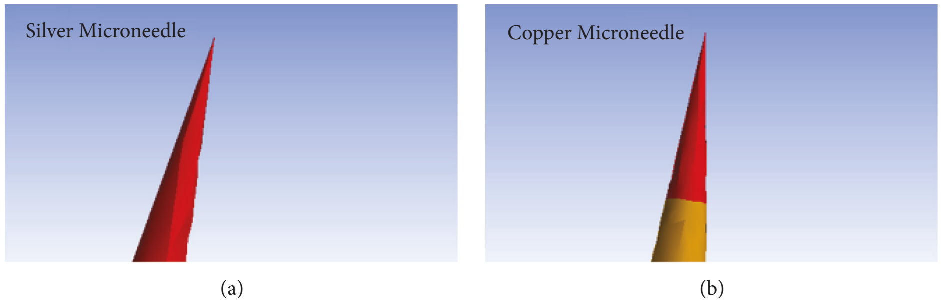

Figure 8: Comparison of tip's deflection when stress is applied. (a) Silver microneedle and (b) copper microneedle.

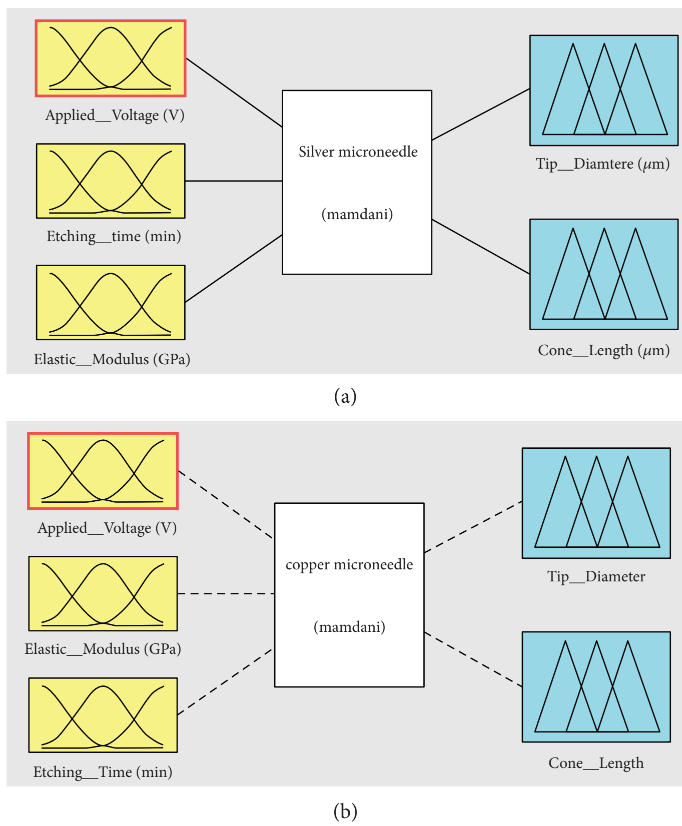

Figure 9: The microneedle FLC interface. (a) Silver microneedle. (b) Copper microneedle.

inputs and outputs, the membership functions for both parameters have been made by selecting the different ranges of values. The ranges of values chosen for membership functions are given in Table 2.

After that, the Mamdani model [76] has been used for the fuzzification of the MEMS-based microneedle by defining the all possible rules. The membership function plots for both microneedles are drawn and they are the same as inputs and outputs are the same for both. The inputs and outputs membership function plots are given in Figures 10–14.

In Figures 13 and 14, it is shown that the membership function values for outputs of tip diameter and cone length are small; possibly the best output deliberation is indicated by the red line in the membership function plots. After the fuzzification, the surface viewer has been drawn for both microneedles to explain in detail the comparative effect of input parameters values like voltage, time, and elastic modulus on the ranges of tip diameter and cone length for both silver and copper microneedles as shown in Figures 15–18.

Table 2: All inputs and outputs values.

Sr. no.	Inputs	Selected range
1	Applied voltage	0–30 V
2	Etching time	0–60 min
3	Elastic modulus	0–300 GPa
	Outputs	
1	Tip diameter	0–10 μm
2	Cone length	0–500 μm

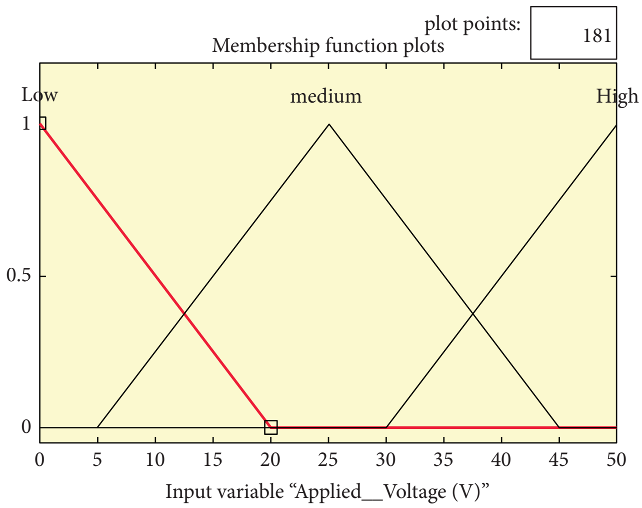

Figure 10: Membership function plot for applied voltage.

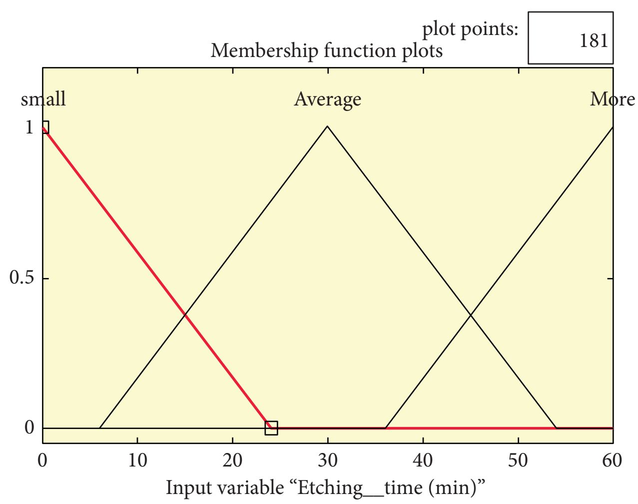

Figure 11: Membership function for etching time.

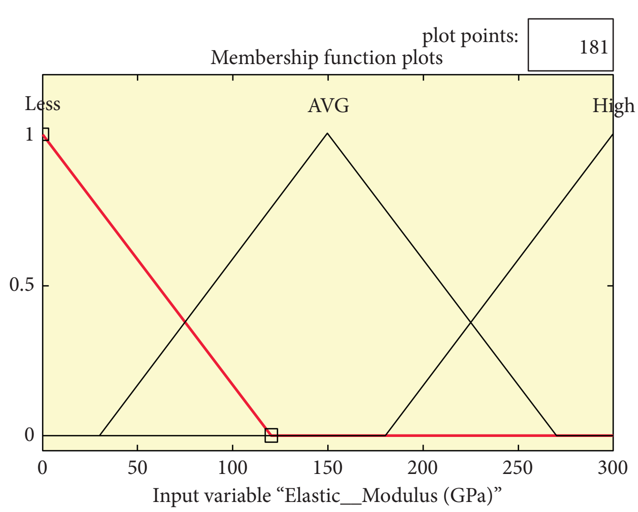

Figure 12: Membership function for elastic modulus.

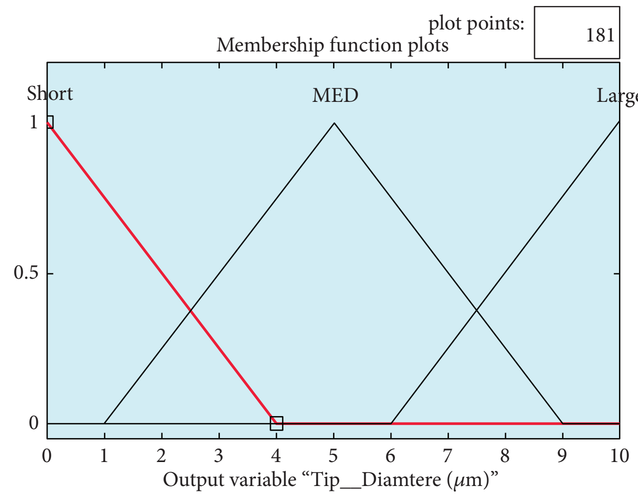

Figure 13: Membership function for tip diameter.

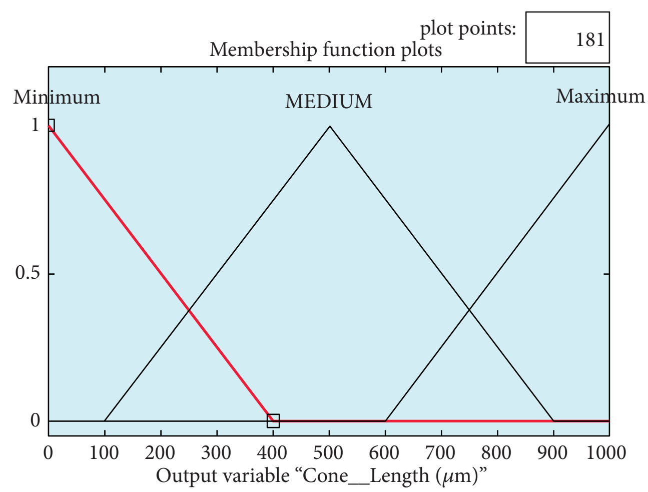

Figure 14: Membership function for cone length.

Figures 15–18 show the effect on tip diameter and cone length of fabricated Ag and Cu microneedles by varying applied voltage, elastic modulus, and etching time. It has been found that the tip diameter keeps decreasing around 5–6 μm when current and applied voltages increase. The cone length is maximum on the applied input parameters. The comparison of rule viewer for both microneedles calculated by FLC simulation on setting value range for both input and output parameters is given in Figure 19.

After the comparative numerical analysis of silver and copper microneedles using FLC, it has been found that using the same input parameters of applied voltage and etching time for both microneedles gives us tip diameters of around 5.05 μm for silver and 5.12 μm for copper with cone length of approximately 500 μm for both. These values for both tip diameters are obtained by varying input parameters of applied voltage and etching time with respect to fixed elastic modulus of both microneedles. It has also been observed in numerical analysis that, for copper microneedle, etching

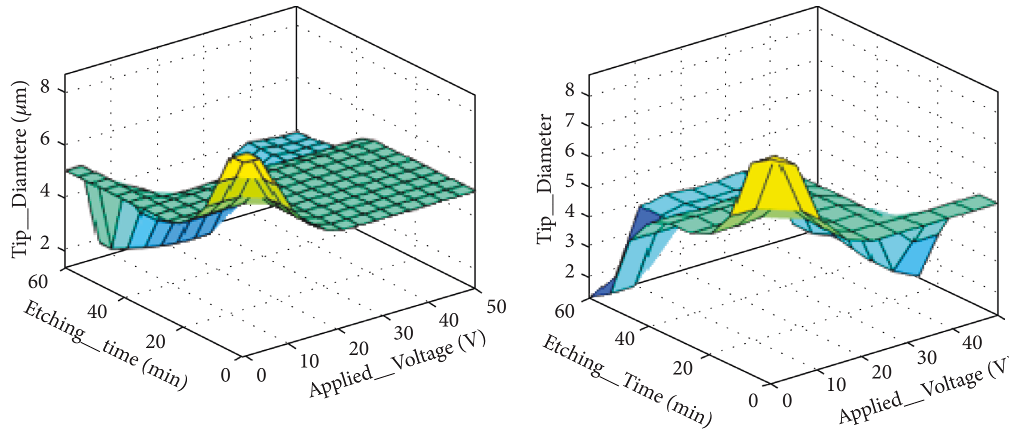

(a) (b)

Figure 15: Comparison of the surface viewer of tip diameter with respect to etching time and applied voltage for (a) silver microneedle and (b) copper microneedle.

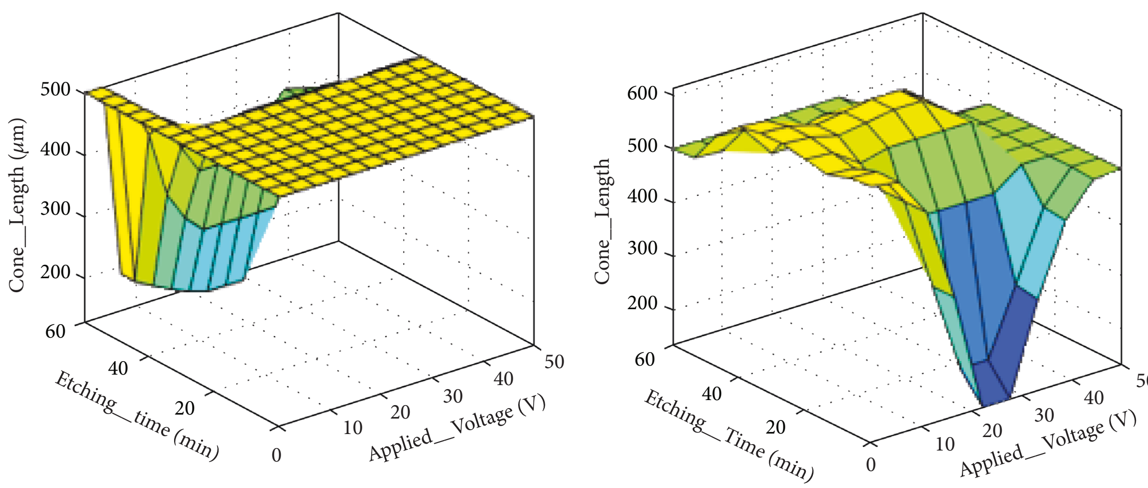

(a) (b)

Figure 16: Comparison of the surface viewer of cone length with respect to etching time and applied voltage for (a) silver microneedle and (b) copper microneedle.

time and voltage need to be increased more as compared to silver microneedle etching. Also, it has been observed by surface viewer and rule viewer that, by increasing the applied voltage and etching time, the tip diameter decreases. The slight difference between the tip diameters of silver and copper microneedles is due to the elasticity of the materials. Copper is considered to have comparatively more elastic modulus and more stiffness than silver.

As the fuzzification of any device is based on the Mamdani model, here, for MEMS-based microneedle, the Mamdani model has also been considered. Some mathematical calculations have been done to understand the comparison between simulated and Mamdani values for both microneedles separately to calculate the accuracy or error percentage of our FLC simulation results. For the error percentage confirmation, Mamdani's formula has been used for the mathematical/numerical calculations. It has been found that a tip diameter of 5.13 for copper microneedle and a tip diameter of 5.06 for silver microneedle are obtained, whereas, from Mamdani mathematical calculations, the cone length for both microneedles was found to be about 498 μm. The difference between the fuzzy simulated values and the Mamdani mathematical values for microneedles' tip and cone length gives just 0.01% and 0.02% errors.

4. Fabrication Analysis

4.1. Materials and Methods for Silver Solid Microneedle. For silver solid microneedle, the etchant has been prepared by mixing the 3M solution of HCL and FeH18N3O18 into DI water. For this purpose, 30 g high graded ferric nitrate non-ahydrate (FeH18N3O18) has been mixed into the 250 ml DI

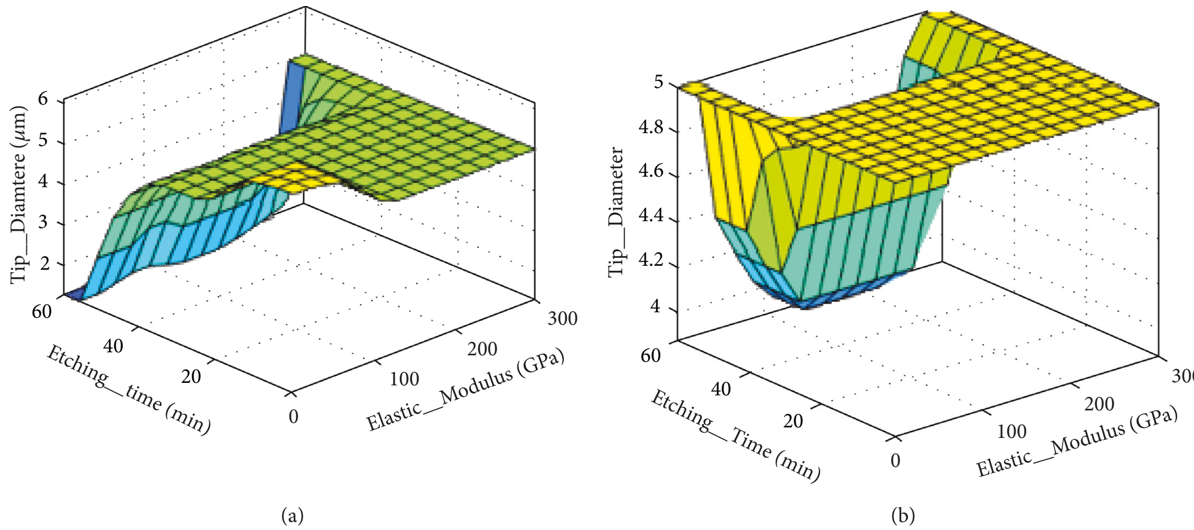

Figure 17: Comparison of the surface viewer of tip diameter with respect to etching time and elastic modulus for (a) silver microneedle and (b) copper microneedle.

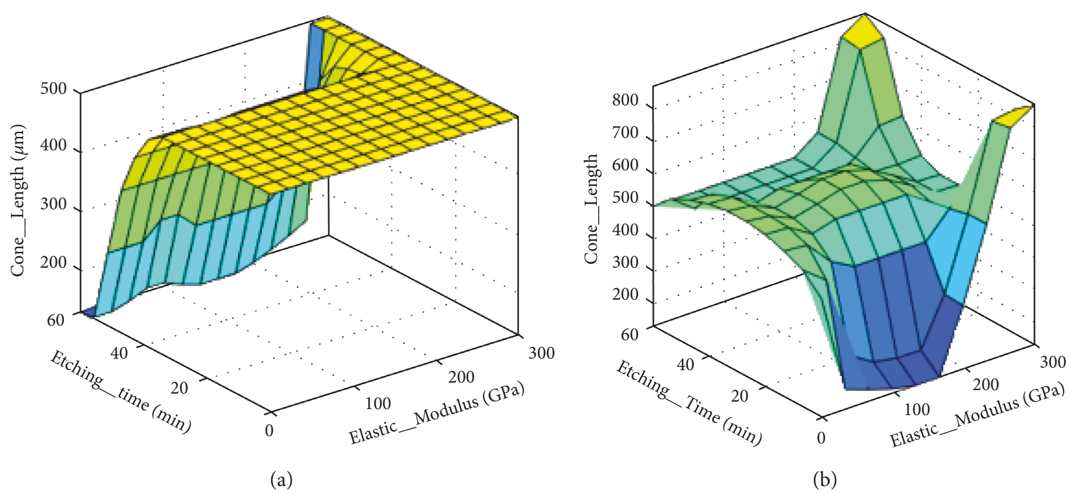

Figure 18: Comparison of the surface viewer of cone length with respect to etching time and applied voltage for (a) silver microneedle and (b) copper microneedle.

water and then magnetically stirred for 30 minutes. After stirring, 10 ml of HCl has been mixed dropwise into the former prepared solution which turned intense yellow immediately.

4.2. Materials and Methods for Copper Solid Microneedle. For copper solid microneedle, the etchant has been prepared by mixing the 3M solution of NaCl and HCL into DI water. For this purpose, 30 g high graded NaCl (Sigma-Aldrich 99%) has been mixed into the 250 ml deionized water (DI, Q-murk deionizer) and magnetically stirred for 20 minutes. After stirring, 10 ml of HCl has been mixed into the formerly prepared solution dropwise which maintained a light blue color.

4.3. Experimental Setup. For the fabrication of silver and copper solid microneedle, the self-designed setup has been used. The self-designed setup works on the principle of electrolysis and is named electrochemical etching. The experimental setup used for fabrication consists of the glass beaker which is round neck from the top (Pyrox, 500 ml) with a glass lid having a hole to let the graphite cathode and a catcher pass through it.

A catcher has been used for holding the silver and copper wire and it acts as an anode. Both wires attached to the catcher have been immersed into the etchant vertically with the help of the conducting catcher. DC power supply has been attached across the electrodes with the help of the probes. The voltage, time, and current have been controlled physically by the knob (used for tunning) attached to the power supply as shown in Figure 5. A pure silver (925 sterling) wire of 0.5 mm has been purchased and then cut into small pieces of 1.7–2 cm in length. Similarly, copper wire of fin quality has been purchased and then cut into small pieces of 1.5–2 cm in length.

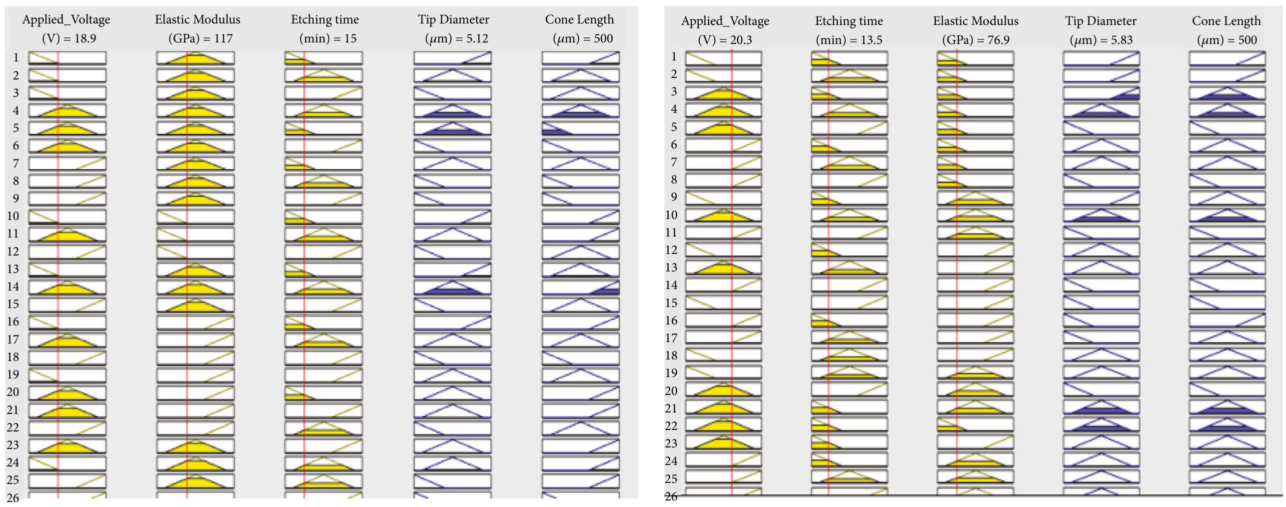

(a) (b)

Figure 19: Rule viewer comparison for (a) silver microneedle and (b) copper microneedle.

4.4. Electrochemical Etching Procedure. After cutting, the silver and copper wires have been properly cleaned by the deionized (DI) water. Then, both cleansed wires have been placed into the ultrasonic bath for 20 mins to remove all impurities. Next silver and copper wires have been placed in the separate Petri dishes having ethanol and left for drying in the laboratory oven under the heat treatment at about 1500°C. After the cleaning process, the prepared etchant solution of electrolyte has been put into the glass beaker of the etching setup. The graphite cathode and cleaned silver wire and copper wire anode are dipped vertically into the separately prepared etchant solution for both microneedles. A DC of 30 mA and voltage of 15–24 V have been applied across electrodes for 10–20 minutes by using a regulated DC power supply for both microneedles. After etching is done, the silver and copper needles have been again washed by using DI water and ethanol. Finally, the fabricated silver and copper microneedles have been sent for characterization. The fabricated silver and copper microneedles have about 6 μm diameter. The schematic for electrochemical etching of silver and copper microneedles is shown in Figure 20.

The etching mechanism is also explained as shown in Figure 21 showing how the etching has been performed when the silver and copper wires were dipped into the prepared etchant solution.

5. Characterization Results

The fabricated silver and copper solid microneedles have been characterized after a thorough analysis by the scanning electron microscope (SEM). The tip of both microneedles has a range of around 5-6 μm. The SEM image has been taken for different micron ranges to observe microneedles closely. The SEM characterization for both solid microneedles has been performed to study the structure of microneedles.

The SEM results for both solid microneedles with cone length of approximately 500 μm are shown in Figure 22.

Also, the zoomed SEM images of both silver and copper microneedles have been taken to observe the etched surface of both microneedles' tips as shown in Figure 23.

6. Coating of Microneedles

After the characterization for silver and copper solid microneedle has been done, the coating of material on microneedles has been done. For coating, the dip-coating method has been used and prototypical molecules of riboflavin (7,8-dimethyl-10-[(2S,3S,4R)-2,3,4,5-tetrahydroxypentyl] benzo[g]pteridine-2,4-dione) has been coated on the microneedle. First, the microneedles have been dipped separately into 3 micrograms of riboflavin and then taken off. The microneedles entrain a liquid film on their tip surface upon exiting the coating liquid. The dissolved solids existing in the liquid film get deposited on the solid silver and copper microneedle surface as a coating after the solvent in the liquid film evaporates.

The contribution of surface tension of coating material is significant in the dip-coating method. The coated silver and copper microneedles have also been sent for characterization to quantify how many drugs coated on their surfaces hold, and comparative images with 2x zoom are shown in Figure 24 and Figure 25 before and after coating.

Also, the surfaces of coated microneedles have been observed for quantifying the amount of drug stuck on it as shown in Figure 25.

7. Results and Discussion

The graphical analysis has been done firstly on the simulation results taken for both silver and copper solid microneedles. The fracture strength of the microneedle's tip has been examined to evaluate the possibility of its fracture during the medical application. Therefore, how much tip deflection takes place on applying stress of around 800 MPa so that its fracture limit is being estimated has been analyzed

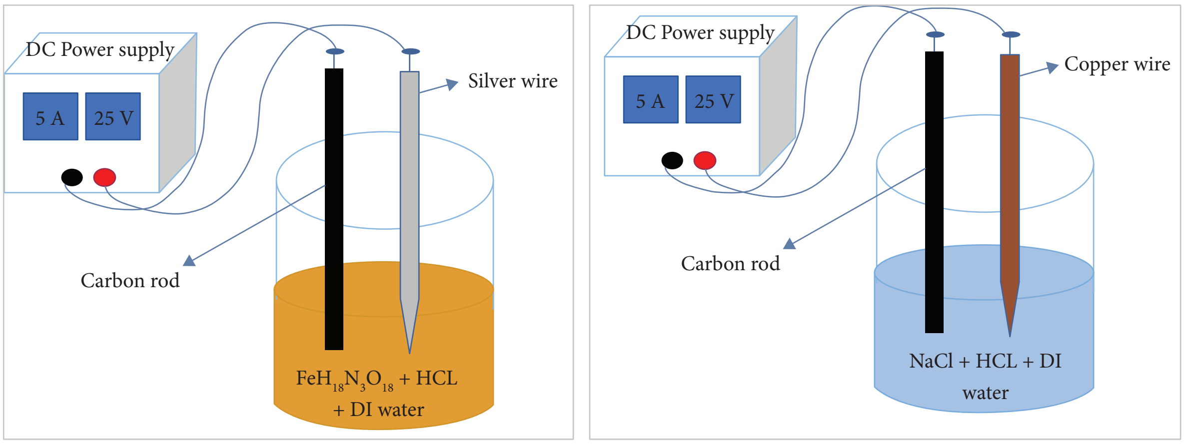

Figure 20: Schematic electrochemical etching setup for silver and copper solid microneedle.

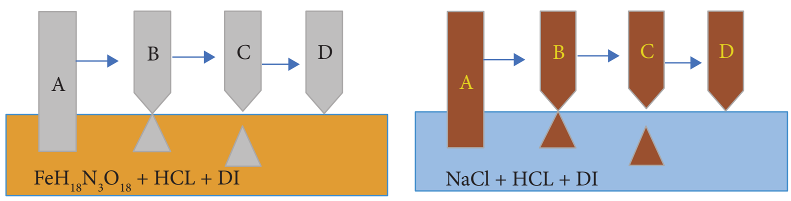

(a) (b)

Figure 21: Etching mechanism for (a) silver and (b) copper solid microneedles.

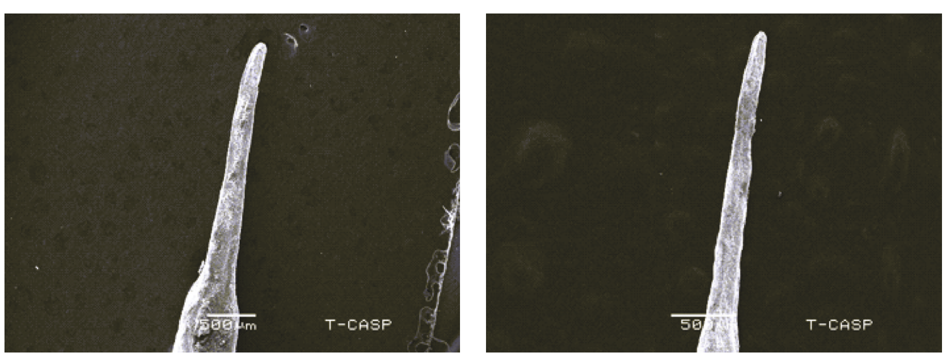

(a) (b)

Figure 22: SEM image of (a) silver and (b) copper microneedle tip for 500 μm.

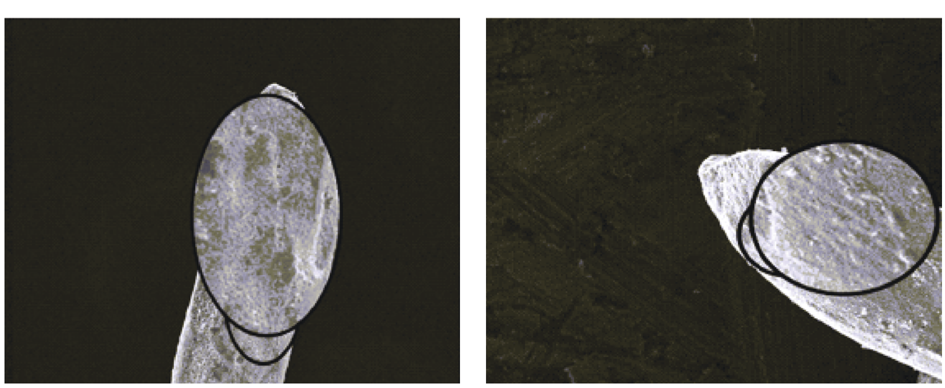

(a) (b)

Figure 23: 2x zoomed SEM images of (a) silver and (b) copper microneedle tips with a magnified etched surface.

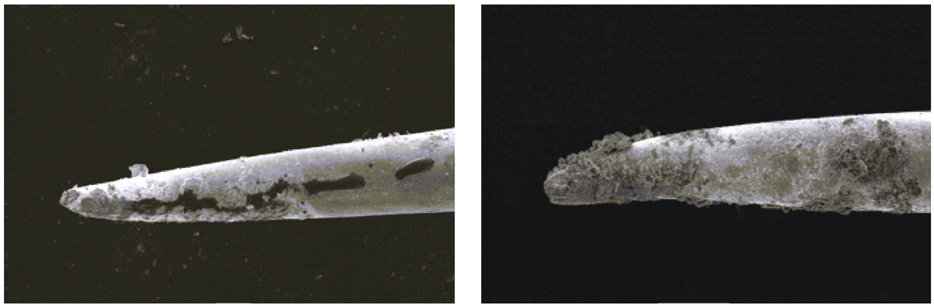

(a) (b)

Figure 24: Magnified SEM images of (a) silver and (b) copper coated microneedle.

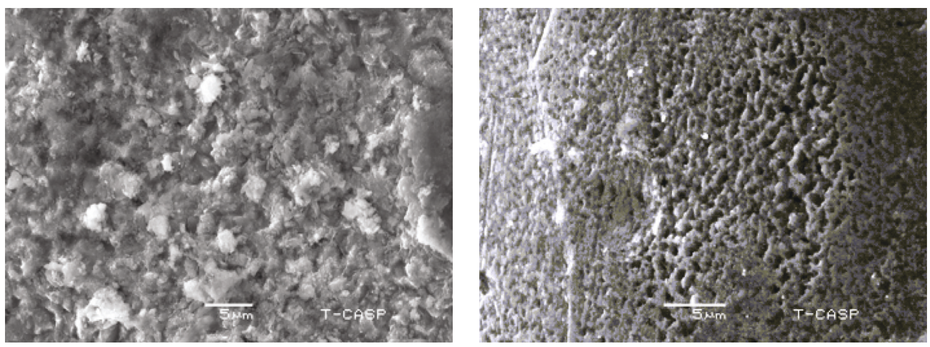

(a) (b)

Figure 25: Magnified SEM images of tip surface (a) silver and (b) copper coated microneedle.

because once the tip starts deflecting rapidly it is more likely to get fractured on the application. The tip deflection based on the stress-tip diameter data obtained from the simulation results are displayed in Figure 26(a), and fracture strength is in Figure 26(b).

It has been analyzed from the graph depicting the results of a structural simulation that fracture strength of silver microneedle is relatively low as compared to that of copper microneedle.

This is because silver has a comparatively less elastic limit and tensile strength than copper, and detailed properties are given in Table 3.

When microneedles are inserted into the skin, various forces like bending, buckling, resistive, compressive, and lateral forces have been influenced on microneedles. To predict the effect of these various forces for the projected design, the structural analysis has been executed in ANSYS. In structural analysis, the total deflection along the length of both silver and copper microneedles at the applied force of 10 N is shown in Figure 27.

In this graph, it has been observed that when force is applied a deflection starts at the length of approximately 100 μm for both solid microneedles.

In fabrication, two parameters of time and voltage have been set. By varying these two parameters, the effect on tip diameter has been analyzed and it is the same for both microneedles depending on the materials used for them. The graph is given in Figure 28.

The analysis has shown that increasing the etching time and applied voltage for both silver and copper solid microneedles will give less tip diameter or sharper tip. Also, if the applied voltage remains constant and etching time is increasing, then tip diameter decreases. The same is the case if the etching time remains constant and the applied voltage is increasing; then tip diameter also decreases. The effect on cone length of microneedle when the applied voltage remains constant and etching time increases is also shown in Figure 29.

Here, in this graph, the microneedle cone length effect has been measured by fixing the applied voltage and increasing the etching time. The cone length of the microneedle will be a maximum of 500 μm by bar comparison method.

After studying the literature review in detail, the comparison between the methods and techniques used by other researchers and the method and materials used in this research paper are given in Table 4.

Thus, from this comparison table, it has been found that silver and copper materials are more appropriate to use than other metals, silicon, and polymers. As they have been used in many medical treatments and even in medicines for many years, silver and copper nanoparticles are considered one of the most dynamic and fascinating nanomaterials among several metallic nanoparticles involved in biomedical applications. They are not only biocompatible but also bioinert. They are used as antibiotic agents in different biomedical applications.

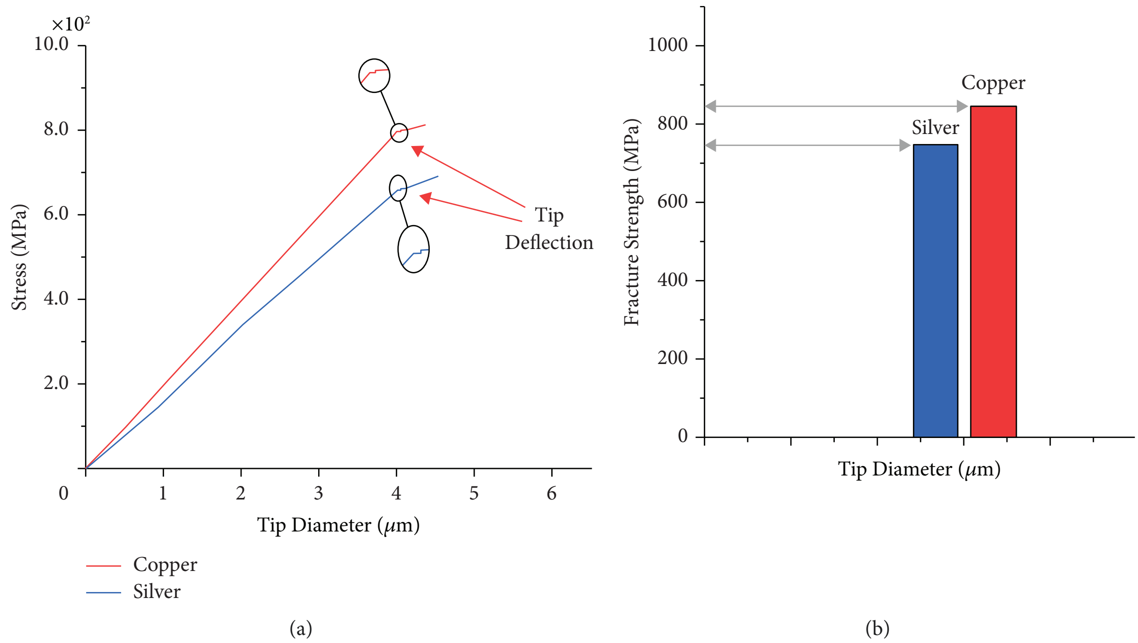

FIGURE 26: Graphical analysis of simulation results of deflection for both silver and copper microneedles. (a) Tip deflection comparison when stress is applied on both microneedles. (b) Fracture strength comparison based on the observed results of deflection.

TABLE 3: Comparison between properties of silver and copper.

Element	Silver	Copper
Ultimate tensile strength	110 MPa	210 MPa
Young's modulus of elasticity	83 GPa	120 GPa
Elastic limit	300 MPa	330 MPa
Endurance limit	40 MPa	70 MPa
Hardness	250 MPa	400 MPa

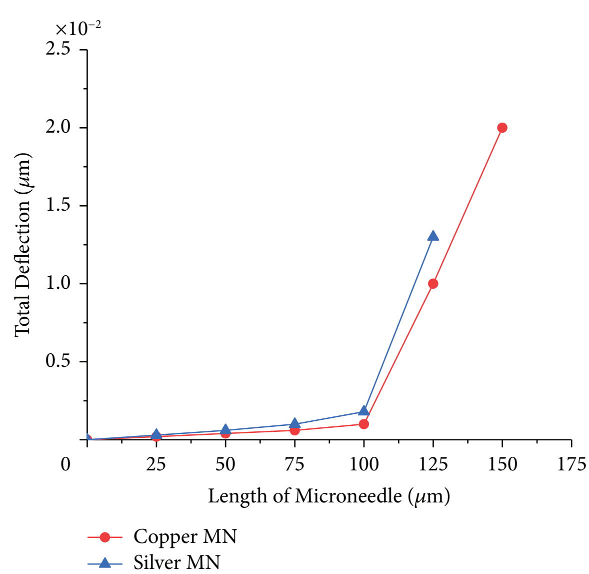

FIGURE 27: Structural analysis of total deflection along the length of silver and copper microneedles.

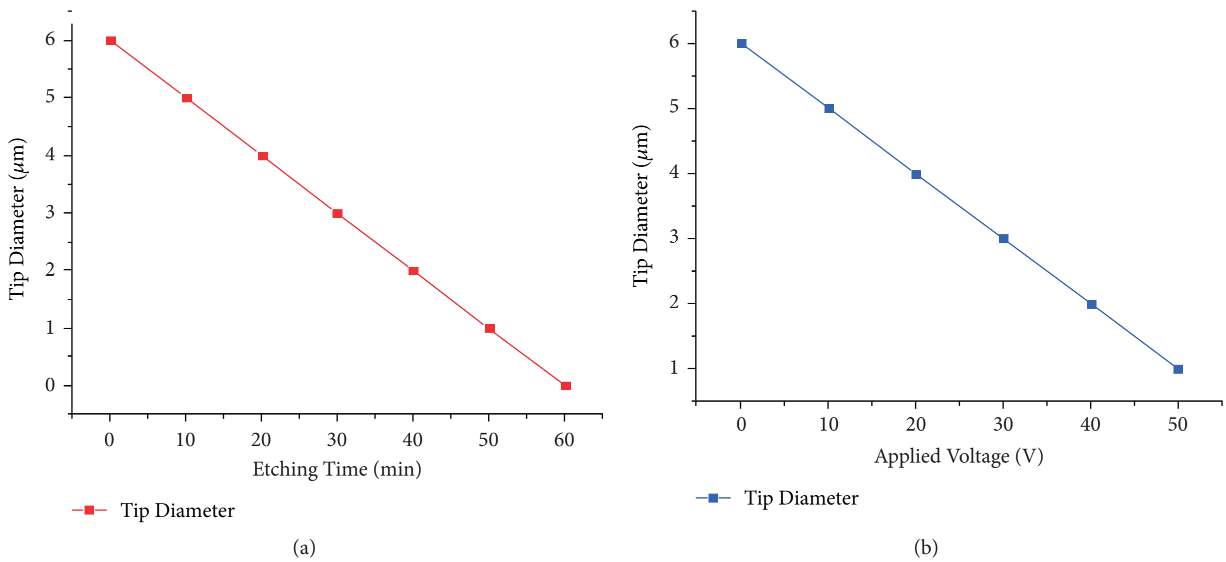

FIGURE 28: The graphs of (a) tip diameter versus etching time and (b) tip diameter versus applied voltage.

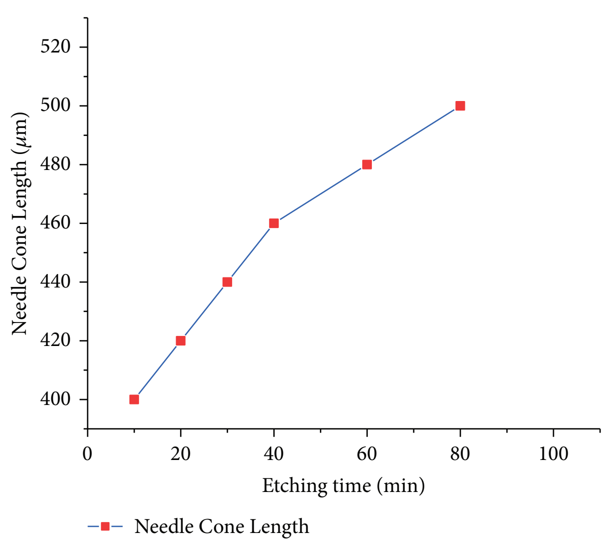

FIGURE 29: The graph of etching time versus cone length.

TABLE 4: Comparison between materials and techniques used in other works and our work.

Materials	Fabrication techniques	Advantages	Disadvantages	References
Silicon	The deep reactive ion etching process	Excellent biocompatibility and, specifically, mechanical properties are superior to polymers and metals. Also, they have nonductile nature. This technique gives much better resolution and higher aspect ratios.	Silicon microneedles are brittle and might break in insertion into the skin. This technique gives slow etch rates, low choosiness, and channel effects caused by imitated ions	[77, 78]
Stainless steel	Wet-etching photolithography	Stainless steel is characteristically more disinfected and lasts long. Wet-etching photolithography has almost no harm due to its virtuously chemical nature and is highly selective.	Stainless steel has low heat conductivity and can burn skin when heated up. Wet-etching photolithography has temperature sensitivity, poor element control, and high chemical clearance costs.	[79–82]

Table 4: Continued.

Materials	Fabrication techniques	Advantages	Disadvantages	References
Polymers	Micromolding technique	Polymers are biocompatible, biodegradable, and water-soluble. Micromolding technique is highly used for microsized objects.	The strength to size ratio of polymer is fewer as compared to metals. Cannot be machined easily and restricted speed is required for machining it. Micromolding technique is of high cost.	[83, 84]
Titanium	Surface micromachining technique or multilayer technique	Titanium is comparatively more durable and biocompatible as compared to silicon. This surface micromachining technique is more robust and reliable.	Titanium is of higher cost than other metals used and is not suitable for mass production. This technique is also of high cost.	[85–87]
Nickel	Electroless plating	Nickel is a corrosion-free and hygienic material and easily recyclable. This technique gives even coating gif nickel and smooth surface microneedles.	Some allergic reaction occurs using nickel material. High-cost technique and suitable only when the coating is involved.	[88, 89]
Silver and copper	Electrochemical etching (the electrochemical etching technique is a low-cost, clean-room-free technique and highly suitable for mass production, and no costly molding or photoresist mask is needed; it is an easily and safely used technique)	Silver is powerful, highly biocompatible, and natural antibiotic material. Silver nanoparticles are highly used in medicines for different treatments. It has ductile nature. Copper material is a biocompatible metal and endogenously exists in the human body. Copper nanoparticles have been used extensively in many medical treatments.	Silver and copper are not toxic materials so they have only minimal risk of infections and can be safely used.	Current study

Also, electrochemical etching is a low-cost technique that helps in high productivity or mass production.

8. Conclusion

To fabricate microneedles, there is a need to choose the most appropriate materials for microneedle manufacture depending on the following conditions:

(i) Manufacturing should be gentle without damaging penetrating and uneven molecules; drug release must be precise or immediate.

(ii) Mechanical strength must be sufficient for skin penetration.

Not only materials but also the appropriate technique is needed for the fabrication of solid microneedles. Many different techniques as given in Table 1 have been used. But as they are costly, and it is not economically appropriate to use them for mass production. In this research paper, numerical analysis and structural simulation have also been performed to demonstrate the deflection of the microneedles' tips and the effect of input parameters such as time and voltage on tip diameter and cone length. An economical technique for the fabrication of solid microneedle has been presented. It only costs a little as compared to other techniques for fabrication. It is easily affordable by many pharmaceutical companies. By using this technique microneedles fabrication can be increased to double at a low cost. Also, underdeveloped countries can afford this technique easily and bring microneedles technology to them as well. Not only economical techniques but also novel materials have also been chosen for the fabrication of microneedles. Silver and copper have not been used until now as a material for the fabrication of microneedle. However, they have been used for the fabrication of nanoparticles because both silver and copper are bioactive materials and have continuously been used as antibacterial coatings in many drugs or implants. This research work aims to introduce an economical and novel method for the fabrication of solid microneedles.

Data Availability

All the data and steps are given in the manuscript, and more details can be provided on demand.

Conflicts of Interest

The authors declare that there are no conflicts of interest.

References

[1] S. Indermun, R. Luttge, Y. E. Choonara et al., "Current advances in the fabrication of microneedles for transdermal delivery," *Journal of Controlled Release: Official Journal of the Controlled Release Society*, vol. 185, pp. 130–138, 2014.

[2] H. L. Quinn, M. C. Kearney, A. J. Courtenay, M. T. C. McCrudden, and R. F. Donnelly, "The role of microneedles for drug and vaccine delivery," *Expert Opinion on Drug Delivery*, vol. 11, no. 11, pp. 1769–1780, 2014.

[3] N. S. Rejinold, J.-H. Shin, H. Y. Seok, and Y. C. Kim, "Biomedical applications of microneedles in therapeutics: recent advancements and implications in drug delivery," *Expert Opinion on Drug Delivery*, vol. 13, no. 1, pp. 109–131, 2016.
[4] B. I. Kevin, "Transdermal delivery of drugs with microneedles: strategies and outcomes," *Journal of Drug Delivery Science and Technology*, vol. 29, pp. 16–23, 2015.
[5] L. R. Pires, K. Vinayakumar, M. Turos, V. Miguel, and J. Gaspar, "A perspective on microneedle-based drug delivery and diagnostics in paediatrics," *Journal of Personalized Medicine*, vol. 9, no. 4, p. 49, 2019.
[6] D. M. K. Van, R. Luttge, P. J. Vos, J. Bouwstra, G. Kersten, and I. Ploemen, "Microneedle-based drug and vaccine delivery via nanoporous microneedle arrays," *Drug Delivery and Translational Research*, vol. 5, no. 4, pp. 397–406, 2015.
[7] K. Ita, "Transdermal delivery of drugs with microneedles—potential and challenges," *Pharmaceutics*, vol. 7, no. 3, pp. 90–105, 2015.
[8] P. Bollella, S. Sharma, E. G. C. Anthony, F. Tasca, and R. Antiochia, "Minimally invasive glucose monitoring using a highly porous gold microneedles-based biosensor: characterization and application in artificial interstitial fluid," *Catalysts*, vol. 9, no. 7, 580 pages, 2019.
[9] M. Wang, L. Hu, and X. Chenjie, "Recent advances in the design of polymeric microneedles for transdermal drug delivery and biosensing," *Lab on a Chip*, vol. 17, no. 8, pp. 1373–1387, 2017.
[10] T. K. Kiang, S. A. Ranamukhaarachchi, and M. H. Ensom, "Revolutionizing therapeutic drug monitoring with the use of interstitial fluid and microneedles technology," *Pharmaceutics*, vol. 9, no. 4, p. 43, 2017.
[11] Ö. Erdem, I. Eş, G. A. Akceoglu, Y. Saylan, and F. Inci, "Recent advances in microneedle-based sensors for sampling, diagnosis and monitoring of chronic diseases," *Biosensors*, vol. 11, no. 9, p. 296, 2021.
[12] W. Li, Z. Liu, F. Fontana et al., "Tailoring porous silicon for biomedical applications: from drug delivery to cancer immunotherapy," *Advanced Materials*, vol. 30, no. 24, Article ID 1703740, 2018.
[13] L. Chang, Q. Yang, Q. Niu et al., "High-performance ionic polymer–metal composite actuators fabricated with microneedle roughening," *Smart Materials and Structures*, vol. 28, no. 1, Article ID 015007, 2018.
[14] B. L. Gray and D. Chung, "Wearable microfluidic and electronic frameworks for biomedical applications," in *ECS Meeting Abstracts*IOP Publishing, Philadelphia, PA, USA, 2018.
[15] T. Abraham, M. Mao, and C. Tan, "Engineering approaches of smart, bio-inspired vesicles for biomedical applications," *Physical Biology*, vol. 15, no. 6, Article ID 061001, 2018.
[16] E. Larraneta, R. E. Lutton, A. D. Woolfson, and R. F. Donnelly, "Microneedle arrays as transdermal and intradermal drug delivery systems: materials science, manufacture and commercial development," *Materials Science and Engineering: R: Reports*, vol. 104, pp. 1–32, 2016.
[17] Y. Kanda, H. Takehara, and T. Ichiki, "Mechanical strength evaluation of crystalline poly (L-lactic acid) fabricated by replica micromolding for bioabsorbable microneedle devices," *Japanese Journal of Applied Physics*, vol. 58, 2019.
[18] S. R. Chinnadayyala and S. Cho, "Porous platinum black-coated minimally invasive microneedles for non-enzymatic continuous glucose monitoring in interstitial fluid," *Nanomaterials*, vol. 11, no. 1, p. 37, 2021.
[19] A. Gaikwad and S. Desai, "Understanding material deformation in nanoimprint of gold using molecular dynamics simulations," *American Journal of Engineering and Applied Sciences*, vol. 11, no. 2, pp. 837–844, 2018.
[20] K. J. Nair, *Micro-injection Moulded Microneedles for Drug Delivery*, University of Bradford, Bradford, England, 2016.
[21] Y. K. Demir, Z. Akan, and O. Kerimoglu, "Characterization of polymeric microneedle arrays for transdermal drug delivery," *PLoS One*, vol. 8, no. 10, Article ID e77289, 2013.
[22] C. Jeggy, *Micro-injection Moulding: From Process to Modelling*, Presses univ. de Louvain, Louvain-la-Neuve, Belgium, 2004.
[23] T. Esho, S. Desai, and M. Craps, "Direct writing of enriched single walled carbon nanotubes towards thin film transistors (TFTs)," in *Proceedings of the IIE Annual Conference. Proceedings*, p. 1, Institute of Industrial and Systems Engineers (IISE), Nashville, Tennessee, March 2011.
[24] A. Ismail, M. H. El-Newehy, M. E. El-Naggar, A. Meera Moydeen, and A. Menazea, "Enhancement the electrical conductivity of the synthesized polyvinylidene fluoride/polyvinyl chloride composite doped with palladium nanoparticles via laser ablation," *Journal of Materials Research and Technology*, vol. 9, no. 5, pp. 11178–11188, 2020.
[25] K. T. Tran and T. D. Nguyen, "Lithography-based methods to manufacture biomaterials at small scales," *Journal of Science: Advanced Materials and Devices*, vol. 2, no. 1, pp. 1–14, 2017.
[26] E. D. Alvarado, M. G. P. Juárez, C. P. Pérez, E. Pérez, and J. A. G. Calderón, "Improvement in the dispersion of TiO2 particles inside Chitosan-Methyl cellulose films by the use of silane coupling agent," *Journal of the Mexican Chemical Society*, vol. 63, no. 2, pp. 154–168, 2019.
[27] P. Dardano, A. Caliò, V. Di Palma, M. F. Bevilacqua, A. Di Matteo, and L. De Stefano, "A photolithographic approach to polymeric microneedles array fabrication," *Materials*, vol. 8, no. 12, pp. 8661–8673, 2015.
[28] L. E. González García, M. N. MacGregor, R. M. Visalakshan et al., "Self-sterilizing antibacterial silver-loaded microneedles," *Chemical Communications*, vol. 55, no. 2, pp. 171–174, 2019.
[29] H. Chang, M. Zheng, S. W. T. Chew, and C. J. A. M. T. Xu, "Advances in the formulations of microneedles for manifold biomedical applications," *Advanced Materials Technologies*, vol. 5, no. 4, Article ID 1900552, 2020.
[30] T. Liu, G. Luo, and M. J. A. T. Xing, "Biomedical applications of polymeric microneedles for transdermal therapeutic delivery and diagnosis: current status and future perspectives," *Advanced Therapeutics*, vol. 3, no. 9, Article ID 1900140, 2020.
[31] K. Moussi, A. Bukhamsin, T. Hidalgo, and J. J. A. E. M. Kosel, "Biocompatible 3D printed microneedles for transdermal, intradermal, and percutaneous applications," *Advanced Engineering Materials*, vol. 22, no. 2, Article ID 1901358, 2020.
[32] K. Lee, M. J. Goudie, P. Tebon et al., *Advanced Drug Delivery Reviews*, pp. 41–59, 2020.
[33] G. Bonfante, H. Lee, L. Bao et al., "Comparison of polymers to enhance mechanical properties of microneedles for biomedical applications," *Micro and Nano Systems Letters*, vol. 8, no. 1, 13 pages, 2020.
[34] J. Chi, X. Zhang, C. Chen, C. Shao, Y. Zhao, and Y. J. B. m. Wang, "Antibacterial and angiogenic chitosan microneedle array patch for promoting wound healing," *Bioactive Materials*, vol. 5, no. 2, pp. 253–259, 2020.
[35] B. Cai, Y. Gong, Z. Wang, L. Wang, and W. J. T. Chen, "Microneedle arrays integrated with living organisms for

smart biomedical applications," *Theranostics*, vol. 11, no. 20, pp. 10012–10029, 2021.
[36] S. Dugam, R. Tade, R. Dhole, and S. J. F. J. o. P. S. Nangare, "Emerging era of microneedle array for pharmaceutical and biomedical applications: recent advances and toxicological perspectives," *Future Journal of Pharmaceutical Sciences*, vol. 7, no. 1, pp. 19–26, 2021.
[37] K. J. Krieger, N. Bertollo, M. Dangol, J. T. Sheridan, M. M. Lowery, and E. D. O'Cearbhaill, "Simple and customizable method for fabrication of high-aspect ratio microneedle molds using low-cost 3D printing," *Microsystems & nanoengineering*, vol. 5, no. 1, pp. 42–14, 2019.
[38] B. Altubaishe, J. Clarke, C. McWilliams, and S. Desai, "Comparative analysis of risk management strategies for additive manufacturing supply chains," *American Journal of Applied Sciences*, vol. 16, no. 8, pp. 273–282, 2019.
[39] F. K. Aldawood, S. X. Chang, and S. Desai, "Design and manufacture of a high precision personalized electron bolus device for radiation therapy," *Medical Devices & Sensors*, vol. 3, no. 6, Article ID e10077, 2020.
[40] R. M. Taylor, P. R. Miller, P. Ebrahimi, R. Polsky, and J. T. J. L. a. Baca, "Minimally-invasive, microneedle-array extraction of interstitial fluid for comprehensive biomedical applications: transcriptomics, proteomics, metabolomics, exosome research, and biomarker identification," *Laboratory Animals*, vol. 52, no. 5, pp. 526–530, 2018.
[41] P. Shende, M. J. B. P. Salunke, and E. Express, "Transepidermal microneedles for co-administration of folic acid with methotrexate in the treatment of rheumatoid arthritis," *Biomedical Physics & Engineering Express*, vol. 5, no. 2, Article ID 025023, 2019.
[42] A. Ravindran, P. Chandran, and S. S. Khan, "Biofunctionalized silver nanoparticles: advances and prospects," *Colloids and Surfaces B: Biointerfaces*, vol. 105, pp. 342–352, 2013.
[43] A. Desireddy, B. E. Conn, J. Guo et al., "Ultrastable silver nanoparticles," *Nature*, vol. 501, no. 7467, pp. 399–402, 2013.
[44] E. I. Alarcon, M. Griffith, and K. I. Udekwu, "Silver nanoparticle applications," *Springer International Publishing*, vol. 10, pp. 978–973, 2015.
[45] S. Prabhu and E. K. Poulose, "Silver nanoparticles: mechanism of antimicrobial action, synthesis, medical applications, and toxicity effects," *International Nano Letters*, vol. 2, no. 1, pp. 32–10, 2012.
[46] S. Marin, G. Vlasceanu, R. Tiplea et al., "Applications and toxicity of silver nanoparticles: a recent review," *Current Topics in Medicinal Chemistry*, vol. 15, no. 16, pp. 1596–1604, 2015.
[47] R. Singh, U. U. Shedbalkar, S. A. Wadhwani, and B. A. Chopade, "Bacteriagenic silver nanoparticles: synthesis, mechanism, and applications," *Applied Microbiology and Biotechnology*, vol. 99, no. 11, pp. 4579–4593, 2015.
[48] A. C. Burduşel, O. Gherasim, A. M. Grumezescu, L. Mogoantă, A. Ficai, and E. Andronescu, "Biomedical applications of silver nanoparticles: an up-to-date overview," *Nanomaterials*, vol. 8, no. 9, p. 681, 2018.
[49] G. Franci, A. Falanga, S. Galdiero et al., "Silver nanoparticles as potential antibacterial agents," *Molecules*, vol. 20, no. 5, pp. 8856–8874, 2015.
[50] S. Tang and J. Zheng, "Antibacterial activity of silver nanoparticles: structural effects," *Advanced healthcare materials*, vol. 7, no. 13, Article ID 1701503, 2018.
[51] I. X. Yin, J. Zhang, I. S. Zhao, M. L. Mei, Q. Li, and C. H. Chu, "The antibacterial mechanism of silver nanoparticles and its application in dentistry," *International Journal of Nanomedicine*, vol. 15, pp. 2555–2562, 2020.
[52] J. Ramyadevi, K. Jeyasubramanian, A. Marikani, G. Rajakumar, and A. A. Rahuman, "Synthesis and antimicrobial activity of copper nanoparticles," *Materials Letters*, vol. 71, pp. 114–116, 2012.
[53] G. Shobha, V. Moses, and S. Ananda, "Biological synthesis of copper nanoparticles and its impact," *Int. j. pharm. sci. Invent*, vol. 3, no. 8, pp. 6–28, 2014.
[54] L. A. Velosa-Moncada, L. A. Aguilera-Cortés, M. A. González-Palacios, J.-P. Raskin, and A. L. Herrera-May, "Design of a novel MEMS microgripper with rotatory electrostatic comb-drive actuators for biomedical applications," *Sensors*, vol. 18, no. 5, p. 1664, 2018.
[55] D. Denoyer, S. Masaldan, S. La Fontaine, and M. A. Cater, "Targeting copper in cancer therapy:'Copper that Cancer," *Metallomics*, vol. 7, no. 11, pp. 1459–1476, 2015.
[56] D. Churilov, V. Churilova, I. Stepanova et al., "Size-dependent biological effects of copper nanopowders on mustard seedlings," in *Proceedings of the IOP Conference Series: Earth and Environmental Science*, vol. 392, October 2019, Article ID 012008.
[57] S. Tayyaba, M. W. Ashraf, Z. Ahmad, N. Wang, M. J. Afzal, and N. Afzulpurkar, "Fabrication and analysis of polydimethylsiloxane (PDMS) microchannels for biomedical application," *Processes*, vol. 9, no. 1, p. 57, 2020.
[58] N. Tariq, M. W. Ashraf, and S. Tayyaba, "A review on solid microneedles for biomedical applications," *Journal of Pharmaceutical Innovation*, pp. 1–20, 2021.
[59] M. W. Ashraf, S. Tayyaba, N. Afzulpurkar et al., "Optimization of fabrication process for MEMS based microneedles using ICP etching technology," in *Advanced Materials Research*Trans Tech Publ, Stafa-Zurich, Switzerland, 2012.
[60] S. Tayyaba, M. W. Ashraf, and N. Afzulpurkar, "Design and simulation of double lumen polymeric microneedles for blood transport," in *Proceedings of the 2010 International Conference on Mechanical and Electrical Technology*, pp. 615–618, IEEE, Wuhan, China, July 2010.
[61] N. Tariq, M. W. Ashraf, and S. Tayyaba, "Simulation, analysis and characterization of solid microneedles for biomedical applications," *Journal of Intelligent and Fuzzy Systems*, pp. 1–11, 2022.
[62] S. Tayyaba, M. W. Ashraf, M. I. Tariq et al., "Skin insertion analysis of microneedle using ANSYS and fuzzy logic," *Journal of Intelligent and Fuzzy Systems*, vol. 38, no. 5, pp. 5885–5895, 2020.
[63] M. Y. Abdollahzadeh Jamalabadi, M. Daqiqshirazi, H. Nasiri, M. R. Safaei, and T. K. Nguyen, "Modeling and analysis of biomagnetic blood Carreau fluid flow through a stenosis artery with magnetic heat transfer: a transient study," *PLoS One*, vol. 13, no. 2, Article ID e0192138, 2018.
[64] M. Y. Abdollahzadeh Jamalabadi, M. Ghasemi, R. Alamian, S. Wongwises, M. Afrand, and M. S. Shadloo, "Modeling of subcooled flow boiling with nanoparticles under the influence of a magnetic field," *Symmetry*, vol. 11, no. 10, 1275 pages, 2019.
[65] H. Nasiri, M. Y. Abdollahzadeh Jamalabadi, R. Sadeghi, M. R. Safaei, T. K. Nguyen, and M. Safdari Shadloo, "A smoothed particle hydrodynamics approach for numerical simulation of nano-fluid flows," *Journal of Thermal Analysis and Calorimetry*, vol. 135, no. 3, pp. 1733–1741, 2019.
[66] A. Haghighi, M. S. Shadloo, A. Maleki, and M. Y. Abdollahzadeh Jamalabadi, "Using committee neural network for prediction of pressure drop in two-phase

microchannels," *Applied Sciences*, vol. 10, no. 15, 5384 pages, 2020.
[67] Y.-h. Zhang, S. A. Campbell, and S. Karthikeyan, "Finite element analysis of hollow out-of-plane HfO2 microneedles for transdermal drug delivery applications," *Biomedical Microdevices*, vol. 20, no. 1, pp. 19–27, 2018.
[68] M. W. Ashraf, S. Tayyaba, N. Afzulpurkar, and A. Nisar, "Fabrication and analysis of tapered tip silicon microneedles for mems based drug delivery system," *Sensors and Transducers Journal*, vol. 122, no. 11, pp. 158–172, 2010.
[69] H.-C. Kuo, Y. Lin, Y.-K. Shen, and S.-C. Kang, "Invasive PLA microneedle fabrication applied to drug delivery system," in *Proceedings of the 2011 Second International Conference on Mechanic Automation and Control Engineering*, pp. 7437–7440, IEEE, Inner Mongolia, China, July 2011.
[70] L. Zhang, J. Liu, J. Lai, and Z. Xiong, "Performance analysis of adaptive neuro fuzzy inference system control for MEMS navigation system," *Mathematical Problems in Engineering*, vol. 2014, Article ID 961067, 7 pages, 2014.
[71] Y. Chu and J. Fei, "Adaptive global sliding mode control for MEMS gyroscope using RBF neural network," *Mathematical Problems in Engineering*, vol. 2015, Article ID 403180, 9 pages, 2015.
[72] X. Ji, "Research on signal processing of MEMS gyro array," *Mathematical Problems in Engineering*, vol. 2015, Article ID 120954, 6 pages, 2015.
[73] W. Zhao, X. Sun, Y. Rong et al., "Optimization on the precision of the MEMS-redundant IMU based on adhesive joint assembly," *Mathematical Problems in Engineering*, vol. 2020, Article ID 8855141, 2020.
[74] L. Wang, B. Song, X. Han, and Y. Hao, "Attitude determination method by fusing single antenna GPS and low cost MEMS sensors using intelligent Kalman filter algorithm," *Mathematical Problems in Engineering*, vol. 2017, Article ID 4517673, 14 pages, 2017.
[75] S. Bououden, M. Chadli, and H. R. Karimi, "Fuzzy sliding mode controller design using Takagi-Sugeno modelled nonlinear systems," *Mathematical Problems in Engineering*, vol. 2013, Article ID 734094, 2013.
[76] Y. Wang, Y. Chen, and J. Lai, "Fuzzy prediction for traffic flow based on delta test," *Mathematical Problems in Engineering*, vol. 201613 pages, Article ID 5128528, 2016.
[77] S. Henry, D. V. McAllister, M. G. Allen, and M. R. Prausnitz, "Microfabricated microneedles: a novel approach to transdermal drug delivery," *Journal of Pharmaceutical Sciences*, vol. 87, no. 8, pp. 922–925, 1998.
[78] J.-H. Park, M. G. Allen, and M. R. Prausnitz, "Biodegradable polymer microneedles: fabrication, mechanics and transdermal drug delivery," *Journal of Controlled Release*, vol. 104, no. 1, pp. 51–66, 2005.
[79] H. S. Gill and M. R. Prausnitz, "Coated microneedles for transdermal delivery," *Journal of Controlled Release: Official Journal of the Controlled Release Society*, vol. 117, no. 2, pp. 227–237, 2007.
[80] M. Rajabi, N. Roxhed, R. Z. Shafagh et al., "Flexible and stretchable microneedle patches with integrated rigid stainless steel microneedles for transdermal biointerfacing," *PLoS One*, vol. 11, no. 12, Article ID e0166330, 2016.
[81] S. M. Mugo and W. Lu, "Modified stainless steel microneedle electrode for polyphenolics detection," *Analytical and Bioanalytical Chemistry*, vol. 412, no. 26, pp. 7063–7072, 2020.
[82] M.-C. Kim, J. W. Lee, H.-J. Choi et al., "Microneedle patch delivery to the skin of virus-like particles containing heterologous M2e extracellular domains of influenza virus induces broad heterosubtypic cross-protection," *Journal of Controlled Release*, vol. 210, pp. 208–216, 2015.
[83] O. Olatunji, C. C. Igwe, A. S. Ahmed, D. O. A. Alhassan, G. O. Asieba, and B. D. Diganta, "Microneedles from fish scale biopolymer," *Journal of Applied Polymer Science*, vol. 131, no. 12, 2014.
[84] S. Yang, Y. Feng, L. Zhang, N. Chen, W. Yuan, and T. Jin, "A scalable fabrication process of polymer microneedles," *International Journal of Nanomedicine*, vol. 7, p. 1415, 2012.
[85] A. Doraiswamy, C. Jin, R. Narayan et al., "Two photon induced polymerization of organic–inorganic hybrid biomaterials for microstructured medical devices," *Acta Biomaterialia*, vol. 2, no. 3, pp. 267–275, 2006.
[86] E. R. Parker, M. P. Rao, K. L. Turner, C. D. Meinhart, and N. C. MacDonald, "Bulk micromachined titanium microneedles," *Journal of microelectromechanical systems*, vol. 16, no. 2, pp. 289–295, 2007.
[87] S. A. Skoog, P. R. Miller, R. D. Boehm, A. V. Sumant, R. Polsky, and R. J. Narayan, "Nitrogen-incorporated ultrananocrystalline diamond microneedle arrays for electrochemical biosensing," *Diamond and Related Materials*, vol. 54, pp. 39–46, 2015.
[88] P. G. Jung, T. W. Lee, D. J. Oh et al., "Nickel microneedles fabricated by sequential copper and nickel electroless plating and copper chemical wet etching," *Sensors and Materials*, vol. 20, no. 1, pp. 45–53, 2008.
[89] C. Y. Jin, M. H. Han, S. S. Lee, and Y. H. Choi, "Mass producible and biocompatible microneedle patch and functional verification of its usefulness for transdermal drug delivery," *Biomedical Microdevices*, vol. 11, no. 6, pp. 1195–1203, 2009.

Hindawi
Mathematical Problems in Engineering
Volume 2022, Article ID 9712199, 12 pages
https://doi.org/10.1155/2022/9712199

Research Article

An Efficient Analytical Approach for the Periodicity of Nano/ Microelectromechanical Systems' Oscillators

Naveed Anjum,[1] **Jamshaid Ul Rahman**,[2] **Ji-Huan He**,[3,4,5] **Md. Nur Alam**,[6] **and Muhammad Suleman**[7]

[1]*Department of Mathematics, Government College University, Faisalabad 38000, Pakistan*
[2]*Abdus Salam School of Mathematical Sciences, GC University, Lahore 54600, Pakistan*
[3]*National Engineering Laboratory for Modern Silk, College of Textile and Engineering, Soochow University, Suzhou 215003, China*
[4]*School of Science, Xi'an University of Architecture and Technology, Xi'an 710055, China*
[5]*School of Mathematics and Information Science, Henan Polytechnic University, Jiaozuo 454003, China*
[6]*Department of Mathematics, Pabna University of Science and Technology, Pabna 6600, Bangladesh*
[7]*Department of Mathematics, Comsat University, Islamabad 45550, Pakistan*

Correspondence should be addressed to Md. Nur Alam; nuralam.pstu23@gmail.com

Received 1 January 2022; Accepted 21 March 2022; Published 22 April 2022

Academic Editor: Francisco Lopez-Huerta

Periodic behavior analysis of nano/microelectromechanical systems (N/MEMS) is an essential field owing to their many promising applications in microinstruments. The interesting and unique properties of these systems, particularly, small size, batch fabrication, low power consumption, and high reliability, have fascinated researchers and industries to implement these structures for the production of different microdevices. The dynamic oscillatory behavior of N/MEMS is very intricate due to the various types of nonlinearities present in these structures. The foremost objective of this study is to explore the periodicity of oscillatory problems from N/MEMS. The variational iteration method (VIM), which has been considered as an effective approach for nonlinear oscillators, is coupled with the Laplace transform to obtain the approximate analytic solution of these nonlinear vibratory systems with fewer computations. This coupling of VIM and Laplace transform not only helps in the identification of the Lagrange multiplier without getting into the details of the cryptic theory of variations, but also finds the frequency-amplitude relationship and the analytic approximate solution of N/MEMS. A generalized vibratory equation for N/MEMS is followed by three examples as special cases of this generalized equation are given to elucidate the effectivity of the coupling. The solution obtained from the Laplace-based VIM not only exhibits good agreement with observations numerically but also higher accuracy yields when compared to other established techniques in the open literature.

1. Introduction

A few decades have passed since the revelation and advancement of nano/microelectromechanical systems (N/MEMS). This innovation now has touched a level of maturity that, nowadays, several N/MEMS devices are being utilized in our daily life, ranging from pressure sensors and accelerometers in cars, radiofrequency switches, micromirrors in electronics devices such as Plasma TVs, microphones in the telecommunication industry, and inertia sensors in video games [1–6]. Conversely, with this developing demand on the N/MEMS innovation come incredible challenges. Dynamic analysis is one of them and has experienced rapid development [7]. The oscillators from N/MEMS have rich dynamics, and there are many phenomena involved in the dynamic analysis of a N/MEMS such as pull-in instability, phase diagram, and hysteresis. However, the focus of this manuscript is on the periodic solution property of N/MEMS. The exact solutions of N/MEMS, which are hard to find, play a vital role in examining the properties and behavior of these systems. Thus, researchers are interested in finding at least analytic solutions because they have more detail which helps with better insight into these systems.

In the past decades, several techniques have been proposed to get the approximate analytic solution of N/MEMS problems such as the homotopy perturbation method (HPM), higher-order HPM [8], Taylor series [9], energy balance technique [10], spreading residual harmonic balance method [11], higher-order Hamiltonian method [12], Adomian decomposition method (ADM) [13], Li-He modified HPM [14], modified ADM [15], variational approach [16], Galerkin decomposition method [17], and so on. It is also noted that, besides these methods, there are various analytical techniques for getting the approximate solution to the nonlinear equations, for example, the He-Laplace method [18], global residual harmonic balance method [19], integral transform-based methods [20–22], max-min approach [23], frequency-amplitude formulation method [24], Hamiltonian approach [25], and others [26–29]. Moreover, there have been several review articles that have appeared on the analytical methods for oscillatory problems during the past decade [30–32].

The variational iteration method (VIM) [33] is one of the most powerful techniques among the aforementioned methods, capable to solve linear and nonlinear, ordinary and partial differential equations [34–41] analytically and leading to truthful results. It was first proposed in 1998 [33] and has been extensively discussed, including its extensions and modifications [22, 41]. The main theme of the method involves the construction of a suitable iterative formula with a Lagrange multiplier that is optimally determined with the help of the variational theory. As there is no need to linearize or treat the nonlinear terms, therefore, authors [22] recently recommend that Laplace transform a simpler method to evaluate the multiplier, rendering the approach available to researchers facing different nonlinear problems. Additionally, it is noticed that nonlinear oscillators benefit greatly from this modification.

In this study, we construct a generalized nonlinear vibrational problem for N/MEMS, which under various conditions, reduces to different physical systems such as electrostatic force-based N/MEMS, the dynamic behavior of the microbeams induced by van der Waals attractions, the periodicity of the multiwalled carbon nanotubes under the effect of an electric field, etc. A Laplace-based VIM (LVIM) is employed to obtain a general solution of these microsystems and hence to obtain the deflection (y) and the oscillator's frequency (Ω) for different scenarios as the particular cases of the generalized problem. We match the findings of LVIM to those yielded numerically using the fourth-order Runge–Kutta method (RK4) and other established methods to endorse its usefulness for N/MEMS.

2. Formalism

Nonlinear oscillators often hold the following equation as follows:

$$\ddot{y}(t) + f(y) = 0, \tag{1}$$

$$\begin{aligned} y(0) &= B, \\ \dot{y}(0) &= 0. \end{aligned} \tag{2}$$

Equation (1) can be written as follows:

$$\ddot{y} + \Omega^2 y + g(y) = 0, \tag{3}$$

where $g(y) = f(y) - \Omega^2 y$.

Recently, authors [22] proposed a simple way of identifying the Lagrange multiplier for the equation (1) which is based on the Laplace transform. Let us revisit the general methodology.

Initially, the correction functional for equation (3) is established as follows:

$$y_{k+1}(t) = y_k(t) + \int_0^t \lambda(t-\psi)\left[\ddot{y}_k(\psi) + \Omega^2 y_k(\psi) + \tilde{g}_k(\psi)\right]\mathrm{d}\psi, \quad k = 0, 1, 2, \ldots\ldots, \tag{4}$$

where λ is the multiplier, y_k depicts the kth solution, and $\tilde{g}_k$ is a restricted variation i.e., $\delta\tilde{g}_k = 0$. The integration in equation (4) is ultimately a convolution; therefore, we can employ the Laplace transform easily. Utilizing the properties of the Laplace transform, and then through restricted variation, the Lagrange multiplier is identified as follows:

$$\lambda(t) = -\frac{1}{\Omega}\sin \Omega t. \tag{5}$$

Finally, the correction functional will get the following form:

$$L\left[y_{k+1}(t)\right] = L\left[y_k(t)\right] - \frac{1}{\Omega}L[\sin \Omega t]L\left[\ddot{y}_k(t) + \Omega^2 y_k(t) + \tilde{g}_k(y)\right]. \tag{6}$$

A detail derivation about the aforementioned method of solution can be seen in Ref. [21].

3. Applications

This section is devoted to a general vibratory system for N/MEMS to explain the theory described in formalism, followed by three well-known N/MEMS as the special cases of this general problem.

Consider the motion of microstructures represented with a nonlinear ordinary differential equation characterized by the general form of a group of oscillators from N/MEMS [10–12, 14, 39, 42–44] used in nanoscience and nanotechnology.

$$\begin{aligned} &\left(\alpha_0 + \alpha_1 y + \alpha_2 y^2 + \alpha_3 y^3 + \alpha_4 y^4\right)\ddot{y} + \alpha_5 + \alpha_6 y \\ &\quad + \alpha_7 y^2 + \alpha_8 y^3 + \alpha_9 y^4 + \alpha_{10} y^5 + \alpha_{11} y^6 + \alpha_{12} y^7 = 0, \end{aligned} \tag{7}$$

where $\alpha_0, \alpha_1, \ldots, \alpha_{12}$ are constants found in result of transforming a multivariable differential equation to an ordinary differential equation using Galerkin approach. Dividing equation (7) by α_0 yields

$$\left(1+d_1y+d_2y^2+d_3y^3+d_4y^4\right)\ddot{y}+d_5+d_6y + d_7y^2+d_8y^3+d_9y^4+d_{10}y^5+d_{11}y^6+d_{12}y^7=0, \tag{8}$$

where $d_j=\alpha_j/\alpha_0$ for $j=1,2,\cdots,12$. Let us rewrite equation (8) as follows:

$$\ddot{y}+\Omega^2y+g(y)=0, \tag{9}$$

where

$$g(y)=\left(d_1y+d_2y^2+d_3y^3+d_4y^4\right)\ddot{y}+d_5+\left(d_6-\Omega^2\right)y + d_7y^2+d_8y^3+d_9y^4+d_{10}y^5+d_{11}y^6+d_{12}y^7. \tag{10}$$

The iterative formula, equation (6), can be expressed as follows:

$$L\left[y_{k+1}(t)\right]=L\left[y_k\right]-\frac{1}{\Omega}L[\sin\Omega t]L\begin{bmatrix}\left(1+d_1y_k+d_2y_k^2+d_3y_k^3+d_4y_k^4\right)\ddot{y}+d_5+d_6y_k\\ +d_7y_k^2+d_8y_k^3+d_9y_k^4+d_{10}y_k^5+d_{11}y_k^6+d_{12}y_k^7\end{bmatrix}. \tag{11}$$

Assuming the initial solution

$$y_0(t)=B\cos\Omega t. \tag{12}$$

After simple calculations, we have

$$L\left[y_1(t)\right]=L[B\cos\Omega t]-\frac{1}{\Omega}L[\sin\Omega t]L\begin{bmatrix}\Gamma_0+\Gamma_1\cos\Omega t+\Gamma_2\cos 2\,\Omega t+\Gamma_3\cos 3\,\Omega t+\\ \Gamma_4\cos 4\,\Omega t+\Gamma_5\cos 5\,\Omega t+\Gamma_6\cos 6\,\Omega t+\Gamma_7\cos 7\,\Omega t\end{bmatrix}. \tag{13}$$

The following relation helps in solving the above-mentioned equation:

$$L^{-1}\left(L[\sin\Omega t]L[\cos\kappa\Omega t]\right)=\begin{cases}\dfrac{1}{2}t\sin\Omega t, & \kappa=1\\[2ex] \dfrac{\cos\Omega t-\cos\kappa\Omega t}{\Omega\left(\kappa^2-1\right)}, & \kappa\neq 1\end{cases},$$

$$\begin{aligned}y_1&=B\cos\Omega t+\frac{\Gamma_0}{\Omega^2}(\cos\Omega t-1)-\frac{\Gamma_1}{2\Omega}t\sin\Omega t-\frac{\Gamma_2}{3\Omega^2}(\cos\Omega t-\cos 2\,\Omega t)\\ &-\frac{\Gamma_3}{8\Omega^2}(\cos\Omega t-\cos 3\,\Omega t)-\frac{\Gamma_4}{15\Omega^2}(\cos\Omega t-\cos 4\,\Omega t)-\frac{\Gamma_5}{24\Omega^2}(\cos\Omega t-\cos 5\,\Omega t)\\ &-\frac{\Gamma_6}{35\Omega^2}(\cos\Omega t-\cos 6\,\Omega t)-\frac{\Gamma_7}{48\Omega^2}(\cos\Omega t-\cos 7\,\Omega t),\end{aligned} \tag{14}$$

where the expression of coefficients $\Gamma_0,\Gamma_1,\ldots,\Gamma_7$ can be depicted as follows:

$$\begin{aligned}
\Gamma_0 &= -B\Omega^2\left(\frac{d_1B}{2}+\frac{3d_3B^3}{8}\right)+d_5+\frac{d_7B^2}{2}+\frac{3d_9B^4}{8}+\frac{5d_{11}B^6}{16},\\
\Gamma_1 &= -B\Omega^2\left(1+\frac{3d_2B^2}{4}+\frac{5d_4B^4}{8}\right)+Bd_6+\frac{3d_8B^3}{4}+\frac{5d_{10}B^5}{8}+\frac{35d_{12}B^7}{64},\\
\Gamma_2 &= -B\Omega^2\left(\frac{d_1B}{2}+\frac{d_3B^3}{2}\right)+\frac{d_7B^2}{2}+\frac{d_9B^4}{2}+\frac{15d_{11}B^6}{32},\\
\Gamma_3 &= -B\Omega^2\left(\frac{d_2B^2}{4}+\frac{5d_4B^4}{16}\right)+\frac{d_8B^3}{4}+\frac{5d_{10}B^5}{16}+\frac{21d_{12}B^7}{64},\\
\Gamma_4 &= -B\Omega^2\left(\frac{d_3B^3}{8}\right)+\frac{d_9B^4}{8}+\frac{3d_{11}B^6}{16},\\
\Gamma_5 &= -B\Omega^2\left(\frac{d_4B^4}{16}\right)+\frac{d_{10}B^5}{16}+\frac{7d_{12}B^7}{64},\\
\Gamma_6 &= \frac{d_{11}B^6}{32},\\
\Gamma_7 &= \frac{d_{12}B^7}{64}.
\end{aligned} \tag{15}$$

To ensure the periodicity requires that the coefficient of $t \sin \omega t$ equal to zero, thus

$$\frac{\Gamma_1}{2\Omega}=0, \tag{16}$$

or

$$-B\Omega^2\left(1+\frac{3d_2B^2}{4}+\frac{5d_4B^4}{8}\right)+Bd_6+\frac{3d_8B^3}{4}+\frac{5d_{10}B^5}{8}+\frac{35d_{12}B^7}{64}=0, \tag{17}$$

yields

$$\Omega=\sqrt{\frac{64d_6+48d_8B^2+40d_{10}B^4+35d_{12}B^6}{64+48d_2B^2+40d_4B^4}}, \tag{18}$$

and thus the first-order approximation for the analytic solution of the equation (7) is as follows:

$$\begin{aligned}
y_{VIM} &= a_0+(a_1+B)\cos\Omega t+a_2\cos 2\,\Omega t+a_3\cos 3\,\Omega t\\
&\quad +a_4\cos 4\,\Omega t+a_5\cos 5\,\Omega t+a_6\cos 6\,\Omega t+a_7\cos 7\,\Omega t,
\end{aligned} \tag{19}$$

where

$$\begin{aligned}
a_0 &= -\frac{\Gamma_0}{\Omega^2},\\
a_1 &= \frac{1}{\Omega^2}\left(\Gamma_0-\frac{\Gamma_2}{3}-\frac{\Gamma_3}{8}-\frac{\Gamma_4}{15}-\frac{\Gamma_5}{24}-\frac{\Gamma_6}{35}-\frac{\Gamma_7}{48}\right),\\
a_2 &= \frac{\Gamma_2}{3\Omega^2},\\
a_3 &= \frac{\Gamma_3}{8\Omega^2},\\
a_4 &= \frac{\Gamma_4}{15\Omega^2},\\
a_5 &= \frac{\Gamma_5}{24\Omega^2},\\
a_6 &= \frac{\Gamma_6}{35\Omega^2},\\
a_7 &= \frac{\Gamma_7}{48\Omega^2}.
\end{aligned} \tag{20}$$

We shall now examine the several physically relevant N/MEMS cases considering various sets of parameter values in equation (7).

3.1. CASE I: Motion of Electrically Excited Microbeam. Consider the motion of an electrically actuated model of a microbeam [10, 12].

$$\left(b_0 + b_1 y^2 + b_2 y^4\right)\ddot{y} + b_3 y + b_4 y^3 + b_5 y^5 + b_6 y^7 = 0, \quad (21)$$

where the expression of coefficients $b_0, b_1, \ldots, b_7$ are as follows:

$$\begin{aligned} b_0 &= \int_0^1 \xi^2 d\eta, \\ b_1 &= -2\int_0^1 \xi^4 d\eta, \\ b_2 &= \int_0^1 \xi^6 d\eta, \\ b_3 &= \int_0^1 \left(\xi\xi'''' - N\xi\xi'' - V^2\xi^2\right) d\eta, \\ b_4 &= \int_0^1 \left(-2\xi^3\xi'''' + 2N\xi^3\xi'' - \beta\xi\xi'' \int_0^1 \xi'^2 d\eta\right) d\eta, \\ b_5 &= \int_0^1 \left(\xi^5\xi'''' - N\xi^5\xi'' + 2\beta\xi^3\xi'' \int_0^1 \xi'^2 d\eta\right) d\eta, \\ b_6 &= -\int_0^1 \left(\beta\xi^5\xi'' \int_0^1 \xi'^2 d\eta\right) d\eta, \end{aligned} \quad (22)$$

where $\xi(\eta) = 16\eta^2(1-\eta)^2$ is the trail function. Equation (21) may be achieved from the generalized equation (7) by choosing the parameters $\alpha_1 = \alpha_3 = \alpha_5 = \alpha_7 = \alpha_9 = \alpha_{11} = 0$, $\alpha_0 = b_0$, $\alpha_2 = b_1$, $\alpha_4 = b_2, \alpha_6 = b_3$, $c_8 = b_4$, $c_{10} = b_5$ and $c_{12} = b_6$.

Let us rewrite equation (21) as

$$\left(1 + m_1 y^2 + m_2 y^4\right)\ddot{y} + m_3 y + m_4 y^3 + m_5 y^5 + m_6 y^7 = 0, \quad (23)$$

where the coefficients $m_j = b_j/b_0\,(j = 1, 2, \ldots, 6)$. The frequency-amplitude relationship can be attained using equation (18) by substituting aforementioned parameters as follows:

$$\Omega_{VIM} = \sqrt{\frac{64m_3 + 48m_4B^2 + 40m_5B^4 + 35m_6B^6}{64 + 48m_1B^2 + 40m_2B^4}}, \quad (24)$$

which differs from the frequency calculated by the energy balance method (EBM) [10], which is as follows:

$$\Omega_{EBM} = \sqrt{\frac{4b_3 + 3b_4B^2 + 7b_5B^4/3 + 15b_6B^6/8}{4b_0 + 2b_1B^2 + b_2B^4}}. \quad (25)$$

The approximate solution of equation (21) by using equation (19) is as follows:

$$\begin{aligned} y_{VIM} &= \left[B - \left(\Lambda_1 + \Lambda_2 + \Lambda_3\right)\right]\cos \Omega t + \Lambda_1 \cos 3\,\Omega t \\ &\quad + \Lambda_2 \cos 5\,\Omega t + \Lambda_3 \cos 7\,\Omega t, \end{aligned} \quad (26)$$

where

$$\begin{aligned} \Lambda_1 &= \frac{1}{8\Omega^2}\left[-A\Omega^2\left(\frac{m_1B^2}{4} + \frac{5m_2B^4}{16}\right) + \frac{m_4B^3}{4} + \frac{5m_5B^5}{16} + \frac{21m_6B^7}{64}\right], \\ \Lambda_2 &= \frac{1}{24\Omega^2}\left[-A\Omega^2\left(\frac{m_2B^4}{16}\right) + \frac{m_5B^5}{16} + \frac{7m_6B^7}{64}\right], \\ \Lambda_3 &= \frac{1}{48\Omega^2}\left[\frac{m_6B^7}{64}\right]. \end{aligned} \quad (27)$$

And, the approximate analytic result by the EBM is

$$y_{EBM} = B\cos\left(\sqrt{\frac{4b_3 + 3b_4B^2 + 7b_5B^4/3 + 15b_6B^6/8}{4b_0 + 2b_1B^2 + b_2B^4}}\,t\right). \quad (28)$$

We depict the deflection of microbeam y obtained from LVIM (solid red lines) (equation (26)) with time t for four sets of parameter values (B, N, V, β) in the left side column of Figure 1 with the same yield by EBM (solid black lines) (equation (28)) and also obtained numerically by utilizing RK4 (solid blue line). This evaluation validates that the findings from the LVIM and those attained by RK4 match remarkably well.

We also graph errors in the deflection of microbeams with respect to their values evaluated using RK4. Red circles and black stars with dashed lines represent the errors of the LVIM $(y_{RK4} - y_{LVIM})$ and EBM $(y_{RK4} - y_{EBM})$, respectively, map errors against time for the similar values of parameters in the right side column of Figure 1. All panels in the right side column confirm that the accuracy of the solution obtained by LVIM is much improved in comparison to the solution obtained by means of EBM because the margin of error is less in the case of LVIM. Moreover, it is notable that the error in EBM is increasing with an increase in amplitude, but the error in LVIM is insignificant.

The effectiveness of the LVIM for the nonlinear analytic frequency and the approximate solution can be seen in Figure 2 which represents the influence of different

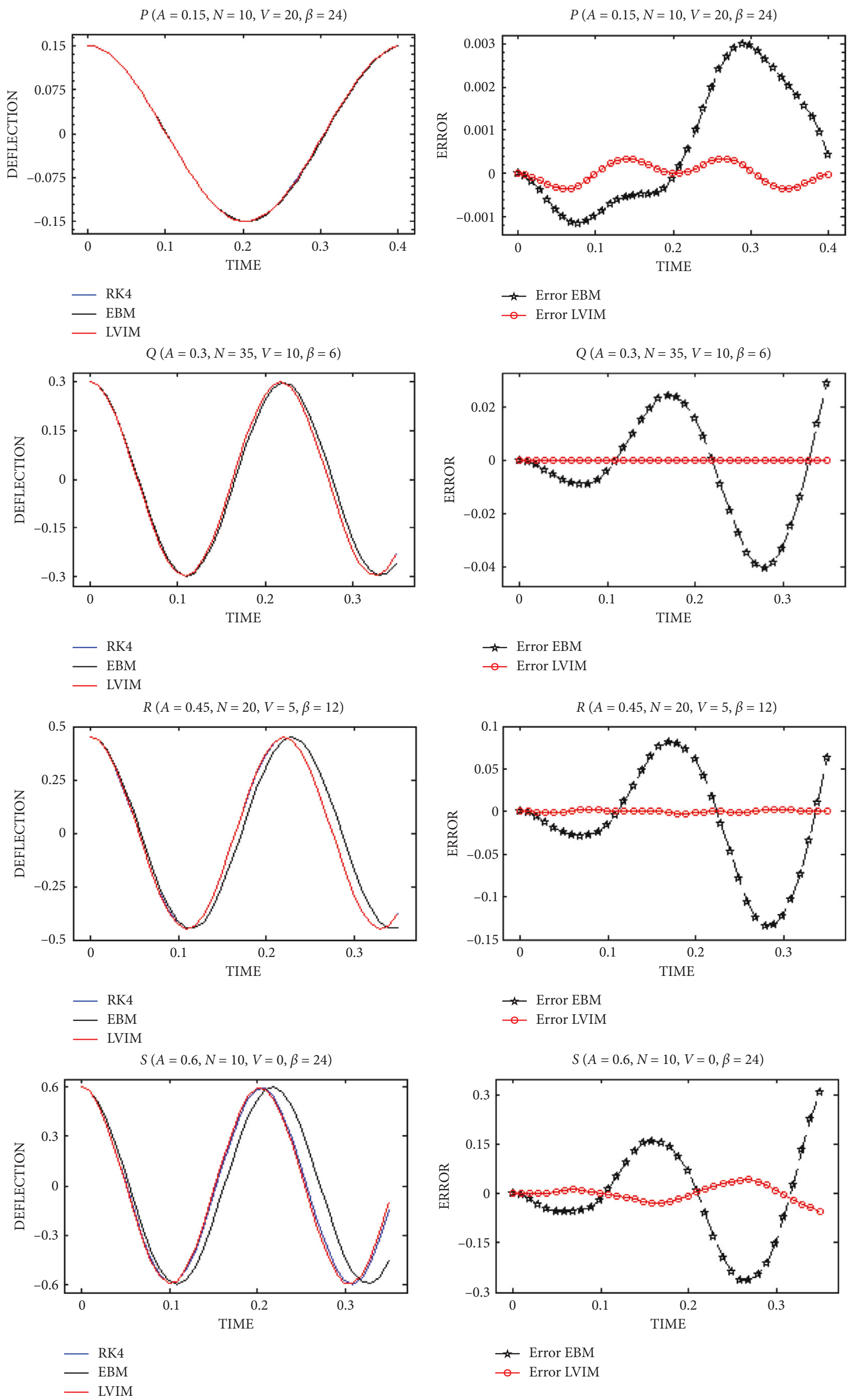

Figure 1: Comparison of results obtained by LVIM and EBM with RK4 findings for electrically excited microbeam.

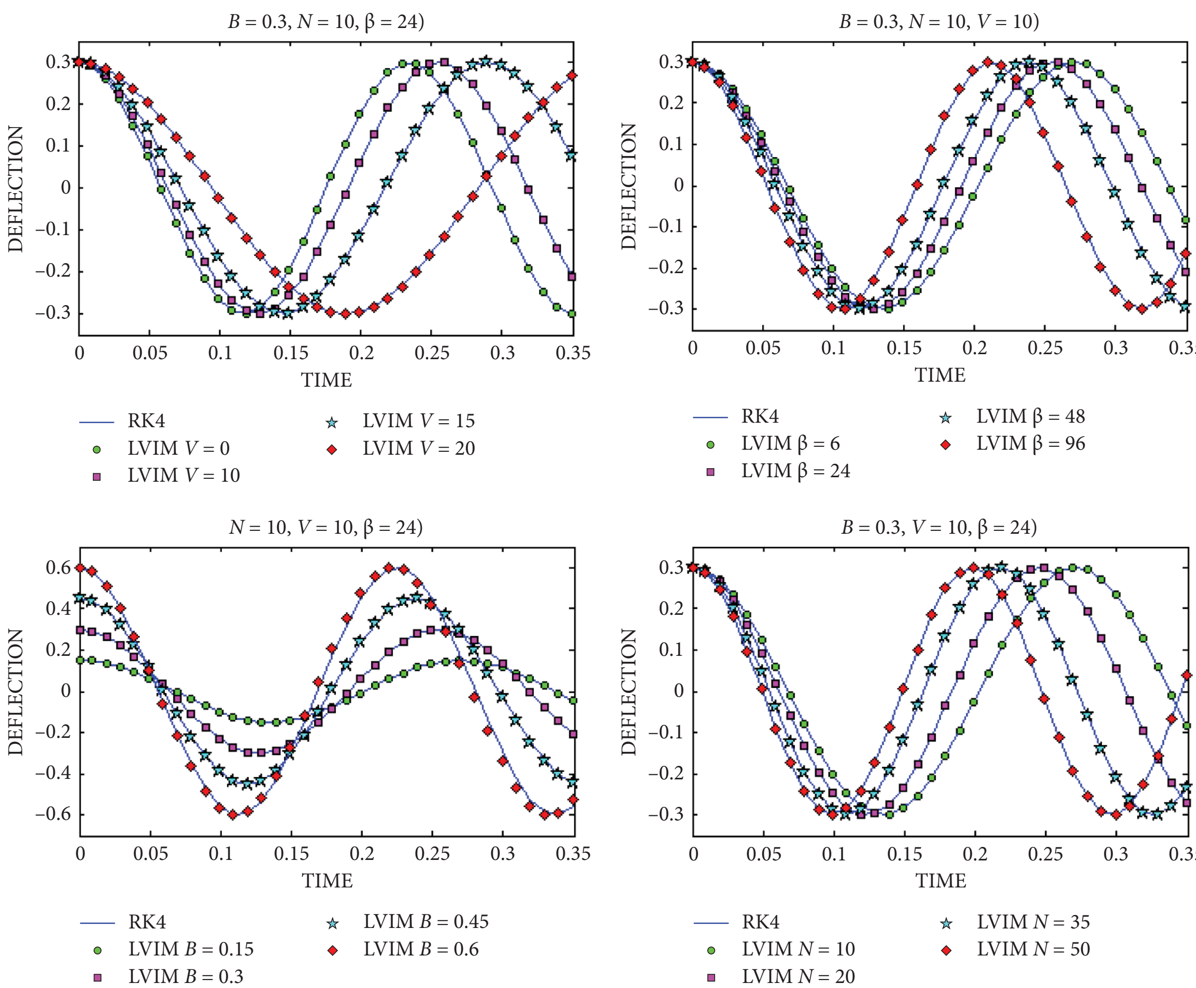

FIGURE 2: Influence of the parameters on the deflection of electrically excited microbeam.

parameters on the deflection of microbeams. To this end, one of the mentioned parameters is supposed to change while the three other ones remain constant. The graphs in this figure demonstrate the accuracy of the solution obtained in equation (26) because the observations attained by the LVIM are in good agreement with those achieved numerically using RK4.

3.2. CASE II: Motion of Nanobeams Actuated by Van der Waals Attractions. Consider the motion of an N/MEMS of nanobeams induced by the Van der Waals attractions [11, 39]. Intermolecular interactions or van der Waals force have been used instead of electrostatic force in this microstructure for actuation. The mathematical model can be represented as follows:

$$\left(h_0 + h_1 y + h_2 y^2 + h_3 y^3\right)\ddot{y} + h_4 + h_5 y + h_6 y^2 + h_7 y^3 + h_8 y^4 + h_9 y^5 + h_{10} y^6 = 0, \tag{29}$$

where the coefficients $h_0, h_1, \ldots, h_{10}$ can be written as follows and a detailed derivation of equation (29) and the physical understanding of each coefficient are available in Refs. [11, 39].

$$\begin{aligned}
h_0 &= \int_0^1 \xi^2 d\eta,\\
h_1 &= -3\int_0^1 \xi^3 d\eta,\\
h_2 &= 3\int_0^1 \xi^4 d\eta,\\
h_3 &= -\int_0^1 \xi^5 d\eta,\\
h_4 &= -\lambda \int_0^1 \xi \, d\eta,\\
h_5 &= \int_0^1 (\xi\xi'''' - N\xi\xi'')d\eta,\\
h_6 &= \int_0^1 \left(-3\xi^2\xi'''' + 3N\xi^2\xi''\right)d\eta,\\
h_7 &= \int_0^1 \left(3\xi^3\xi'''' - 3N\xi^3\xi''\right)d\eta - \beta\int_0^1 \xi\xi'' d\eta \int_0^1 \xi'^2 d\eta,\\
h_8 &= \int_0^1 \left(-\xi^4\xi'''' + N\xi^4\xi''\right)d\eta + 3\beta\int_0^1 \xi^2\xi'' d\eta \int_0^1 \xi'^2 d\eta,\\
h_9 &= -3\beta\int_0^1 \xi^3\xi'' d\eta \int_0^1 \xi'^2 d\eta,\\
h_{10} &= \beta\int_0^1 \xi^4\xi'' d\eta \int_0^1 \xi'^2 d\eta,
\end{aligned} \tag{30}$$

where $\xi(\eta) = \sin \pi\eta$ is the trail function. Equation (29) is solved for different trail function by means of the spreading residue harmonic balance method (SRHBM) [11], which can be attained by putting the parameters $\alpha_0 = h_0,\ \alpha_1 = h_1,\ \alpha_2 = h_2,\ \alpha_3 = h_3,\ \alpha_4 = 0, \alpha_5 = h_4,\ \alpha_6 = h_5, \alpha_7 = h_6,\ \alpha_8 = h_7, \alpha_9 = h_8,\ \alpha_{10} = h_9,\ \alpha_{11} = h_{10}$, and $\alpha_{12} = 0$ in the general form of equation (7).

Equation (29) can rewrite in the following form:

$$\left(1 + k_1 y + k_2 y^2 + k_3 y^3\right)\ddot{y} + k_4 + k_5 y + k_6 y^2 + k_7 y^3 + k_8 y^4 + k_9 y^5 + k_{10} y^6 = 0, \tag{31}$$

where the coefficients $k_n = h_n/h_0\,(n = 1, 2, \ldots, 10)$. The nonlinear frequency of this oscillatory system using LVIM can be gained by placing the abovementioned parameters in equation (18) and can be written as follows:

$$\Omega = \sqrt{\frac{8k_5 + 6k_7B^2 + 5k_9B^4}{8 + 6k_2B^2}}, \tag{32}$$

which is similar to the frequency of order first calculated by SRHBM [11]. The approximate analytic solution of equation (29) is obtained by LVIM from equation (19) as follows:

$$y_{LVIM} = e_0 + (e_1 + B)\cos \Omega t + e_2 \cos 2\,\Omega t + e_3 \cos 3\,\Omega t + e_4 \cos 4\,\Omega t + e_5 \cos 5\,\Omega t + e_6 \cos 6\,\Omega t, \tag{33}$$

where

$$\begin{aligned} e_0 &= -\frac{\Upsilon_0}{\Omega^2},\\ e_1 &= \frac{1}{\Omega^2}\left(\Upsilon_0 - \frac{\Upsilon_2}{3} - \frac{\Upsilon_3}{8} - \frac{\Upsilon_4}{15} - \frac{\Upsilon_5}{24} - \frac{\Upsilon_6}{35}\right),\\ e_2 &= \frac{\Upsilon_2}{3\Omega^2},\\ e_3 &= \frac{\Upsilon_3}{8\Omega^2},\\ e_4 &= \frac{\Upsilon_4}{15\Omega^2},\\ e_5 &= \frac{\Upsilon_5}{24\Omega^2},\\ e_6 &= \frac{\Upsilon_6}{35\Omega^2}, \end{aligned} \tag{34}$$

where the expression of coefficients $\Upsilon_0, \Upsilon_1, \ldots, \Upsilon_2$ can be identified as follows:

$$\begin{aligned} \Upsilon_0 &= -B\Omega^2\left(\frac{k_1 B}{2} + \frac{3k_3B^3}{8}\right) + k_4 + \frac{k_6B^2}{2} + \frac{3k_8B^4}{8} + \frac{5k_{10}B^6}{16},\\ \Upsilon_1 &= -B\Omega^2\left(1 + \frac{3k_2B^2}{4}\right) + Bk_5 + \frac{3k_7B^3}{4} + \frac{5k_9B^5}{8},\\ \Upsilon_2 &= -B\Omega^2\left(\frac{k_1 B}{2} + \frac{k_3B^3}{2}\right) + \frac{k_6B^2}{2} + \frac{k_8B^4}{2} + \frac{15k_{10}B^6}{32},\\ \Upsilon_3 &= -B\Omega^2\left(\frac{k_2B^2}{4}\right) + \frac{k_7B^3}{4} + \frac{5k_9B^5}{16},\\ \Upsilon_4 &= -B\Omega^2\left(\frac{k_3B^3}{8}\right) + \frac{k_8B^4}{8} + \frac{3k_{10}B^6}{16},\\ \Upsilon_5 &= \frac{k_9B^5}{16},\\ \Upsilon_6 &= \frac{k_{10}B^6}{32}. \end{aligned} \tag{35}$$

Figure 3 represents the deflection obtained analytically from a numerical solution for the vibration of nanobeams excited by Van der Waals attraction. We have also plotted the variation of error for the above-mentioned system in the corresponding bottom panels. From the top panel of Figure 3, it is seen that the approximate results were achieved numerically using RK4 (blue line), the SRHBM [11] (black line), and those obtained by the LVIM (red line) equation (33) for two sets of parameters (B, N, β, λ), which reveals the accuracy of the findings achieved by the present application of LVIM. Errors of the SRHBM are symbolized with black stars with solid lines, while errors of LVIM are denoted with red circles against time for the same parameter values in the bottom panel confirming the supremacy of LVIM over SRHBM. Furthermore, in the top panel, a significant difference between the solutions of RK4 and SRHBM can be observed on the trough part of the wave, but the LVIM solution matches extremely well in that part. The same is observed in the error graph shown in the bottom panel. These facts authenticate the great potential of the LVIM for solving nonlinear problems over SRHBM.

Figure 4 demonstrates the effect of change in midpoint deflection of the nanobeams due to variation in parameter values of the model. The LVIM results and those attained by RK4 are almost similar which indicates that LVIM can correctly predict the oscillatory behavior of these microstructures.

3.3. CASE III: Motion of Multiwalled Carbon Nanotubes. Consider the equation of motion of multiwalled carbon nanotubes that includes both the electrostatic and Van der Waals attraction forces for actuating [42].

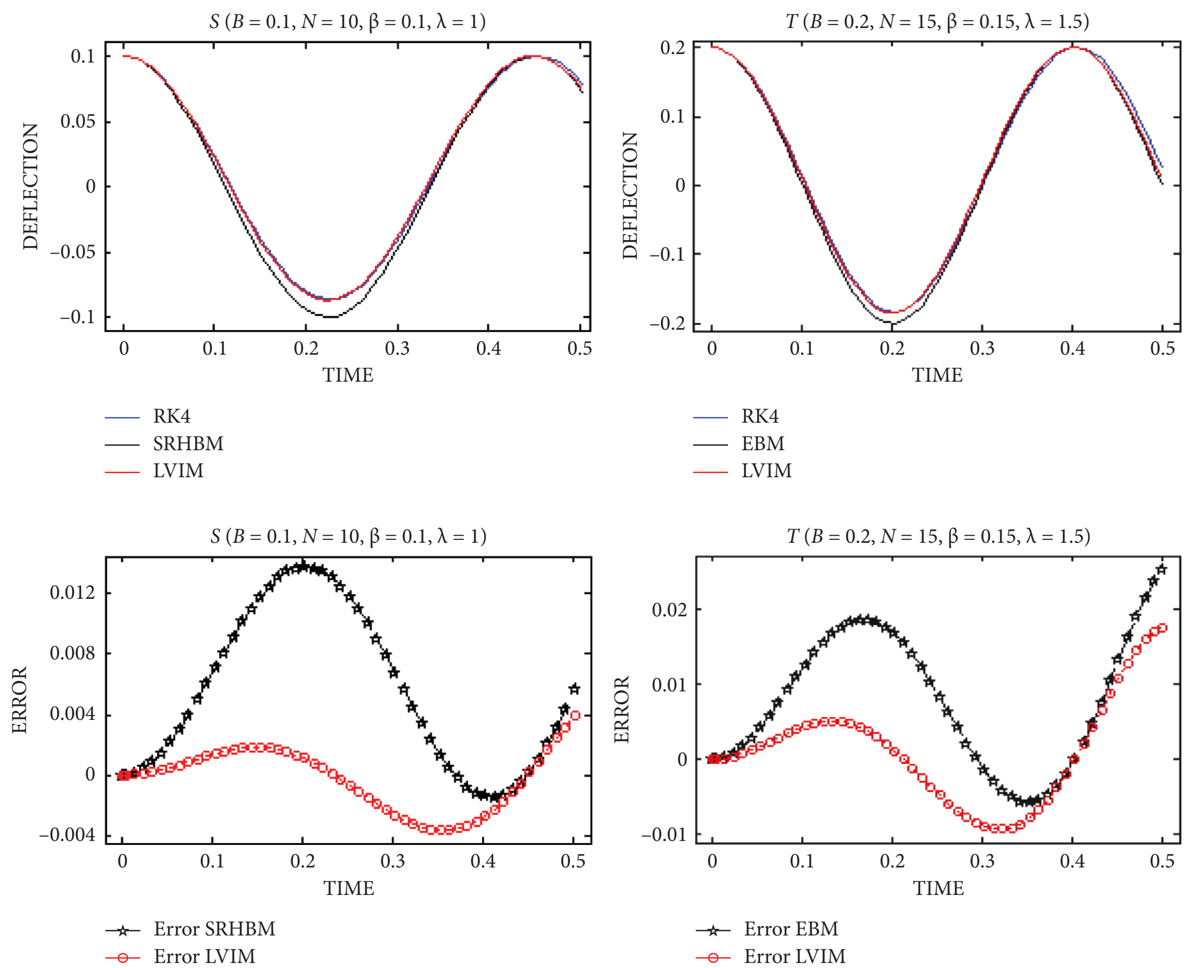

Figure 3: Comparison of results obtained by LVIM and SRHBM with RK4 findings for the nanobeams actuated by Van der Waals force.

$$\ddot{y} + \ell_0 + \ell_1 y + \ell_2 y^2 + \ell_3 y^3 + \ell_4 y^4 = 0, \quad (36)$$

where the coefficients $\ell_0, \ell_1, \ldots, \ell_4$ and detailed derivation of the model equation can be found in [42]. This vibratory model can be achieved by substituting $\alpha_1 = \alpha_2 = \alpha_3 = \alpha_4 = \alpha_{10} = \alpha_{11} = \alpha_{12} = 0$, $\alpha_0 = 1$, $\alpha_5 = \ell_0$, $\alpha_6 = \ell_1$, $\alpha_7 = \ell_2$, $\alpha_8 = \ell_3$, and $\alpha_9 = \ell_4$ in the generalized equation (7). The LVIM frequency may obtained from equation (18) as follows:

$$\Omega = \sqrt{\ell_1 + \frac{3}{4}\ell_3 B^2}. \quad (37)$$

The LVIM solution of equation (36) is as follows:

$$y_{HPLTM} = \Psi_0 + [\Psi_1 + B]\cos \Omega t + \Psi_2 \cos 2\,\Omega t + \Psi_3 \cos 3\,\Omega t + \Psi_4 \cos 4\,\Omega t, \quad (38)$$

where

$$\Psi_0 = -\frac{1}{\Omega^2}\left[\ell_0 + \frac{\ell_2 B^2}{2} + \frac{3\ell_4 B^4}{8}\right],$$
$$\Psi_1 = \frac{1}{\Omega^2}\left[\frac{\ell_2 B^2}{3} - \frac{\ell_3 B^3}{32} + \frac{\ell_4 B^4}{5}\right],$$
$$\Psi_2 = \frac{1}{3\Omega^2}\left[\frac{\ell_2 B^2}{2} + \frac{\ell_4 B^4}{2}\right],$$
$$\Psi_3 = \frac{1}{8\Omega^2}\left[\frac{\ell_3 B^3}{4}\right], \quad (39)$$

and

$$\Psi_4 = \frac{1}{15\Omega^2}\left[\frac{\ell_4 B^4}{8}\right]. \quad (40)$$

Both frequency and solution are similar to those given by [42] gained by means of the iteration perturbation method and also the same as those given by [43, 44] employing the parameter expansion method.

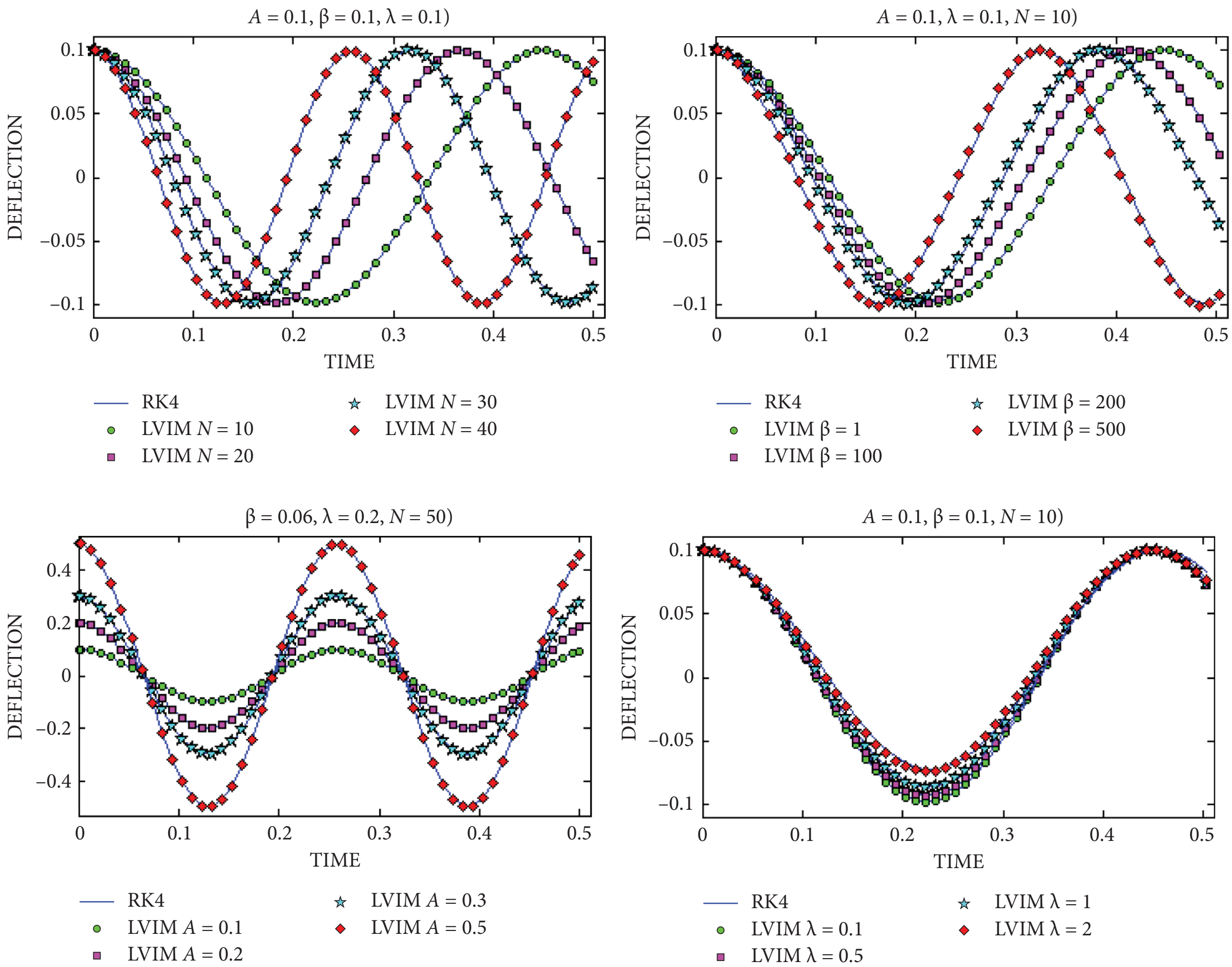

Figure 4: Influence of parameters on deflection of nanobeams actuated by Van der Waals force.

4. Conclusion

A vibratory equation for N/MEMS in its general form is reduced to ordinary differential equations with nonlinearities such as the motion of a microbeam actuated electrically, the vibration of nanobeams under the effect of Van der Waals attractions, and the motion of multiwalled carbon nanotubes. The variational iteration method (VIM) coupled with the Laplace transformation is utilized to achieve the nonlinear analytic frequency and approximate solution of the generalized model of N/MEMS and its relevant systems with great success. We considered some novel variational iteration formulas where the Lagrange multiplier is identified with the help of the Laplace transform which eliminates the elusive theory of variations. The merit of the proposed method is its simplicity (no need to do any integration) and capability to solve nonlinear models with high accuracy. Comparative results of the Laplace-based variational iteration method, energy balance process, spreading residual harmonic balance technique, and Runge–Kutta scheme were given to show the efficacy of the suggested strategy. It is concluded that the obtained results for the generalized model enable us to examine numerous nonlinear physical N/MEMS easily in a similar way.

Data Availability

No datasets were generated or analyzed during the current study.

Conflicts of Interest

The authors declare that they have no conflicts of interest.

References

[1] M. I. Younis, *MEMS Linear and Nonlinear Statics and Dynamics*, Springer, Berlin, Germany, 2011.

[2] E. Ruocco and V. Mallardo, "Buckling and vibration analysis nanoplates with imperfections," *Applied Mathematics and Computation*, vol. 357, pp. 282–296, 2019.

[3] M. Kumar, S. Yadav, and A. Kumar, "MEMS impedance flow cytometry designs for effective manipulation of micro entities in health care applications," *Biosensors and Bioelectronics*, vol. 142, 2019.

[4] J. Zhou, "Quenching for a parabolic equation with variable coefficient modeling MEMS technology," *Applied Mathematics and Computation*, vol. 314, pp. 7–11, 2017.

[5] X. Zang, Q. Zhou, J. Chang, Y. Liu, and L. Lin, "Graphene and carbon nanotube (CNT) in MEMS/NEMS applications," *Microelectronic Engineering*, vol. 132, pp. 192–206, 2015.

[6] R. Osiander, M. A. G. Darrin, and J. Champion, "MEMS and microstructures in aerospace applications," *Tribology and Lubrication Technology*, vol. 12, p. 54, 2006.

[7] J. Ul Rahman, D. Lu, M. Suleman, J. H. He, and M. Ramzan, "He–Elzaki method for spatial diffusion of biological population," *Fractals*, vol. 27, no. 5, Article ID 1950069, 2019.

[8] S. Ampun and P. Sawangtong, "The approximate analytic solution of the time-fractional Black-Scholes equation with a European option based on the Katugampola fractional derivative," *Mathematics*, vol. 9, no. 3, p. 214, 2021.

[9] M. Moghimi Zand, M. T. Ahmadian, and B. Rashidian, "Semi-analytic solutions to nonlinear vibrations of microbeams under suddenly applied voltages," *Journal of Sound and Vibration*, vol. 325, pp. 382–396, 2009.

[10] Y. Fu, J. Zhang, and L. Wan, "Application of the energy balance method to a nonlinear oscillator arising in the microelectromechanical system (MEMS)," *Current Applied Physics*, vol. 11, pp. 482–485, 2011.

[11] Y. H. Qian, J. L. Pan, and Y. Qiang, "The spreading residue harmonic balance method for studying the doubly clamped beam-type N/MEMS subjected to the van der Waals attraction," *J. Low Freq. Noise V. A.*vol. 38, no. 3–4, pp. 1261–1271, 2019.

[12] S. Sadeghzadeh and A. Kabiri, "Application of higher order Hamiltonian approach to the nonlinear vibration of micro electro mechanical systems," *Latin American Journal of Solids and Structures*, vol. 13, pp. 478–497, 2016.

[13] M. M. Khader and N. H. Sweilam, "Singularly perturbed BVP to estimation of diaphragm deflection in MEMS capacitive microphone: an application of ADM," *Applied Mathematics and Computation*, vol. 281, pp. 214–222, 2016.

[14] N. Anjum, J. H. He, Q. T. Ain, and D. Tian, "Li-He's modified homotopy perturbation method for doubly-clamped electrically actuated microbeams-based microelectromechanical system," *Facta Universitatis – Series: Mechanical Engineering*, vol. 19, 2021.

[15] R. Soroush, A. Koochi, and A. Kazemi, "Modeling the effect of van der Waals attraction on the instability of electrostatic cantilever and doubly–supported nano-beams using modified Adomian method," *International Journal of Structural Stability and Dynamics*, vol. 12, Article ID 1250036, 2013.

[16] Y. Zuo and H. Liu, "Instability of the printing jet during the three-dimensional-printing process," *Journal of Low Frequency Noise, Vibration and Active Control*, Article ID 14613484211021518, 2021.

[17] A. R. Askari and M. Tahani, "Stability analysis of electrostatically actuated nano/micro-beams under the effect of van der Waals force, a semi-analytical approach," *Communications in Nonlinear Science and Numerical Simulation*, vol. 34, pp. 130–141, 2016.

[18] M. Suleman, D. Lu, and C. Yue, "He-Laplace method for general nonlinear periodic solitary solution of vibration equations," *J Low Freq Noise V A*, vol. 38, no. 3-4, pp. 1297–1304, 2019.

[19] M. Mohammadian and M. Shariati, "Approximate analytical solutions to a conservative oscillator using global residue harmonic balance method," *Chinese Journal of Physics*, vol. 55, no. 1, pp. 47–58, 2017.

[20] N. Anjum, M. Suleman, and D. Lu, "Numerical iteration for nonlinear oscillators by Elzaki transform," *J. Low Freq. Noise V. A.*vol. 39, no. 4, pp. 879–884, 2019.

[21] K. Manimegalai, C. F. S. Zephania, and P. K. Bera, "Study of strongly nonlinear oscillators using the Aboodh transform and the homotopy perturbation method," *Eur Phys J Plus*, vol. 134, pp. 462–469, 2019.

[22] N. Anjum and J. H. He, "Laplace transform: making the variational iteration method easier," *Applied Mathematics Letters*, vol. 92, pp. 134–138, 2019.

[23] S. S. Ganji, A. Barari, and D. D. Ganji, "Approximate analysis of two-mass–spring systems and buckling of a column," *Computers & Mathematics With Applications*, vol. 61, no. 4, pp. 1088–1095, 2011.

[24] Z.-Y. Ren, "Theoretical basis of He's frequency-amplitude formulation for nonlinear oscillators," *Nonlinear Sci. Lett. A*, vol. 9, no. 1, pp. 86–90, 2017.

[25] A. Hassan, "Application of higher order Hamiltonian approach to nonlinear vibrating systems," *Journal of Theoretical and Applied Mechanics*, vol. 51, no. 2, pp. 287–296, 2013.

[26] S. Hosseinzadeh, Kh. Hosseinzadeh, M. Rahai, and D. Ganji, "Analytical solution of nonlinear differential equations two oscillators mechanism using Akbari–Ganji method," *Modern Physics Letters B*, vol. 35, no. 31, Article ID 2150462, 2021.

[27] Z. Y. Ren, "A simplified He's frequency–amplitude formulation for nonlinear oscillators," *Journal of Low Frequency Noise, Vibration and Active Control*, vol. 41, Article ID 14613484211030737, 2021.

[28] Y. Zhang, D. Tian, and J. Pang, "A fast estimation of the frequency property of the microelectromechanical system oscillator," *Journal of Low Frequency Noise, Vibration and Active Control*, vol. 41, Article ID 14613484211051837, 2021.

[29] B. M. I. Haque and M. M. A. Hossain, "An effective solution of the cube-root truly nonlinear oscillator: extended iteration procedure," *International Journal of Differential Equations*, vol. 2021, Article ID 7819209, 2021.

[30] J. H. He, N. Anjum, and P. Skrzypacz, "A variational principle for a nonlinear oscillator arising in the microelectromechanical system," *Journal of Applied and Computational Mechanics*, vol. 7, no. 1, pp. 78–83, 2021.

[31] M. Bayat, I. Pakar, and G. Domairry, "Recent developments of some asymptotic methods and their applications for nonlinear vibration equations in engineering problems: a review," *Latin American Journal of Solids and Structures*, vol. 9, no. 2, pp. 1–93, 2012.

[32] Y. Shen and Y. O. El-Dib, "A periodic solution of the fractional sine-Gordon equation arising in architectural engineering," *Journal of Low Frequency Noise, Vibration and Active Control*, vol. 40, no. 2, pp. 683–691, 2021.

[33] E. Hesameddini and H. Latifizadeh, "Reconstruction of variational iteration algorithms using the Laplace transform," *International Journal of Nonlinear Sciences and Numerical Stimulation*, vol. 10, no. 11-12, pp. 1377–1382, 2009.

[34] Z.-L. Tao, G.-H. Chen, and Y.-H. Chen, "Variational iteration method with matrix Lagrange multiplier for nonlinear oscillators," *Journal of Low Frequency Noise, Vibration and Active Control*, vol. 38, no. 3-4, pp. 984–991, 2019.

[35] D. D. Durgun and A. Konuralp, "Fractional variational iteration method for time-fractional non-linear functional partial differential equation having proportional delays," *Thermal Science*, vol. 22, pp. S33–S46, 2018.

[36] Z. M. Odibat and S. Momani, "Application of variational iteration method to nonlinear differential equations of fractional order," *International Journal of Nonlinear Sciences and Numerical Stimulation*, vol. 7, no. 1, pp. 27–34, 2006.

[37] G. C. Wu, D. Baleanu, and Z. G. Deng, "Variational iteration method as a kernel constructive technique," *Applied Mathematical Modelling*, vol. 39, no. 15, pp. 4378–4384, 2015.

[38] I. A. Yeasmin, M. S. Rahman, and M. S. Alam, "The modified Lindstedt–Poincare method for solving quadratic nonlinear

oscillators," *Journal of Low Frequency Noise, Vibration and Active Control*, vol. 40, no. 3, pp. 1351–1368, 2021.

[39] M. Mohammadiana, "Application of the variational iteration method to nonlinear vibrations of nanobeams induced by the van der Waals force under different boundary conditions," *Eur Phys J Plus*, vol. 132, pp. 169–181, 2017.

[40] J. I. Ramos, "On the variational iteration method and other iterative techniques for nonlinear differential equations, Appl. Math. Comp," vol. 199, no. 1, pp. 39–69, 2008.

[41] S. A. Khuri and A. Sayfy, "Generalizing the variational iteration method for BVPs: proper setting of the correction functional," *Applied Mathematics Letters*, vol. 68, pp. 68–75, 2017.

[42] H. M. Sedighi and F. Daneshmand, "Static and dynamic pull-in instability of multi-walled carbon nanotube probes by He's iteration perturbation method," *Journal of Mechanical Science and Technology*, vol. 28, no. 9, pp. 3459–3469, 2014.

[43] H. M. Sedighi, A. Reza, and J. Zare, "Using parameter expansion method and min-max approach for the analytical investigation of vibrating micro-beams pre-deformed by an electric field," *Advances in Structural Engineering*, vol. 16, no. 4, pp. 693–699, 2013.

[44] H. M. Sedighi and K. H. Shirazi, "Vibrations of micro-beams actuated by an electric field via Parameter Expansion Method," *Acta Astronautica*, vol. 85, pp. 19–24, 2013.